1-1-1988

A study of the microstructure of PVF2/PMMA blends by small angle neutron and x-ray scattering/

William Stewart Herman
University of Massachusetts Amherst

Recommended Citation

A STUDY OF THE MICROSTRUCTURE

OF PVF$_2$/PMMA BLENDS

BY SMALL ANGLE NEUTRON AND X-RAY SCATTERING

A Dissertation Presented

by

WILLIAM STEWART HERMAN

Submitted to the Graduate School of the
University of Massachusetts in partial fulfillment
of the requirements for the degree of

DOCTOR OF PHILOSOPHY

February 1988

Department of Polymer Science and Engineering

A STUDY OF THE MICROSTRUCTURE OF PVF_2/PMMA BLENDS

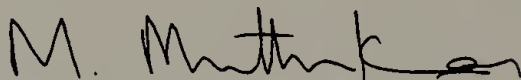BY SMALL ANGLE NEUTRON AND X-RAY SCATTERING

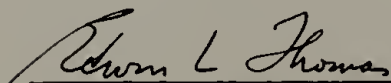A Dissertation Presented

by

WILLIAM S. HERMAN

Approved as to style and content by:

_____
Richard S. Stein, Chairperson of Committee

_____
Murugappan Muthukumar, Member

_____
Edwin L. Thomas, Member

_____
Edwin L. Thomas, Department Head
Polymer Science and Engineering

ACKNOWLEDGMENTS

Dedicated

to my Mother

ABSTRACT

A Study of the Microstructure of PVF_2/PMMA Blends
by Small Angle Neutron and X-ray Scattering

(February 1988)

William S. Herman
B.S., City College of New York
M.S., University of Massachusetts
Ph.D., University of Massachusetts

Directed by: Professor Richard S. Stein

Small angle x-ray and neutron scattering studies were performed on blends of PVF_2 with PMMA. A comparison of the scattered intensities indicates that the electron density profile is different from the neutron scattering length density profile. This system, therefore, cannot be modelled assuming only two phases.

The SANS and SAXS invariants were used to calculate transition zone thicknesses for two other models. The first model assumes a linear transition zone between the crystalline PVF_2 phase and the mixed amorphous phase. The other model consists of three phases: a crystalline PVF_2 phase, an amorphous PVF2 phase containing branched material and cilia, and a mixed amorphous phase. It has been determined that an interphase exists at the crystal-amorphous phase boundary and it is at least 25Å in thickness (interlamellar distance $\cong$ 200 Å). The interphase thickness assuming a linear transition zone is ~50Å, while for the three-phase system is about ~25Å.

The method of using two invariants to determine phase sizes and especially transition zone thicknesses is superior to measuring transition zone thicknesses from deviations from Porod's law.

TABLE OF CONTENTS

LIST OF TABLES

LIST OF FIGURES

Chapter 1

INTRODUCTION

The commercial blending of polymers is well over 30 years old. The basic motivation to study blends is to understand why polymers mix and what effect mixing has on the two polymers in the mixed state. This fundamental understanding would meet the commercial motive as well, which is to obtain the best performance such as high modulus, easier processability or better impact properties for the dominant component in the blend at the lowest possible cost. Several general reviews and references regarding the properties of polymeric alloys can be found in the literature [1-5].

Blends of two miscible polymers usually give intermediate properties between those of the components. Amorphous miscible polymers compose the bulk of the most widely used commercial blends, such as atactic polystyrene (aPS) with poly(phenylene oxide) (PPO) [6-7] or poly(vinyl chloride), PVC, with butadiene-acrylonitrile copolymers [8-9]. Crystalline, liquid crystalline and amorphous polymers as well can be mixed to form immiscible blends, which constitute essentially composite materials such as toughened epoxies.

Many polymer pairs rely on specific interactions between the chain substituents, a negative enthalpic contribution to the free energy of mixing, to be compatible. The entropic contribution is negligible, though negative, due to the polymer's long chain nature. However, at elevated temperatures, the enthalpic contribution to mixing becomes positive, causing these mixtures to phase separate [10-14]. Similar to this liquid-liquid transition, a liquid-solid transition, crystallization, can occur which also leads to segregation into two or more phases. It is also important to understand the role of processing parameters such as temperature, annealing time, orientation, etc. on the final

morphology in order to control these and therefore the blend's final properties. This thesis is concerned with the final morphology of blends in which one component crystallizes. To this end small angle scattering techniques are used to study the microstructure of an amorphous polymer which resides between the crystalline lamellae of its blend counterpart.

When one polymer crystallizes from a homogeneously mixed amorphous state the noncrystallizable component is not included in the crystal. Instead, it is rejected to form a pure phase of its own or a blend with the crystallizable polymer in regions where this remains in an amorphous state, such as between the lamellae [15-18]. A subject of considerable scientific interest for these blends is to define which are the factors that influence the rejection phenomenon and why and how much does each factor contribute. It is well established that parameters such as temperature, molecular weight, miscibility and relative glass transition temperature of the two polymers will affect the final structure of the blend. However, a quantitative understanding of the mechanisms involved is still lacking.

Flexible polymers in a quiescent state tend to crystallize from the melt forming spherulites. These macrostructures are spherical during the intermediate stages of growth and assume a polyhedral shape in the late stages of crystallization as a consequence of impingement. Spherulites are composed of crystalline lamellae extending radially from the center such that the polymer chain direction is predominantly perpendicular to the radius. When a non-crystallizable component is added, it is selectively rejected upon crystallization of the system to one of three regions: the interspherulitic region, the interfibrillar region or the interlamellar region. Low molecular weight components and other additives that are able to diffuse faster than the crystal growth front advances will segregate into the interspherulitic region [19-20]. Any polymer

2

chain of lower diffusing ability relative to crystal formation will be included inside the spherulite, either between the lamellae or between the fibrils. Fibrils, in spherulites, are composed of bundles or stacks of lamellae (since lamellae are almost always much wider than they are thick) separated by the rejected material. The interfibrillar region is intermediate in size between the other two regions. It has been found that amorphous polymers that have no specific interactions with and have roughly the same glass transition temperature, T_g, as the crystallizing component, such as atactic polystyrene (aPS)/isotactic polystyrene (iPS) blends, reside in the interfibrillar region [21-23]. Finally, amorphous polymers that have strongly favorable interactions with and a considerably higher T_g than the crystallizing polymer are contained between the crystalline lamellae [24-27]; the interlamellar region represents the smallest rejection zone of the three.

Naturally occurring spherulites were studied as early as the late 1800's in certain silicates [28]. And as early as 1929 Bernauer proposed that impurities play an important role in the formation and coarseness of spherulites [29]. In his experiments he studied the effect of adding impurities to several organic compounds inducing spherulite formation when in their pure state they did not.

Keith and Padden in 1963 developed a phenomenological theory to describe impurity rejection in crystallizing polymer systems [30]. In their approach, impurities are defined as any substance which crystallizes considerably slower than the most readily crystallizable chains, such as small molecule additives, noncrystallizable polymers or homopolymer fractions of lower stereoregularity or molecular weight (there is a lower probability of a shorter molecule having the correct conformation to add to the crystal surface). The theory attempts to predict an average size for the crystalline

3

fibrils both for homopolymers and for blends in which one component crystallizes.

The theory assumes that crystallization of a spherulite proceeds linearly with time, and that the growth front can be considered planar on a small scale. As the growth front advances, crystallizing chains are extracted out of the melt in front of the crystal, causing the relative concentration of the non-crystallizing entities to increase in that region. After crystallizing for a transitory period a steady state is reached. The concentration profile of impurity ahead of the growth front is described by:

$$C(x) = C_0 \exp(-x/\delta) + C_\infty$$

where C_0 and C_∞ represent the excess concentrations of the impurity at the growth face and its concentration at an infinite distance from the growth face, respectively. C_∞ and C_0 have no physical significance in themselves since this is a phenomenological theory. The thickness of the impurity layer is the decay constant, defined as $\delta = D/G$, where D is the diffusion constant of the impurity away from the growth front and G is the growth rate. A constant growth rate implies that the rejected polymer cannot diffuse radially faster than the crystal front advances. When steady state conditions are reached, the concentration of the impurity remains constant during the isothermal crystallization of a given system. A more complete background on this subject is given by Chalmers [31] or Delves [32] who describe a similar development referring to small molecule systems.

The exponential concentration profile of impurities at the growth front implies that the relative fraction of crystallizable material increases rapidly with distance from the crystal. Perturbations on the crystal surface profile due to fluctuations in the local growth rate will create projections into a melt richer in crystallizable material. Therefore, these projections will continue to

grow giving rise to a fibrous morphology within the spherulites. Impurities rejected during the process of fibril formation will diffuse laterally accumulating in the adjacent regions. This increase in impurity concentration inhibits any perturbation in these zones from developing into a stable fibril. The limiting distance between independently growing fluctuations is of the order of δ. Therefore, the fibrillar size in crystallizing systems containing any impurities is $\delta = D/G$ and it can be calculated if the values of D and G for the system being studied are known.

Optical microscopy studies performed by Keith and Padden [33-36] showed their theory to be qualitatively correct. They examined several polymer blends varying the molecular weight of the impurity and crystallization temperature and showed a definite trend was present relating spherulite coarseness and δ.

The Keith and Padden theory has also been used in PVF_2/PMMA [30] blends to explain the presence of the amorphous component between the lamellae. The inherently low diffusion coefficient of the PMMA [37-40] is reduced further by its favorable interactions with PVF_2 [38]; PVF_2 has a relatively fast growth rate [39-41]. Both of these factors combined lead to a small value of δ. Blends of PVF_2 with PMMA have been studied extensively by several techniques. Paul et al. [42-45] blended several oxygen containing polymers with PVF_2 to determine what polymers will have the most favorable interactions with the fluorines in PVF_2. They concluded that polymers containing carbonyl groups are highly miscible with PVF_2. Similar results were found from infrared spectroscopy of PVF_2/PMMA blends [46-47] from shifts in the carbonyl absorption peaks. This blend exhibits a cloud point at 330°C [45,48], well above the ceiling temperature for PMMA. Also, negative

interaction parameters [49] from SAXS [50] and SANS [51] in the melt state along with melting point depression data [52-53] confirm that this is one of the most miscible blends studied to date.

Early thermal and dielectric studies have shown that for low concentrations of PVF_2 (below 40 volume %) in PMMA, the blend shows little or no crystallinity by the presence of only a single T_g. Above 40 volume percent, PVF_2 will crystallize from the melt. This is evidenced by the presence of the relaxation for PVF_2 at 100°C. Two other relaxations are also observed: one at 60-80°C corresponding to the T_g of the mixed PMMA/PVF_2 phase and a relaxation at -40°C [54-59] (dynamic mechanical thermal analysis done in this work, Figure 1) which is the T_g or amorphous PVF_2. A model of phase separation in the melt followed by crystallization was proposed to explain these results. The conclusions of the scattering data and the thermal data are in opposition to each other.

Hahn, Wendorff and Yoon [60-61] have recently proposed a model to take into account both sets of results. They reject a two-phase model which was consistent with Morra's results because there is no amorphous PVF_2 phase. They also reject a transition zone between the crystalline and mixed amorphous phase because the relaxation peak for the amorphous PVF_2 did not shift or broaden. They concluded that the transition zone must be of constant density and composed of pure PVF_2. Its placement between the two phases was chosen since head-to-head, tail-to-tail and branched PVF_2 units would be rejected from the crystal to its surface forming this extra phase. This would then form a dense phase which would resist mixing with the PMMA.

The presence of a transition zone in crystalline polymers has been predicted by Flory, Yoon and Dill [62-64] using a lattice model. The problem they addressed was one of calculating the number of chain units necessary for

6

a chain leaving a crystal surrounded by other chains all parallel to each other to become random in direction. From their calculations for polyethylene a transition zone must exist which is about 10-12Å wide. This had already been shown by Vonk [65] experimentally.

This investigation examines the microstructure of PVF_2 when blended with PMMA focusing mainly on the presence and size of the transition zone between the crystalline and amorphous phase. This analysis will be performed using SAXS and SANS since the combination of the two techniques gives far more information than either one of the techniques alone. The scattered intensities are used to calculate parameters for several lamellar models.

THEORY

2.1 Three-dimensional Systems

The purpose of this chapter is to give a basic background in scattering theory for the relationships used in this thesis. The literature contains many excellent reviews on its fundamentals and applications pertaining to polymers [66-71]. The basic relationship between real space and reciprocal (Fourier) space is represented in the equation:

$$I(q) = K' \iiint \gamma(r) \exp (iq\ r)\, dr \tag{1}$$

where K' is a constant, r is the vector between two points in real space, $\gamma(r)$ is the three-dimensional correlation function averaged over all points r apart, q is the momentum transfer vector for which $|q| = 4\pi/\lambda \sin 2\theta_B/2$ and $I(q)$ is the intensity in reciprocal space at the point q from the origin. For isotropic systems integration over θ and $\emptyset$ gives:

$$I(q) = 4\pi K' \int \gamma(r)\, r^2\, \frac{\sin qr}{qr}\, dr \tag{2}$$

By Fourier inversion $\gamma(r)$ can be expressed as the transform of $I(q)$ as:

$$\gamma(r) = K \int I(q)\, q^2\, \frac{\sin qr}{qr}\, dq \tag{3}$$

The three-dimensional correlation function is defined by Debye et al. [72-73] as being zero as r goes to infinity and one when $r = 0$. The correlation function is related to the probability of a rod of length r having both ends in the

same phase either in the same particle or in two different particles, and can be calculated by:

$$\gamma(r) = \frac{<\eta(r')\,\eta(r'+r)>}{<\eta(r')\,\eta(r')>} \qquad (4)$$

where $\eta(r')$ is the difference between the scattering density at r' from the average of the system. The brackets $<\ >$ refer to the average over all r's. For light the scattering density depends on the refractive index, for x-rays η denotes the electron density, and for neutrons η is the ratio of the sum of the scattering lengths of one monomer divided by its respective volume. This is represented as:

$$\eta_{iSAXS} = \rho_i^e - \rho^e \qquad (5a)$$

$$\eta_{iSANS} = (a_i/v_i) - (a/v) \qquad (5b)$$

where ρ^e, a_i and v_i are the electron density, the sum of the neutron scattering lengths and the monomer volume of phase i and ρ^e and a/v are the average values of the electron density and the scattering density.

Often, the correlation of a particle with itself is important. A self-correlation can be described as the probability of both ends of a rod existing in the same phase, but not the same particle. The correlation function at r is given by the common volume of the two particles averaged over θ and $\emptyset$ [69]. Mathematically, the two particles are placed on two sets of coordinates a distance r apart. One set of axes is allowed to vary for all x, y and z. For instance, the correlation function for a sphere is [74]:

$$\gamma(r) = 1 - \frac{3}{4}r + \frac{1}{16}r^3 \qquad (6)$$

and for a rectangular parallelepipedon in which $r < a$, $r < b$ and $r < c$ [69] it is:

$$\gamma(r) = 1 - r\left[\frac{ab + ac + bc}{2V}\right] + r^2\left[\frac{2(a + b + c)}{3\pi V}\right] - \frac{r^3}{4\pi V} \tag{7}$$

At larger r's the limits of the integrals become difficult to handle, but simple computer programs can be used to generate these functions (Appendix A). If higher order terms are neglected in equations 6 and 7 the slope of $\gamma(r)$ at the origin is equal to a quarter of the surface to volume ratio;

$$\gamma(r) = 1 - \frac{Sr}{4V} \tag{8}$$

which is Porod's original derivation for a particle of any shape [75] in real space. So for any two-phase structure in which only density fluctuations are being considered Porod's law states that the correlation function must decrease linearly with r.

For objects that have simple shapes such as cubes, spheres or cylinders the dimensions are readily calculable from a correlation function. However, for more complex particles, the isotropic orientation of the particles in space removes details from $\gamma(r)$.

An average size or correlation length can still be calculated by:

$$l_c = 2\int_0^\infty \gamma(r)\,dr \tag{9}$$

The same information can also be obtained directly from the scattering curve avoiding the calculation of $\gamma(r)$ altogether. The Fourier transform of equation 8 at the limit of infinite q gives Porod's law [76]:

$$I(q) = \frac{2\pi \Delta \rho^2}{q^4} \left(\frac{S}{V} \right) \qquad (10)$$

for which $\Delta \rho^2$ is the square of the electron density, for x-ray scattering, between the two phases. The slope of a plot of $I(q)q^2$ vs. q^{-2} will be proportional to the surface to volume ratio. If the scattered intensities are not in absolute units, then:

$$I(q) = \frac{Q}{\pi \emptyset_1 (1-\emptyset_1) q^4} \left(\frac{S}{V} \right) \qquad . \qquad . \qquad (11)$$

where:

$$Q = \int_0^\infty I(q) \, q^2 dq \qquad (12)$$

and $\emptyset_1$ is the volume fraction of phase 1. For more random structures an average size or "reduced inhomogeneity length" [77] is given by:

$$l_c = \frac{4\emptyset_1 (1-\emptyset_1)}{(S/V)} \qquad (13)$$

This reduced inhomogeneity length can be related to the average size of each of the phases by:

$$l_1 = \frac{l_c}{(1-\emptyset_1)} \qquad \qquad 2 = \frac{l_c}{\emptyset_1} \qquad (14)$$

For a dilute system of particles, the small angle region also contains much information. Gunier's law states that for such a system the scattered intensities are given by:

$$I(q) = \exp\left(-R_g^2 q^2/3\right) \tag{15}$$

for the condition of $q\,R_g \ll 1$ where R_g is the radius of gyration of one particle. Porod's law and Gunier's law can be used to obtain a size of the structures present in a three-dimensional isotropic system.

2.2 Lamellar Systems

For lamellar morphologies in crystalline polymers the scattering contrast varies predominantly along the normal to the lamellae. On a microstructural scale this can be treated as a one-dimensional system, while on a macrostructural scale the lamellae are randomly oriented in space making the system isotropic. Therefore, lamellae can be modelled as a series of randomly oriented one-dimensional systems for which the intensity is given by:

$$i(q) = 2V\overline{\eta^2} \int \gamma(x) \cos qx \, dx \tag{16}$$

where $i(q)$ is the intensity from one stack of lamellae and $\gamma(x)$ is the one-dimensional correlation function (as opposed to the three-dimensional correlation function). Again $i(q)$ is the Fourier transform of $\gamma(x)$ so that:

$$\gamma(x) = \frac{1}{\pi V \overline{\eta^2}} \int i(q) \cos qx \, dx \tag{17}$$

The intensity, $i(q)$, is from a single stack of lamellae, but in an isotropic system this intensity is spread out on the surface of a sphere of radius q in reciprocal space. Therefore, as q increases the surface of the sphere grows with q^2 so that the measured intensity, $I(q)$, is:

$$I(q) \, \alpha \, \frac{i(q)}{4\pi q^2} \qquad (18)$$

giving:

$$\gamma(x) = \frac{K}{\eta^2} \int_0^\infty I(q)q^2 \cos qx \, dq \qquad (19)$$

The correlation function is calculated from the auto-correlation or the auto-convolution [if $\eta(x)$ is chosen to be an even function] of the electron density profile as:

$$\gamma(x) = \frac{1}{\eta^2} \int_0^\infty \eta(x') \, \eta(x + x') \, dx' \qquad (20)$$

$\eta(x)$ is usually chosen as a series of square pulses which can include a transition zone and distributions of crystalline and amorphous sizes. These are then fit to the experimental functions, but little extra information is gained. Again, the scattering curve contains far more information about the system.

A major part of this thesis is based on the analysis of the SAXS and SANS invariants. The invariant is the square of the average deviation of the electron density or neutron scattering cross-section. The invariant can be understood in two ways. First, if we define the Fourier transform of $\eta(x)$ as $A(q)$, then:

$$i(q) = A(q) A^*(q) = \int_0^\infty \gamma(x) \cos qx \, dx \qquad (21)$$

$$A(q) A^*(q) = I(q) q^2 \qquad (22)$$

Parseval's theorem states that no energy should be lost between the point that the radiation leaves the object to when it arrives at the detector. In mathematical terms, this is shown as:

$$\frac{1}{2\pi} \int_{-\infty}^{\infty} |A(q)|^2 \exp(iqx) \, dq = C \int_{-\infty}^{\infty} \eta(x') \eta(x - x') \, dx' \tag{23}$$

and when $x = 0$ then:

$$\frac{1}{2\pi} \int_{-\infty}^{\infty} |A(q)|^2 \, dq = C \int_{-\infty}^{\infty} |\eta(x')|^2 \, dx' \tag{24}$$

or:

$$\frac{1}{2\pi} \int_{-\infty}^{\infty} I(q) q^2 \, dq = C \int_{-\infty}^{\infty} |\eta(x')|^2 \, dx' \tag{25}$$

Physically, at $x = 0$, this is the point at which all objects are perfectly correlated with themselves (no negative contributions) so that equations 24 and 25 are now:

$$\langle \eta^2 \rangle = K \int_{0}^{\infty} I(q) q^2 \, dq \tag{26}$$

A comparison of several electron density profiles along with the square of the electron density deviation is shown in Figure 2. The invariant, $\langle \eta^2 \rangle$, is the average of the square deviation over one repeat period and for an ideal two-phase system:

$$\langle \eta^2 \rangle = \eta_1^2 \emptyset_1 + \eta_2^2 \emptyset_2 \tag{27}$$

or:

$$<\eta^2> = (\rho_1^e - \rho_2^e)^2 \, \emptyset_1 \emptyset_2 \tag{28}$$

If there are three phases of constant electron density, then:

$$<\eta^2> = \eta_1^2 \, \emptyset_1 + \eta_2^2 \, \emptyset_2 + \eta_3^2 \, \emptyset_3 \tag{29}$$

$$<\eta^2> = (\rho_1^e - \rho_2^e)^2 \, \emptyset_1 \emptyset_2 + (\rho_1^e - \rho_3)^2 \, \emptyset_1 \emptyset_3 + (\rho_2^e - \rho_3^e)^2 \, \emptyset_2 \emptyset_3 \tag{30}$$

If we introduce a linear transition zone between the two phases of constant composition, then:

$$<\eta^2> = (\rho_1^e - \rho_2^e)^2 \left(\emptyset_1 \emptyset_2 - \frac{ES}{6V} \right) \tag{31}$$

For a lamellar model the predominant contribution to the surface is normal to the lamellae; there are two interfaces per repeat period so that $S/2V = 1/L$ giving:

$$<\eta^2> = (\rho_1^e - \rho_2^e)^2 \left(\emptyset_1 \emptyset_2 - \frac{\emptyset_E}{6} \right) \tag{32}$$

where $\emptyset_e$ is the volume fraction of transition zone in the material. As can be seen, the introduction of any type of transition zone will decrease the invariant when the contrast between the two phases does not change.

Using conventional x-ray generators, x-rays are usually collimated with a slit instead of a pinhole as is the case in these experiments. The intensities obtained are defined as smeared intensities as opposed to desmeared intensities

for pinhole colimation. This line of intensity is perpendicular to the detector as shown in Figure 3, where the y direction is the main beam direction and q is the detector position. The scattering measured for an isotropic system corresponds to $I(\sqrt{y^2 + q^2})$ but is measured at q on the detector. Likewise, all the y values will contribute to the measured intensity at q. This line of intensity can be treated as a series of pinhole scatterers. Mathematically, this is described by:

$$\tilde{I}(q) = \int_{-\infty}^{\infty} I\left(\sqrt{q^2 + y^2}\right) w(y)\, dy \tag{33}$$

for:

$$\int w(y) = 1 \tag{34}$$

For nonisotropic scatterers this equation needs to be modified by the introduction of an angular dependence of the desmeared intensity. In this situation, the experiment should be performed on a rotating anode generator using pinhole colimation because the equations are too cumbersome.

A simplification can be made in equation 33 by allowing W(y) to be a constant. Along with this, the beam must be long enough in the y direction so that the contribution at even the widest $\sqrt{q^2 + y^2}$'s are recorded at small q's. Mathematically, the length of the beam at the detector position must be greater than $(q_{max} - S_{dd})/2$. Usually this condition is not as rigorous since scattering at large q's is negligible with respect to the scattered intensities at small q's. This is called the infinite height assumption and yields:

$$\tilde{I}(q) = \int_{-\infty}^{\infty} I\left(\sqrt{q^2 + y^2}\right) dy \tag{35}$$

As an example, Porod's law for desmeared intensities relates $I(q)$ to q^{-4}, but for smeared intensities this becomes:

$$\tilde{I}(q) = \int_{-\infty}^{\infty} \frac{K_P}{(q^2 + y^2)^2} \, dy \; = \frac{\pi K_P}{2q^3} \tag{36}$$

and the invariant can be calculated from:

$$<\eta^2> = \frac{K'}{2} \int_0^{\infty} \tilde{I}(q) \, q \, dq \tag{37}$$

The calculation of the desmeared intensities from the smeared is performed by:

$$I(q) = \frac{\partial}{\partial q} \int_0^{\infty} \tilde{I}\left(\sqrt{q^2 + a^2}\right) da \tag{38}$$

This equation can also be used to obtain a correlation function for smeared data in which the infinite height assumption applies. Equation 19 relates the desmeared intensity to the correlation function. Combining equations 19 and 38 and integrating by parts gives:

$$\gamma(x) = \frac{1}{2\pi} \iint \tilde{I}\left(\sqrt{q^2 + a^2}\right) \cos qx \, dq \, da -$$
$$\frac{1}{2\pi} \iint \tilde{I}\left(\sqrt{q^2 + a^2}\right) qx \sin qx \, dq \, da \tag{39}$$

and for $q = z\cos\theta$ and $z = z\sin\theta$:

$$\gamma(x) = \frac{1}{4} \int_0^{\infty} z \, \tilde{I}(z) \left[J_0(zx) - qx \, J_1(zx) \right] dz \tag{40}$$

17

(As much as possible it is always favorable to calculate parameters from the intensities directly from the detector.)

From equation 23 the Fourier transform of a convolution of two functions is their product in reciprocal space. Deviations from Porod's law can be accounted for by the inclusion of a transition zone between the two phases. These deviations in the scattering curve cause the intensity in the large q region to decrease proportionately to q^n where n usually varies from -5 to -6 instead of -4. Mathematically the electron density profile including a transition zone for a one-dimensional lamellar stack can be expressed as:

$$\rho^e(x) = \int_0^\infty \rho^e_{ideal}(x') \, h(x-x') \, dx' \tag{41}$$

where $\rho^e_{ideal}(x)$ represents a series of square pulses and $h(x)$ is a smoothing function dependent on the type of transition zone.

The Fourier transform of the auto-correlation of $\rho^e(x)$ is the product of the above functions in reciprocal space:

$$I(q) = I_{ideal}(q) \, H^2(q) \tag{42}$$

where $H(q)$ is the Fourier transform of $h(x)$. For ideal two-phase systems with sharp boundaries, $I_{ideal}(q)$ can be replaced by Porod's law at larger angles giving:

$$I(q) = \frac{KpH^2(q)}{q^4} \tag{43}$$

So at wide angles a simple expression can be used to describe the existance of a transition layer.

The Fourier series is a simple method of expressing any periodic function as a series of sinusoidal terms of various wavelengths. Originally developed to solve diffusion equations Fourier theory can also be applied to light waves, and their interaction with matter. Fourier transforms result from allowing the periodicity of a given function to approach infinity. A periodic function can be represented by a series of spikes in Fourier space. As the repeat period is allowed to increase, the distance between spikes in Fourier space grows closer together but the envelope of the tips of the spikes remains constant, and, in the limiting case, becomes a continuous function.

Therefore, there is no limit as to what the smoothing function can be. The two most common smoothing functions describe a linear transition zone and a sigmoidal transition zone between the two phases. A linear transition zone of thickness E can be represented by:

$$h(x) = 1/E \quad \text{from} \quad -E/2 < x < E/2 \tag{44a}$$

$$\text{and}$$

$$h(x) = 0 \quad \text{elsewhere} \tag{44b}$$

which is just a square pulse with an area of unity. The Fourier transform of a single square pulse is:

$$H(q) = \frac{\sin(qE/2)}{(qE/2)} \tag{45}$$

A Taylor series expansion neglecting higher terms gives:

$$H(q) = 1 - \frac{q^2 E^2}{24} \tag{46}$$

and:

$$H^2(q) = 1 - \frac{q^2 E^2}{12}$$

(47)

for small values of qE (e.g. up to qE = 2 there is only a 6% error).

$$I(q) = \frac{Kp}{q^4} - \frac{KpE^2}{12q^2}$$

(48)

and for smeared intensities:

$$I(q) = \frac{Kp\pi}{2} \left(\frac{1}{q^3} - \frac{E^2}{6q} \right)$$

(49)

The transition zone thickness can be obtained from a plot of $I(q)q^2$ vs. q^{-2} for pinhole (desmeared) collimated systems and from $I(q)q$ vs. q^{-2} for smeared intensities. Absolute intensities are not required for transition zone thicknesses but are for Porod constants.

When the interface is assumed to be sigmoidal in shape:

$$H(q) = \exp \left(\frac{-\sigma^2 q^2}{2} \right)$$

(50)

such that:

$$I(q) = \frac{Kp}{q^4} \exp (-\sigma^2 q^2)$$

(51)

The exponent can either be expanded for small q or a plot of $\ln(I(q)q^4)$ vs. q^2 will give σ. The smeared intensity takes an intractable form except for the limit of small q giving:

$$I(q) = \frac{K_{P}\pi}{2q^3} (1 - 2\sigma^2 q^2)$$ (52)

Other profiles can be derived and will be discussed later.

Absolute units can either be calculated by measuring the main beam intensity directly or by using a secondary standard. Most detectors cannot withstand being exposed to the main beam directly, but a transluscent beam stop with a known attenuation factor will give both a scattering curve and the main beam intensity. This is the most accurate method since both are measured simultaneously. A secondary standard, even though less accurate due to fluctuations in the main beam intensity and the intensity at the calibration angle, is easier to use.

For SAXS, absolute smeared intensities are given by:

$$\tilde{i}(q) = \left[\frac{\tilde{I}}{\tilde{I}_c} \right] \frac{aA_c}{CTDA_s}$$ (53)

where:

I = counts/sec for the sample

I_c = counts/sec for the lupolene at d = 150Å

a = sample to detector distance

A_c = transmission coefficient of lupolene

A_s = transmission coefficient of sample

T = Thompson scattering factor (7.9×10^{-26} cm^2)

D = thickness of sample

C = Kratky ratio of I_c to I_O

Then the invariant is given by:

$$\langle \eta^2 \rangle = \frac{1}{2\pi\lambda a} \int_0^\infty q\, \tilde{i}(q)\, dq$$ (54)

and the Porod constant is:

$$\frac{S}{V} = \frac{2\emptyset_1(1 - \emptyset_1)}{\pi a \lambda \overline{\eta^2}} \left(\frac{\partial \overline{i}}{\partial(1/q^3)} \right) \tag{55}$$

For SANS, the intensities are usually obtained in Rayleigh ratios:

$$R(q) = \frac{I a^2}{I_0 V} \tag{56}$$

where V is the volume of the irradiated part of the sample. Rayleigh ratios are most often used in neutron and light scattering, but can also be obtained for SAXS taking into account that the scattering length of one electron is .28 x 10^{-10} cm. The units of R(q) are cm^{-1} yielding an invariant in units of cm^{-4}:

$$<\eta^2> = \frac{1}{2\pi^2} \int_0^\infty R(q) q^2 dq \tag{57}$$

and in the Porod region are:

$$\frac{S}{V} = \frac{\left(\dfrac{\partial R(q)}{\partial q^{-4}} \right)}{2\pi(1 - \emptyset_1)\emptyset_1 \overline{\eta^2}} \tag{58}$$

Chapter 3

EXPERIMENTAL

3.1 Materials

The PVF_2 was provided by Polysciences Inc. (lot #4-0533) with a molecular weight of Mw = 140,000 and an M_n = 80,000. The perdeuterated poly(methyl methacrylate), PMMA(d8), was purchased from Polymer Laboratories with an M_n = 57,000 and M_w/M_n = 1.08. This polymer had been synthesized using an anionic catalyst giving a different tacticity than is found for radically polymerized PMMA. The tacticity (the percentage of each triad) is 7% isotactic, 40% heterotactic and 53% syndiotactic. The hydrogenous polymer, PMMA(h8), used for dynamic mechanical thermal analysis, DMTA was obtained from Polysciences with M_w = 90,000 and M_n = 60,000.

3.2 Blend and Sample Preparation

PVF_2 and PMMA(d8) were dissolved in dimethyl formamide (DMF) at room temperature. The low molecular weight and low concentrations of PMMA both favor dissolution which takes several hours. The DMF was then evaporated in a casting dish for 3 days, yielding thin films of the blend. Excess solvent was removed by placing the blends under vacuum for two additional days. The blends that adhered to the casting dish were removed by adding methanol; after 30 seconds they could be peeled off the glass surface.

The SANS samples were prepared by pressing the films into a sheet 100-200 μ thick at 225°C. The sheets were then cut and stacked to fill a circular mold in which they were pressed for short times at 225°C, and subsequently quenched in ice water until all voids and residual solvent were removed.

Three blends, 10, 20 and 30 weight % PMMA(d8), were remelted in the same mold at 225°C for 10 minutes under vacuum and then quenched in ice water. The mold was subsequently wrapped in aluminum foil and annealed in an oil bath for 24 hours at 145°C. These samples are designated as "Q", for quenched and annealed.

Three blends of similar composition were also wrapped in aluminum foil, melted at 225°C in one oil bath for 10 minutes, and transferred to another bath at 145°C for 24 hours. These isothermally crystallized blends are designated as "M", for melt crystallized. The number that preceeds the letter designation is the weight percent of PVF_2 in the blend (e.g. the sample 90Q contains 90 weight % (86.7 vol. %) PVF_2 and was quenched and annealed at 145°C).

The addition of PMMA to PVF_2 favors the formation of the crystalline form which tends to degrade at high temperatures. The dehydrohalogenation of the chain substituents leads to conjugation along the chain and a brown color in the samples. Thermal gravimetric analysis showed no weight loss occurred at the temperature where isothermal crystallization was performed; elemental analysis showed little or no loss of fluorine, and, therefore, little or no structural change in these samples.

3.3 Methods of Analysis

The SANS intensities were obtained at the 30 meter neutron scattering facilities (λ = 4.75Å) using the High Flux Isotope Reactor (HFIR) at Oak Ridge National Laboratories in Oak Ridge, Tennessee. Three sample-to-detector distances (18, 10 and 2 meters) were employed, the angular calibration being calculated from these values. Absolute intensites were determined for the 18 and 10 meter data using an aluminum standard (A1-4) containing voids with an Rg = 203 ± 3Å and an intercept of $R(q = 0)$ = 130 cm^{-1}. The low incoherent

scattering cross-section ($\sigma_{incoh} < 0.01$) makes this an ideal standard since no background correction needs to be made. The 2 meter intensities were converted into absolute units by scaling the incoherent scattering of PMMA(h8) of the 2 meter data to that at 10 meters. The 2 meter data were divided by a scale factor of 450 and then combined with the other data.

The SAXS intensities ($\lambda = 1.54A$ for Cu K_α radiation) were obtained at the University of Massachusetts using a Kratky camera equipped with a Braun one-dimensional position-sensitive detector and a Canberra Series 35 multi-channel analyzer. Data were transferred to and analyzed on a Digital PDP 11/34 computer. The SAXS intensities were desmeared using FFSAXS3 [79] provided by Dr. C. Vonk. Angular calibrations were determined using a uranyl acetate stained duck tendon. The first six orders of Bragg reflections were used with a base periodicity of 640Å. Absolute intensity calibration was obtained using a Lupolene standard (24/9) provided by Dr. O. Kratky.

Background subtraction is a critical part of data analysis. Background levels in x-rays are due to thermal density fluctuations in the amorphous phase, whether frozen in or randomly occurring in time and space, thermal vibrations of the atoms, lattice defects in the crystal and impurities in the system. Underestimation of the background level is indicated by the scattered intensities not asymptotically approaching zero at large q's. An overestimation, on the other hand, would not be detectable.

There are several ways to subtract a background from a scattering curve for a two-phase system. These methods are divided into two categories: the first is for scattering curves which extend to large 1's such that the entire Porod region is included (the intensity has reached a minimum and has begun to increase); the second type is for those that do not. The choice of the method is controlled by the angular limit of the detector for the sample analyzed.

For the first case, the background intensity can be expressed as a power series in q^2. Two simplifications have been proposed: Ruland [80] compacts the power series into an exponential function (a gaussian):

$$I_b(q) = ae^{bq^2}$$

and Vonk [65] discards all terms except for exponents of either 4 or 6.

$$I_b(q) = aq^4 + aq^6$$

These q-dependent backgrounds are subtracted from the scattering curves.

Two simpler methods can alternatively be used in which the background is assumed to have no q dependence. Either the minimum intensity in the wide angle region [65] or an extrapolation to $q = 0$ for a log I vs. q^2 plot [81-83] can be chosen as the fluctuation scattering. These last two methods overestimate the background scattering, which results in an error of the order of 10% in calculating deviations from Porod's law (transition zone thicknesses) and . slightly diminishes the value obtained for the invariant. These errors, though, are not of great significance making the simpler approach of constant background scattering preferred in most cases.

The method for correcting scattering curves when the intensities at large q's are not available is less accurate, because further assumptions concerning the structure of the samples must be made. This involves the assumption that the system is composed of two phases each with no internal structure such that Porod's law (eq. 10) applies. For desmeared intensities the total scattering can then be expressed as:

$$I(q) = K/q^4 + I_b$$

where I_b is the background scattering level, assumed to be constant. Introducing the effect of a transition zone yields:

$$I(q) = KH^2(q)/q^4 + I_b$$

26

It must, in this case, be assumed that $H^2(q)$ goes to zero at large q's such that a plot of $I(Q)q^4$ versus q^4 has a slope equal to the background scattering and a vanishing intercept. For some cases the intercept is not zero, which is due to the fact that $H^2(q)$ is not zero; Todo, Hashimoto and Kawai [84] however, have shown that the resulting error in the background is within experimental error. This is the method chosen to correct for background scattering for the SAXS intensities in this study. Since the SAXS intensities are smeared, Porod's law is now given by equation 36. Plots of $I(q)q^3$ vs. q^3 are shown in Figures 4 and 5 and the slopes are listed in Table 1.

An alternative method for background correction, often used by Vonk for polyethylene systems, is to measure the background from the melted crystalline sample [85-86]. This is the most accurate technique since the scattering due to heterogeneities can be subtracted along with any residual main beam scattering. This method can also be used with amorphous phase separated polymers such as Kinning's styrene-butadiene block copolymers [87]; similarly, low molecular weight analogs can also be used to determine the background level. These methods are unsuitable for blends with mixed phases though, since Wendorff [50] has shown that concentration fluctuations will contribute significantly to the background scattering. This is the case for crystalline/amorphous blends in which the amorphous polymer resides between the lamellae.

Koberstein [88] has shown that for SANS the background level is dominated by the incoherent scattering in most polymer systems. In $PVF_2/PMMA$ blends, however, the background scattering is complicated by the presence

of concentration fluctuations in the mixed amorphous phase (interlamellar region). It was therefore chosen to assume a constant background, determined by the same method as the SAXS data were corrected. For the SANS intensities equation 62 applies since pinhole collimation was used. Plots of $I(q)Q^4$ versus q^4 are shown in Figures 6 to 8 and the background levels also listed in Table 2.

Chapter 4

RESULTS AND DISCUSSION

4.1 Introduction

The basic goal of this thesis is to study the microstructure of $PVF_2/PMMA$ blends by comparing the small angle neutron and X-ray scattering. The underlying idea is that, if the scattering length density and the electron density profiles of the system are the same, then the intensities from both SANS and SAXS will be identical. The blend of PVF_2 and PMMA provides a good subject for this study. The PMMA resides between the PVF_2 lamellae so that the contrast for both SAXS and SANS is due to the lamellar structure; the high scattering density phase is the crystalline PVF_2 for SAXS and the homogeneously mixed amorphous phase containing PMMA(d8) for SANS.

4.2 Models

Three models are used to describe the concentration of PMMA between the lamellae and the size of the transition zone, where present. The two-phase model consists of regions of constant composition and a sharp interface. For a one-dimensional system the electron density profile of this model corresponds to a series of square pulses. A good example is high density polyethylene which has a relatively small crystalline-amorphous transition zone thickness of <10Å. Three-dimensional systems containing voids, though, are the best representation of a two-phase system with a sharp interface. For the $PVF_2/$ PMMA blend, the first phase is pure crystalline PVF_2 and the other is composed of amorphous PVF_2 homogeneously mixed with PMMA. This system is described by the SAXS and SANS invariant equations (see equations 59 and 60

in section 4.4) with only one unknown (the degree of mixing in the mixed phase).

Morra found that a two-phase model could be used to fit his invariants for the $PVF_2/PMMA$ system [27]. In the present study, however, it has been demonstrated that the same data could also fit a model which assumes that a transition phase is present between the crystalline and the mixed amorphous phases.

The introduction of a transition zone into the blend leads to an increase in both SAXS and SANS invariants. A transition zone will create around the crystals a region void of PMMA. This situation is schematically illustrated for a two-phase model with a linear transition zone in Figure 9. This corresponds to an increase in the concentration of PMMA in the mixed amorphous phase. The invariant for a two-phase system with a linear transition zone (eq. 32) is the product of two parts: a contrast term between the two phases, and a term dependent on the volume fraction of the phases. The contrast term will increase with increasing the transition zone thickness. For the blend of PVF_2 and PMMA, the large differences in the electron densities and scattering lengths of the crystalline PVF_2, amorphous PVF_2 and PMMA (Table 2) will greatly increase the contrast term for both SAXS and SANS as the PMMA is concentrated; the volume fraction term will decrease only slightly. The net effect is a large increase in the invariant upon the introduction of a transition zone. Moreover, the SANS invariant will increase more than the SAXS invariant will, since the contrast between crystalline PVF_2 and PMMA is greater for neutrons than for x-rays.

The linear transition zone model has been applied to a variety of systems (homopolymers [65], copolymers [89,90] and blends [22]) and the deviation from Porod's law due to the interphase has been determined. Modelling this

system using the SAXS and SANS invariants, the square of the deviation of the electron density, $\eta^2(x)$, through the transition zone is a parabola. On the other hand, if a sigmoidal interphase is assumed, $\eta^2(x)$ is a gaussian within this phase. A transition zone with a sigmoidal profile will be slightly larger than that for a linear interphase. The difference between the thicknesses of the two zones, though is negligible within the experimental error. Therefore, in this work the linear transition zone model was chosen.

The three-phase model for the $PVF_2/PMMA$ blend is represented by a crystalline PVF_2 phase, a homogeneously mixed amorphous phase and a transition zone between the two of constant density amorphous PVF_2. This is the model preferred by Wendorff to explain the dielectric relaxation data [60,61]. The model also corresponds to the minimum transition zone thickness that can exist in a system when modelling SAXS invariants. Since the electron density of amorphous PVF_2 is roughly the average electron density of the system, the transition zone will not contribute to the SAXS invariant. It will contribute to the SANS invariant, though, since the scattering length density of amorphous PVF_2 is slightly less than crystalline PVF_2. In fact, the neutron scattering curve for pure PVF_2, shown in Figure 10, shows a peak corresponding to the lamellar spacing due to the density difference of crystalline and amorphous PVF_2. For semicrystalline polymers the coherent scattering is usually much less than the incoherent level. The expected neutron scattering due to crystalline-amorphous density differences calculated from SAXS for iPS (which is comparable to that of most semicrystalline materials) is negligible compared to the incoherent level of polystyrene (Figure 11).

4.3 Scattering and Correlation Functions

A comparison of the scattered intensities divided by their respective invariants is shown in Figures 12-17. There is a large discrepancy between the SAXS and SANS data for all blend compositions and preparations. Furthermore, plots of $I(q)q^2$ vs. q (Figures 18-23) yield two curves (for which the integrated area is $2\pi^2$) enhance the difference between the SAXS and SANS intensities. The scattering maximum occurs at the same angle for both SAXS and SANS indicating an interlamellar placement for the PMMA, but the SAXS intensities at small angles are found to be much higher than the SANS. The large difference in the two intensity profiles can be attributed directly to the scattering in the Porod region. This difference can be related to two features in the microstructure. First, the two scattering profiles are not the same indicating that the blend is not a two-phase structure. Secondly, the SANS intensities are directly related to the concentration profile of PMMA(d8) in the blend, leading us to conclude that the electron density profilie is related to both the concentration of PMMA(d8) and the density changes occurring in PVF_2. This must result from regions of noncrystalline PVF_2. These regions could either be of constant scattering density as shown in the three-phase model or of a varying scattering density as in the linear transition zone model.

The one-dimensional correlation functions determined from the SAXS and SANS intensities are shown in Figures 24-29, respectively. While there is good agreement between the two functions, there is little definition in either. The only major difference is at small x's where there is a noticeable curvature in the SAXS correlation functions, which can again be attributed to a transition zone. Valuable information can be gained from the correlation functions as has been shown by Strobl [91]; however, most of this information is obscured when a high degree of disorder is present in the system, such as bent lamellae,

corrugated surfaces and a large lamellar size distribution. For highly ordered polymers such as polyethylene correlation function analysis is a useful technique to determine microstructural details; however, for most other polymers, and especially for blends, the parameters obtained from Strobl's analysis are often imprecise and misleading. Based upon the comparison of the SANS and SAXS scattering curves and correlation functions, a two-phase model does not fit.

4.4 Invariants

A quantitative analysis of the microstructure can be obtained using the invariants to calculate sizes and compositions of the phases.

4.4.1 Two-Phase Model

For the two-phase model, the only parameter for the invariant equations is the degree of mixing, $\emptyset_c$, of the PVF$_2$ with PMMA in the amorphous phase. The SAXS and SANS invariants are described by:

$$<\eta^2>_{SAXS} = [(\rho 1_c - \rho M) -$$

$$(\rho 1_a - \rho M)\emptyset_c]^2 \left(1 - \frac{\emptyset_M}{1 - \emptyset_c}\right)\left(\frac{\emptyset_M}{1 - \emptyset_c}\right)$$

(59)

and:

$$<\eta^2>_{SANS} = \left[\left(\frac{a_{1c}}{V_{1c}} - \frac{a_M}{V_M}\right) -\right.$$

$$\left.\left(\frac{a_{1a}}{V_{1a}} - \frac{a_M}{V_M}\right)\emptyset_c\right]^2 \left(\frac{\emptyset_M}{1 - \emptyset_c}\right)\left(1 - \frac{\emptyset_M}{1 - \emptyset_c}\right)$$

(60)

33

where the subscripts 1c, 1a and M refer to the PVF_2 crystalline phase, the PVF_2 amorphous phase, and the pure PMMA, respectively. $\emptyset_c$ is the volume fraction of PVF_2 in the PMMA mixed phase (e.g. $\emptyset_c = 0.5$ when there are equal amounts of PVF_2 and PMMA in the mixed phase). From these two equations $\emptyset_c$ can be calculated for both SANS and SAXS as listed in Table 3. These two values should be the same if a two-phase model does fit the invariants. However, the degree of mixing determined from SAXS is on average 60% higher than $\emptyset_c$ determined from SANS. If a SAXS invariant is back calculated from the SANS degree of mixing, then this invariant is 75% greater than the one experimentally determined. A transition zone in this type of system (large differences in electron and scattering length densities so that the dominant term is the contrast between the two phases) will give larger than expected invariants; it will also give a larger invariant for SANS than for SAXS, when compared using the $\emptyset_c$ values.

4.4.2 Linear Transition Model

The second model assumes a linear transition zone. For this system there are two unknowns: the electron density of the PMMA phase and the size of the transition zone. The assumptions used in constructing the model are that there are two phases of constant electron and scattering length density. The electron density profile has a linear gradient between these two phases and the interphase has a thickness E and a total volume fraction of $\emptyset_e$ ($\emptyset_e = 2E/L$, where L is the sum of the crystalline, amorphous and transition zone thicknesses). The transition zone is broken up into two parts. The first fraction corresponds to the decrease in the electron density from that of crystalline to amorphous PVF_2. This section contains no PMMA or no PMMA can penetrate any region of PVF_2 which has a density greater than that of amorphous PVF_2.

In the second part of the transition zone the electron density decreases from that of amorphous PVF_2 to the density of the mixed amorphous phase. This region contains PMMA and will contribute to the SANS scattering curve and invariant. The first part of the transition zone, on the other hand, will have little effect on the SANS scattered intensities and a small but not negligible effect on the SANS invariant. The equation for the SANS invariant will include contributions from two transition zones and is given by:

$$<\eta^2> = \eta^2{}_{1cN}\,\emptyset_1 + \eta^2{}_{2N}\,\emptyset_2 + <\eta^2{}_{E1N}>\emptyset_{E1} + <\eta^2{}_{E2N}>\emptyset_{E2} \qquad (61)$$

while for SAXS the transition zone is smooth:

$$<\eta^2> = \eta^2{}_{1cx}\,\emptyset_1 + \eta^2{}_{2x}\,\emptyset_2 + <\eta^2{}_{Ex}>\emptyset_E \qquad (62)$$

These equations are solved by iterating over values for $\emptyset_c$ and e and the results are listed in Table 4. Using these data, the volume fraction of crystalline, $\emptyset_1$, and homogeneously mixed amorphous phase, $\emptyset_2$, are determined from:

$$\emptyset_1 = 1 - \emptyset_e = \emptyset_2 \qquad\qquad \emptyset_2 = \frac{\emptyset_M}{1 - \emptyset_c} - \frac{\emptyset_{E1}}{2} \qquad (63)$$

and are listed in Table 4. Figures 30-35 show plots of $I(q)q$ vs. q^{-2} from which transition zone thicknesses were measured using equation 49 (Table 5). The Porod constants can be calculated from the slope of this plot and from them the surface-to-volume ratios, S/V, can be determined (Table 5). The surface-to-volume ratio for a one-dimensional system should be equal to twice the inverse of the long spacing, 2/L. The parameter of SL/2V is listed for the different samples in Table 5, and it is found to be greater than one for all the blends.

The disagreement could be due to error in the Porod constant, a small crystalline lamellar width so that correlations parallel to the lamellae cannot be neglected, or a rough crystallite surface which would increase the total surface area in the structure. The latter is more likely since defects in the chain would be rejected to the crystal face creating pockets of noncrystalline material along the surface. Transition zone thicknesses from SANS intensities were not determined due to lack of resolution and large fluctuations in the scattered intensities at large q's.

The agreement between the transition zone thicknesses calculated from the Porod region and from modelling is poor, but still within error limits. The error in determining the thickness from the Porod region is large and subject to errors in background subtraction and fluctuations at large q. Values for $\emptyset_1$ have also been determined from DSC and are listed in Table 4 along with those from the model. There are several problems in measuring the percent crystallinities of PVF_2 and its blends. The most serious comes from the existence of several crystalline forms, because the enthalpy of fusion is known only for the most common form, the α phase [tgtg] [92]. Crystallizing in the presence of any material that PVF_2 has favorable interactions with enhances the formation of the β phase [tt] [61]. Since the PMMA is highly miscible with PVF_2, the blend will contain both α and β crystalline phases. It is assumed that the enthalpy of fusion of the β phase is the same as that of the α phase. However, it is more likely that the β phase, which is more dense, has a larger enthalpy of fusion so that the values from DSC would be overestimated. The agreement between the model and the percent crystallinities from DSC is fair.

The homogeneously mixed amorphous phase is predominantly PMMA. Table 6 lists values for the volume fraction of PMMA in this phase with respect to the volume of the amorphous phase $(1 - \emptyset_c)$ and with respect to the total

PMMA in the blend ($\emptyset_q$), and also the fraction of PMMA in the transition zone relative to the total blend volume ($\emptyset_{mt}$). The similarity in the first two values is coincidental, but their variation as the blend composition is changed shows that the amorphous phase becomes more and more concentrated in PMMA on addition of PMMA to the system. Furthermore, from the values for $\emptyset_{mt}$, for all blend compositions a constant amount of PMMA is present in the transition zone: when more PMMA is added it will be rejected to the amorphous phase.

4.4.3 Three-Phase Model

The third model is composed of three phases: crystalline PVF_2, a homogeneously mixed PVF_2-PMMA phase, and a transition zone of amorphous PVF_2. All the PMMA is contained in the mixed amorphous phase. Wendorff favors this model to describe the microstructure of PVF_2/PMMA blends, mainly due to the presence of a β relaxation peak in the dielectric curves. He concludes that there must be an amorphous PVF_2 component. He then uses SAXS to fit the invariants either to a two- or three-phase model. Wendorff concludes that "there is local phase separation due to the presence of this amorphous interface which expels the PMMA despite its favorable interaction with PVF_2". Recently, an upper critical solution temperature, UCST, has been proposed [48] to exist in PVF_2-PMMA blends at 130°C. This finding should have no effect on Wendorff's and this work, since crystallization was carried out at a higher temperature. The results of Wendorff's SAXS analysis will be reviewed later. Even though the three-phase transition zone must have different properties than those of bulk amorphous PVF_2, for convenience we will use the electron and scattering length densities of amorphous PVF_2 (the density of this phase will be addressed later).

The SAXS and SANS invariants for the three-phase model are:

$$<\eta^2_{SAXS}> = <\eta^2_{1cx}>\emptyset_1 + <\eta^2_{2x}>\emptyset_c + <\eta^2_{ex}>\emptyset_c \tag{64}$$

and:

$$<\eta^2_{SANS}> = <\eta^2_{1cN}>\emptyset_1 + <\eta^2_{2N}>\emptyset_2 + <\eta^2_{cN}>\emptyset_c \tag{65}$$

Again these were solved by iterating through values of $\emptyset_c$ and $\emptyset_e$.

The values for $\emptyset_e$ are listed in Table 7. They correspond to the minimum transition zone thickness that must exist in this system. The volume fractions of the interphase in the system range from 20% to 25%, and such values are more amenable to physical intuition than those calculated from the linear transition zone model. By neutron scattering the three-phase system appears as a quasi-two phase system, accounting for the large SANS invariant and the high concentration of PMMA in the amorphous phase.

The percent crystallinity of the PVF_2 calculated with respect to its volume fraction in the blend remains constant (45%) over the composition range of 0-30 wt.% PMMA. This agrees very well with data obtained from DSC measurements. The volume fraction of PVF_2 in the mixed amorphous phase with respect to the total blend volume is also found to be constant (18%), and the volume fraction of transition zone is constant (20%) as well.

The transition zone thicknesses can be calculated from the Porod region. We first choose two square pulses $\rho_1(x)$ and $\rho_2(x)$ where ρ_1 has a width of C + E and ρ_2 has a width of C. The smoothing function, h(x), is for this case a pair of delta functions a distance E apart centered around the origin giving:

$$h(x) = \frac{1}{2}\delta\left(x + \frac{E}{2}\right) + \frac{1}{2}\delta\left(x - \frac{E}{2}\right) \tag{66}$$

The function $\rho_e(x)'$ represents the three-phase model with the exception that the transition zone electron density is midway between those of the crystalline and amorphous phases (Figure 36). The real electron density profile is given by:

$$\rho^e(x) = \overgroup{\rho_1(x)\, h(x)} + A\rho_2(x) \tag{67}$$

where $\rho_2(x)$ controls the height of the crystalline electron density weighted by the constant A, $[A = (\rho_{1c} - \rho_{1a})/(\rho_{1c} - \rho_2)]$. The scattered intensity is given by:

$$I(q) = \int_0^\infty \left[\int_0^\infty \rho^e(x)\, \rho^e(x^1 + x)\, dx \right] \cos qx\, dx \tag{68}$$

or:

$$I(q) = FT\left[\overset{2}{\overgroup{\widetilde{\rho_1(x)\, h(x)}}} \right] +$$

$$2A\left[\overgroup{\rho_1(x)\, \widetilde{h(x)\, \rho_2(x)}} \right] + FT\left[\overset{2}{\widetilde{\rho_2(x)}} \right] A^2 \tag{69}$$

The Fourier transform of $h(x)$ is $\cos(Eq/2)$, and that of the auto-correlations of the square pulses $[\rho_1(x)$ and $\rho_2(x)]$ is Porod's law at large q. The cross term reduces to zero since one of the assumptions of Porod's law is that r is small; in this case $r < E$ giving:

$$I(q) = \frac{K}{q^4} \cos^2 \frac{Eq}{2} + \frac{A^2 K}{q^4} \tag{70}$$

and for small qE then:

$$I(q) = \frac{K}{q^4}\left(1 + A^2 - \frac{E^2 q^2}{4} \right) \tag{71}$$

39

The parameter A must be calculated from the model (if it is not known, it can be neglected for these blends since the electron density of the PVF_2 amorphous phase is close to the average of the other two phases). The values for $\emptyset_e$ calculated from the Porod region are also listed in Table 7 for comparison with those from the model. The interphase thicknesses determined from the model and from the Porod region again do not agree. The agreement appears to be better for this model than for the linear transition zone model, but the values of the Porod region-to-model thickness ratios for both cases is about the same.

4.5 <u>Comparison with Literature</u>

This section will compare the invariants and long spacings obtained in this work with those determined by Morra and Wendorff. Briefly, Morra's invariants are slightly smaller than those measured in this work and Wendorff's are slightly larger. The values for the long spacings found in this study are in agreement with those found by Morra except for the spacing of the 30 wt.% PMMA blend which is 15% smaller. Morra concluded that all of the PMMA was rejected to the interlamellar region leading to an increase in the long spacing with PMMA concentration (Wendorff found similar results). The invariants and long spacings for this work and Morra's are listed in Table 8 for comparison.

The basic difference in the measured invariants occurs for the 20% PMMA blend which, from this work, is 26% higher. Morra draws a curve (Figure 37) through his invariants vs. composition assuming the 30 wt.% PMMA blend invariant is overestimated since he used a two-phase model to fit his data. However, if his data are analyzed considering the invariant of the 20 wt.% PMMA blend to be low, then the curve through his points will pass through a maximum at 30 wt.% PMMA. In fact, using equation 65 for a three-

phase model and assuming that the transition zone thickness is 20%, the ratio of the percent crystallinity to the volume fraction of PVF$_2$ in the blend is constant (45%) and that 18% of the PVF$_2$ is contained in the mixed amorphous phase (all determined from these experiments) then by differentiation the maximum in the invariant curve occurs at 37.7 vol.% or 30 wt.% PMMA(d8). A maximum is expected due to the two competing contributions to the invariant. As PMMA is added to the blend, the contrast term greatly increases with the product of the volume fractions of each of the phases changing little. When the PMMA content becomes high the product of the volume fractions will drop sharply with PMMA concentration causing the invariant to decrease. A maximum will occur between these two extremes. A maximum would also be expected for the linear interface model, but there are not enough constant parameters in the system to find its location. With respect to the argument presented above, the findings of Morra agree well with the presence of a transition zone, also determined by this work.

Wendorff has used Strobl's analysis of one-dimensional correlation functions to obtain crystalline phase sizes and invariants. A brief outline of Strobl's analysis will be given to understand Wendorff's work. Strobl's one-dimensional correlation function (K(z)) is given by:

$$K(z) = \frac{1}{2\pi^2} \int_0^\infty I(q) q^2 \cos qz \, dq \qquad (72)$$

and is defined at $K(0) = <\eta^2>$. This is the normalized one-dimensional correlation function described in equation 19 multiplied by the invariant for the system being studied. The simplest one-dimensional model to describe lamellae is an equally spaced series of identical square pulses as given in Figure 38a.

The correlation function, shown in Figure 38b, is a series of triangles with the properties:

$$K(0) = \emptyset_1\emptyset_2 (\rho_1{}^e - \rho_2{}^e)^2 \tag{73}$$

$$K(Z) = 0 \qquad Z = \emptyset_1\emptyset_2 L \tag{74}$$

$$K(Z) = minimum \qquad Z = \emptyset_1 L \tag{75}$$

The slope of the self correlation triangle $(x < c)$ is:

$$\frac{dK(z)}{dz} = \frac{-(\rho_1^e - \rho_2^e)^2}{L} \tag{76}$$

All these relations hold for a two-phase model. With the introduction of a distribution of crystallite sizes and long spacings along with a transition zone the correlation function loses its definition as illustrated in Figure 38c. The above relations still hold, but the distribution of long spacings and crystallite sizes damps out structure at large z and adds curvature at all minima and maxima except at small z's. The transition zone causes curvature in the correlation function at $z < E$ and can be shown that $\gamma'(0) = 0$ for linear and sigmoidal transition zones. In the region $E < z < C_{min}$ (where C_{min} is the minimum crystallite size) the one-dimensional correlation function is linear. The slope of this line is given by equation 76 and its intersection with $K(z) = 0$ is given by equation 74. Extrapolation of the linear portion of the correlation function to $z = 0$ gives the quantity Q, the ideal two-phase invariant. This value, when a linear transition zone is present in the system, will differ from $K(0)$ by the factor:

$$Q - K(O) = (\rho_1^e - \rho_2^e)^2 \frac{\emptyset_E}{6} \tag{77}$$

Q is the invariant for an ideal two-phase model with sharp boundaries, while K(0) includes the effect of the transition zone. It is this Q that Wendorff defines as his invariant.

Considering the one-dimensional correlation function for a three-phase model, the electron density profile and its correlation function are represented in Figure 39. The one-dimensional correlation function is expressed as:

$$\gamma(x) = \eta_a^2(a - x) + 2\eta_b^2(b - x) + \eta_c^2(c - x) + 2\eta_b(\eta_a + \eta_c)x$$
$$\text{for } 0 \leq x \leq b \tag{78}$$

and:

$$\gamma(x) = \eta_a^2(a - x) + \eta_c^2(c - x) + 2\eta_a\eta_c(x - b) + 2\eta_b(\eta_a + \eta_c)b$$
$$\text{for } b \leq x \leq a \tag{79}$$

Differentiating the correlation function with respect to x gives:

$$\frac{d\gamma(x)}{dx} = -(\eta_a - \eta_b)^2 - (\eta_b - \eta_c)^2 \quad \text{for} \quad 0 \leq x \leq b \tag{80}$$

and:

$$\frac{d\gamma(x)}{dx} = -(\eta_a - \eta_c)^2 \quad \text{for} \quad b \leq x \leq a \tag{81}$$

so that an extrapolation of the region $b < x < a$ through the point $\gamma(b)$ to the origin gives:

$$Q = \eta^2_a a + \eta^2_c c + 2\eta_b\eta_a b + 2\eta_b\eta_c b - 2\eta_a\eta_c b \tag{82}$$

which is not equal to:

$$\overline{\eta^2} = \eta_a^2 a + 2\eta_b^2 b + \eta_c^2 c \tag{83}$$

43

used by Wendorff.   The difference between the two values is:

$$Q - \overline{\eta^2} = 2\eta_b b(\eta_a + \eta_c - \eta_b) - 2\eta_a \eta_c b$$

The first term is negligible since η_b and the term in the parentheses will be close to zero giving:

$$Q - \overline{\eta^2} = -2\eta_a \eta_c b$$

Therefore, Wendorff's x-ray invariants from Strobl's analysis should not be used to calculate phase sizes for the three-phase model.   His invariants are the same as Morra's and this work's within experimental error.   So the micro-structure does not need to be composed of three phases to fit these data.

4.6 Error Analysis

There are several sources of uncertainty in these experiments.   The first point of uncertainty is in the measurement of the invariants, mainly obtaining absolute intensities and subtracting a background.   Background subtraction was discussed earlier in the experimental section.   The use of a secondary standard, measuring I by an indirect means, leads to a 5-10% error.   The values listed in Tables 4 - 7 are for a 15% error in the invariants.   This excess error includes problems in knowing the crystalline phase density and the composition of the amorphous phase.   All parameters for each model were calculated using the average electron density for the α and β phases with respect to their volume fractions (61).   Since up to 50% of the crystals are in the all trans configuration (β phase) the electron density of the crystalline phase is a pair of δ functions.   But including this effect in the calculation leads to a difference of less than 5% from using the average electron density.

The PMMA concentration in the amorphous phase varies due to distributions in crystalline and amorphous phase size. If the concentration of the PMMA between the lamellae is represented as a pair of delta functions, the largest error that can be produced is 10% (for a PMMA content of 20% with delta functions at 10% and 30%). For a gaussian distribution of PMMA concentration obtained from Vonk's theoretical correlation function analysis the error is less than 5%. The effect due to PMMA concentration variations and crystalline density variations due to the presence of the β phase are present. Therefore, a good estimate of the maximum possible error is 15%.

Another source of uncertainty in these experiments is the value of the amorphous phase density for the three-phase model. This phase was assumed to have the density of amorphous PVF_2. However, the PVF_2 phase could have a density between that of the crystalline phase and the amorphous phase. The density of the amorphous PVF_2 phase was allowed to vary in order to estimate the effect on the transition zone thickness. As might be expected, changing the electron density of this phase only affects the contrast terms (since the major change occurs in the average electron density) so that the transition zone thickness remains constant. The parameter that varies is the composition of the homogeneously mixed amorphous phase. Therefore, since the parameter of interest is the phase size of the transition zone, this effect can be neglected even though it is important since it would be valuable to determine the exact electron density profile of the transition zone.

The final point of controversy in all PVF_2 studies, and especially for its compatible blends is the degradation of PVF_2 at elevated temperatures (93). PVF_2, in the α form, will not degrade, but when the β and γ phases are present the main chain dehydrohalogenates, leading to conjugation along the chain and crosslinking between chains (93). The samples used in this work contain β phase crystals and show a yellow-brown color indicating conjugation. Elemental analysis on the blends studied, listed in Table 8, shows no fluorine loss during crystallization. Therefore, the electron density of the crystalline phase did not need to be modified.

Chapter 5

CONCLUSIONS

In summary, the SAXS and SANS intensities have been compared and their invariants used to calculate parameters describing the microstructure of PVF_2/PMMA blends for three models.

The two-phase model, used by Morra, has been found to be inadequate by comparison of the scattered intensities. A difference greater than 60% was found between the concentration of PMMA in the mixed amorphous phase resulting from the SAXS and SANS invariants, respectively.

The linear transition zone and three-phase models each have two parameters which characterize the system. These parameters have been calculated for each model and found to agree with percent crystallinities from DSC within experimental error.

It has been determined that there must be a transition zone of at least 20Å between the crystalline and amorphous phases. The three-phase model has a transition zone thickness of 20-25Å and is composed of pure PVF_2. The interphase in the linear transition zone model is approximately 50Å thick and a fraction of it ($\sim$ 20-25Å) is composed of pure PVF_2 of gradually decreasing density. This fraction contains cilia and loose folds which can also explain the presence of a PVF_2 relaxation in the dielectric relaxation spectrum. Both of these models can explain the scattering and the thermal analysis data.

This method of invariant analysis is far more accurate for determining transition zone thicknesses than measuring deviations from Porod's law. The errors in the invariants are smaller than the errors due to background

subtraction and statistical fluctuations in the tail portion of the scattering curve used for the Porod analysis.

Chapter 6

SUGGESTIONS FOR FURTHER WORK

The combination of SAXS and SANS has been proven by this study to provide an excellent method for studying the morphology and transition zones of crystalline-amorphous polymer blends.

A similar investigation could be applied to a variety of systems in which rejection of the less readily crystallizable species occurs during crystallization. By varying the miscibility of the two polymers from a highly miscible to a semicompatible state a variety of morphologies can be obtained. This chapter outlines possible future studies on several crystalline-amorphous polymer pairs.

Future studies in this field should first focus on similar polymer-polymer blends such as PEO with PMMA or iPS with PPO. These blends also reject the noncrystallizable polymer to the interlamellar regions. Scattering studies of these two blends would yield different information. Since PEO is synthesized by an anionic process it should have no branches and therefore a small transition zone. Preliminary experiments by T. Russell have shown this to be true. On the other hand, iPS is known to have branches and would therefore have a large transition zone. These results are intuitive but should be confirmed.

Similar to these is the blend of iPS and aPS. Wai has shown from x-rays that the aPS is rejected to the interfibrillar region, and preliminary SANS by this worker has confirmed this result. The scattering patterns can be divided into two regions, the Guinier region where the log I decreases with q^2 and the Porod region where the log I decreases linearly with the log q^{-4}. Phase sizes and surface to volume ratios can be measured from these. A more interesting

part is using iPS and epimerized iPS blended with fully deuterated aPS. Epimerized iPS is chemically modified iPS in which the isotacticity is lowered. This would then provide the opportunity to study secondary crystallization by SALS and to observe the microstructure by SANS.

The most interesting type of blend to study is a crystalline-amorphous semicompatible polymer blend such as iPS-PVME or aPS-iPVME. The idea is that by varying the thermal treatment of the blend and thereby the relative rates of phase separation and crystallization a variety of morphologies and properties can be developed from one polymer pair.

The first step is to choose the molecular weights of both polymers such that the LCST of the mixture lies near the T_m of the crystallizable component. An LCST well below the T_m will make the system unmanageable to study, and an LCST well above the T_m would remove the possibility of studying both . phenomena simultaneously.

The next phase of this study is to examine the rates of phase separation and crystallization by SALS and optical microscopy. Rates of phase separation should be measured at temperatures T_m and at high concentrations of the crystallizable polymer.

The final stage is to generate a series of morphologies by choosing temperatures at which the growth rates differ. The properties of this blend should then be correlated to the morphology.

At the present time, scattering studies on these types of blends is limited by the accuracy of the apparatus. Improving the accuracy of SANS and SAXS measurements which are tied to an absolute calibration standard is by far the most important contribution that could be made.

Appendix 1

TABLES

Table 1

The background intensities determined from
Iq^3 vs. q^3 (SAXS) or Iq^4 vs. q^4 (SANS) plots.

	I_b SAXS	I_b SANS
90Q	1.02×10^{25}	.42
80Q	1.07×10^{25}	.43
70Q	1.07×10^{25}	.39
90M	1.05×10^{25}	.42
80M	1.17×10^{25}	.42
70M	1.18×10^{25}	.39

Table 2

Electron densities and scattering lengths
for PMMA and PVF_2.

	$\rho^e \times 10^{23}$ (e/cm^3)	a/V (cm^{-2})
PMMA	3.90	7.12
Amorphous PVF_2	5.06	2.68
Crystalline PVF_2 (α)	5.78	3.08
Crystalline PVF_2 (β)	5.92	3.16

Table 3

Calculated volume fraction of PMMA rich phase
from the SANS and SAXS invariants.

	$\varnothing_c$ SANS	$\varnothing_c$ SAXS
90Q	.48	.71
80Q	.34	.55
70Q	.29	.45
90M	.52	.72
80M	.35	.55
70M	.29	.46

Table 4

Volume fractions of the three phases compared with the volume fraction percent crystallinity determined by DSC for the linear transition zone model.

	$\emptyset_c$	$\emptyset_e$	$\emptyset_2$	$\emptyset_1$	$\emptyset_1(DSC)$
90Q	.41 ± .07	.54 ± .15	.11 ± .06	.35 ± .15	.43
80Q	.30 ± .06	.53 ± .12	.23 ± .06	.24 ± .12	.36
70Q	.27 ± .05	.46 ± .09	.39 ± .06	.15 ± .09	.29
90M	.49 ± .06	.47 ± .15	.15 ± .06	.38 ± .15	.42
80M	.31 ± .06	.52 ± .12	.24 ± .06	.24 ± .12	.35
70M	.28 ± .05	.41 ± .09	.41 ± .06	.18 ± .09	.29

Table 5

Transition zone thicknesses and surface to volume ratios
obtained from the Porod region compared with
the transition zone thicknesses from the two invariants.

	$\emptyset_e$ (MODEL)	$\emptyset_e$ (Porod)	S/V	SL 2V
90Q	.54	.19	.0199	1.74
80Q	.53	.23	.0117	1.08
70Q	.46	.27	.0186	1.72
90M	.47	.21	.0211	1.85
80M	.52	.24	.0132	1.23
70M	.41	.24	.0164	1.56

Table 6

The volume fraction of the PVF$_2$ rich phase,
the volume fraction of PMMA in the PMMA rich phase
and the fraction of PMMA contained in the transition zone
for the linear transition zone model.

	$(1-\emptyset_c)$	$\emptyset_q$	$\emptyset_{MT}$
90Q	.59	.49	.07
80Q	.70	.63	.10
70Q	.73	.77	.09
90M	.51	.58	.06
80M	.69	.64	.09
70M	.72	.79	.08

Table 7

Volume fractions of the three phases compared with the volume fraction percent crystallinity determined by DSC for the three-phase model.

	$\emptyset_c$	$\emptyset_1$	$\emptyset_2$	$\emptyset_3$	(Porod)
90Q	.55 ± .04	.43 ± .08	.30 ± .04	.27 ± .08	(.10)
80Q	.40 ± .04	.33 ± .06	.43 ± .04	.24 ± .06	(.13)
70Q	.33 ± .04	.24 ± .04	.56 ± .04	.20 ± .04	(.15)
90M	.58 ± .04	.43 ± .08	.32 ± .04	.25 ± .08	(.10)
80M	.41 ± .04	.33 ± .06	.44 ± .04	.23 ± .06	(.14)
70M	.34 ± .04	.26 ± .04	.56 ± .04	.18 ± .04	(.13)

Table 8

Comparison of d-spacings and invariants
from this work with Morra's work.

	d spacings Å		invariants (I^2/cm^6)	
	fit from Morra data	this work	Morra	this work
90	166Å	175Å	2.35	2.83
80	194Å	190Å	2.85	3.87
70	229Å	190Å	4.17	4.19

Table 9

Results from elemental analysis
on the PVF$_2$/PMMA blends.

	% Fluorine	
	measured	ideal
90	.525	.535
80	.476	.475
70	.417	.416
Standard*	.422	.426

*PVF$_2$/PMMA (h8) blend

Appendix 2

FIGURES

Figure 1.   DMTA of pure PVF$_2$, pure PMMA, a 90/10 and 80/20 blend of PVF$_2$ with PMMA.

tan δ (DMTA)

.12

PVF₂

90/10

PMMA

80/20

TEMPERATURE (°C)

-100   -50   0   50

63
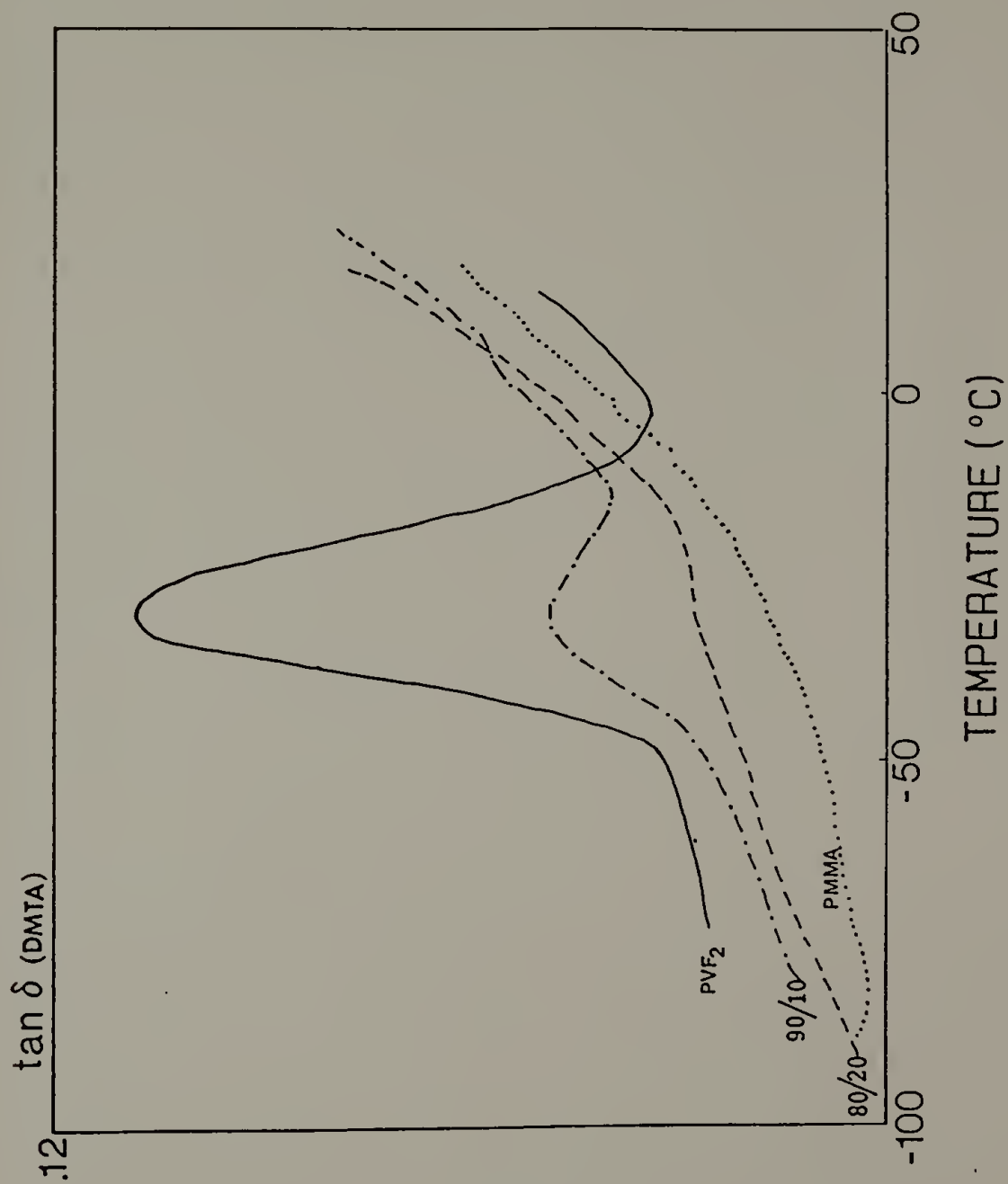
Figure 2.   Electron density profiles and the square of the devia-
tion of the electron density from the average electron
density for three model systems.
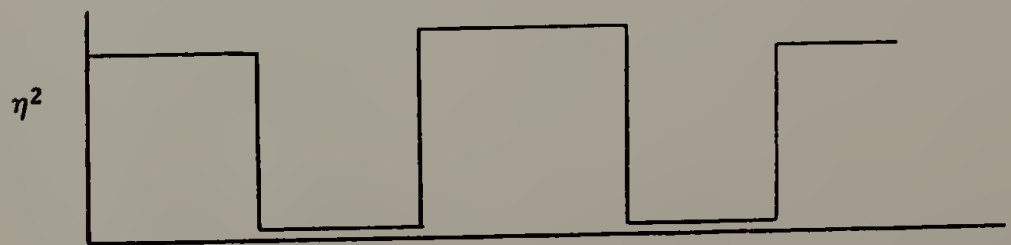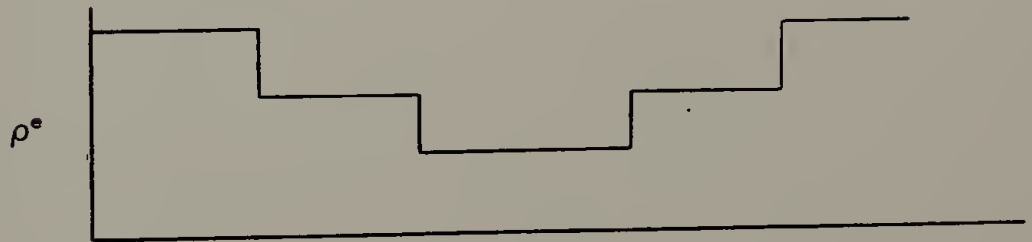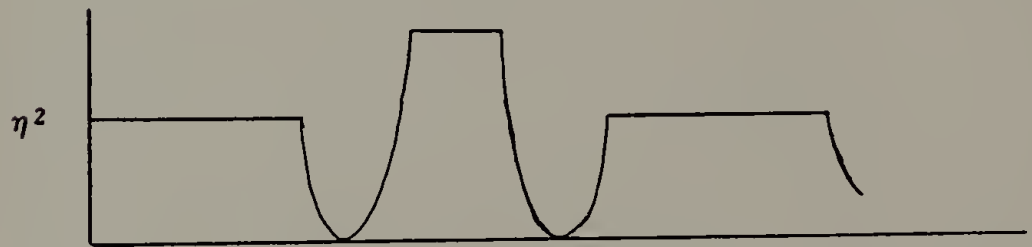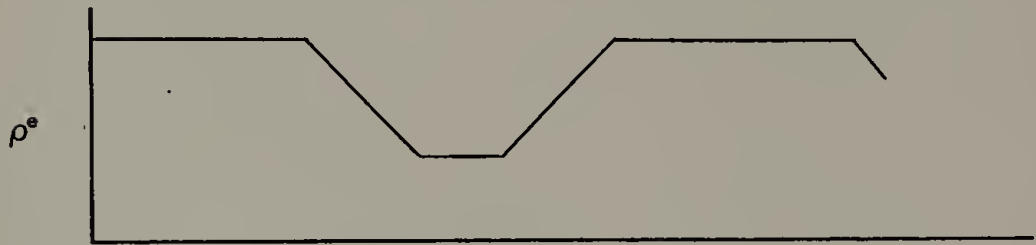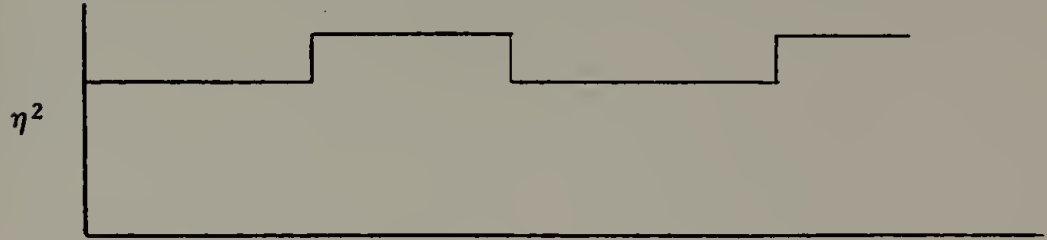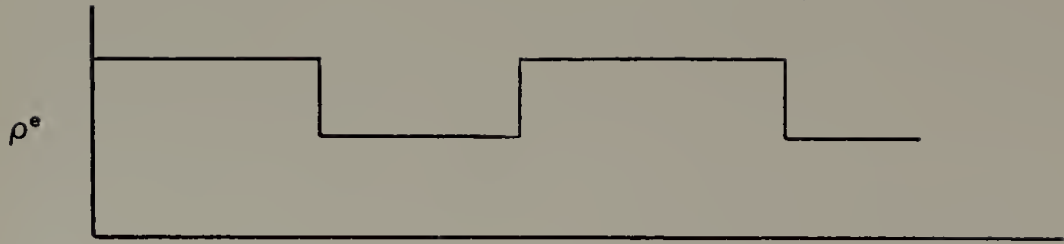
Figure 3.   Relation between smeared and desmeared scattering angles.
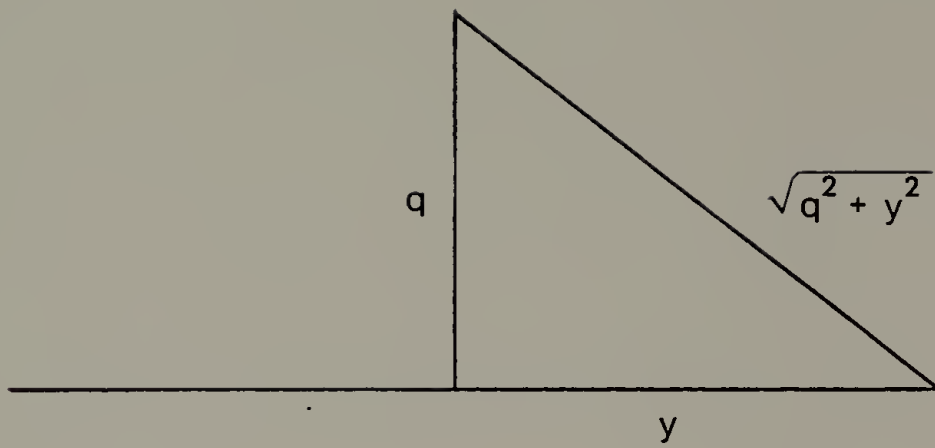
Figure 4. Iq^3 vs. q^3 SAXS smeared intensities for 90 PVF$_2$/10 PMMA blend (quenched).
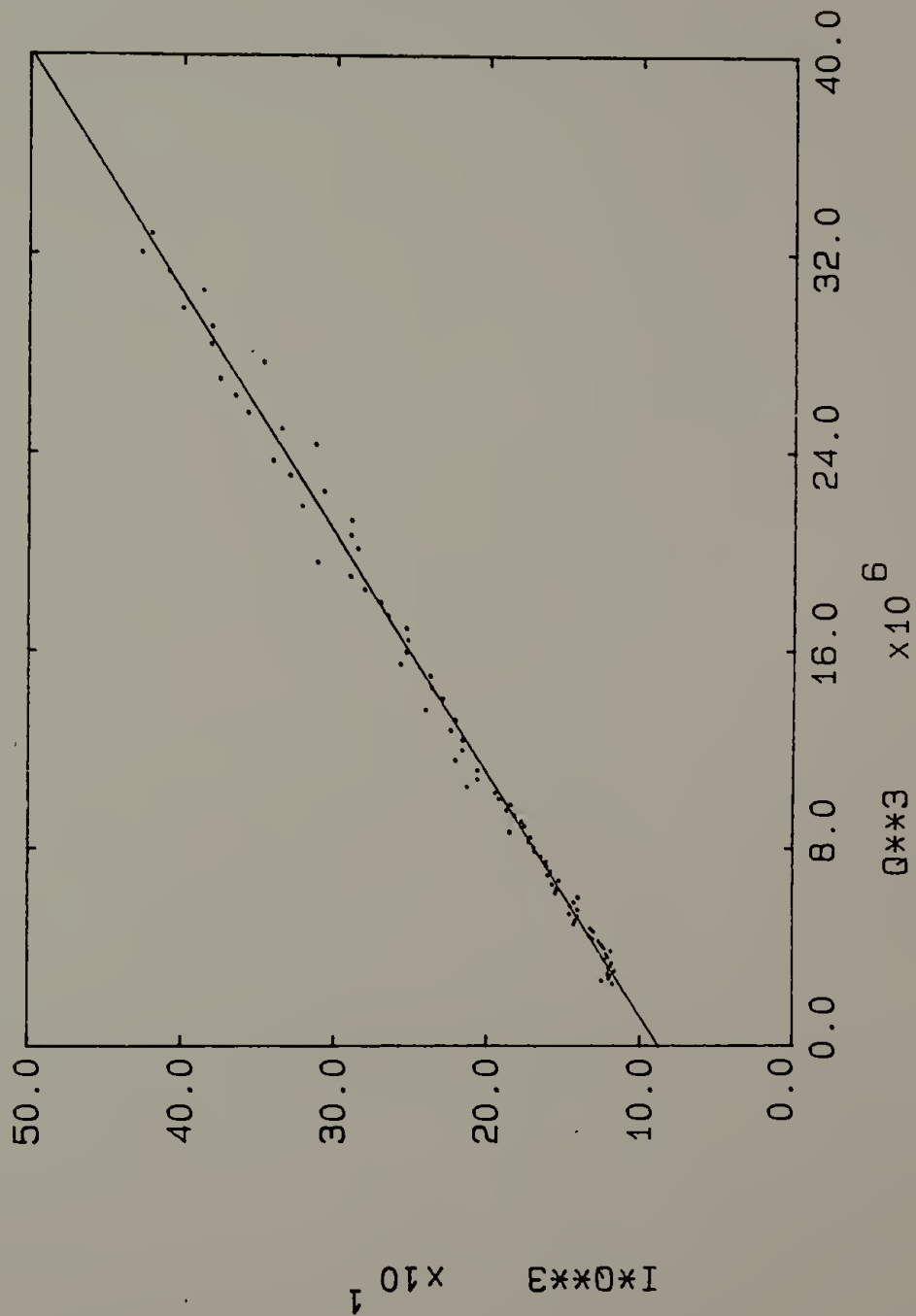
Figure 5. Iq^3 vs. q^3 SAXS smeared intensities for 80 PVF_2/20 PMMA blend (quenched).
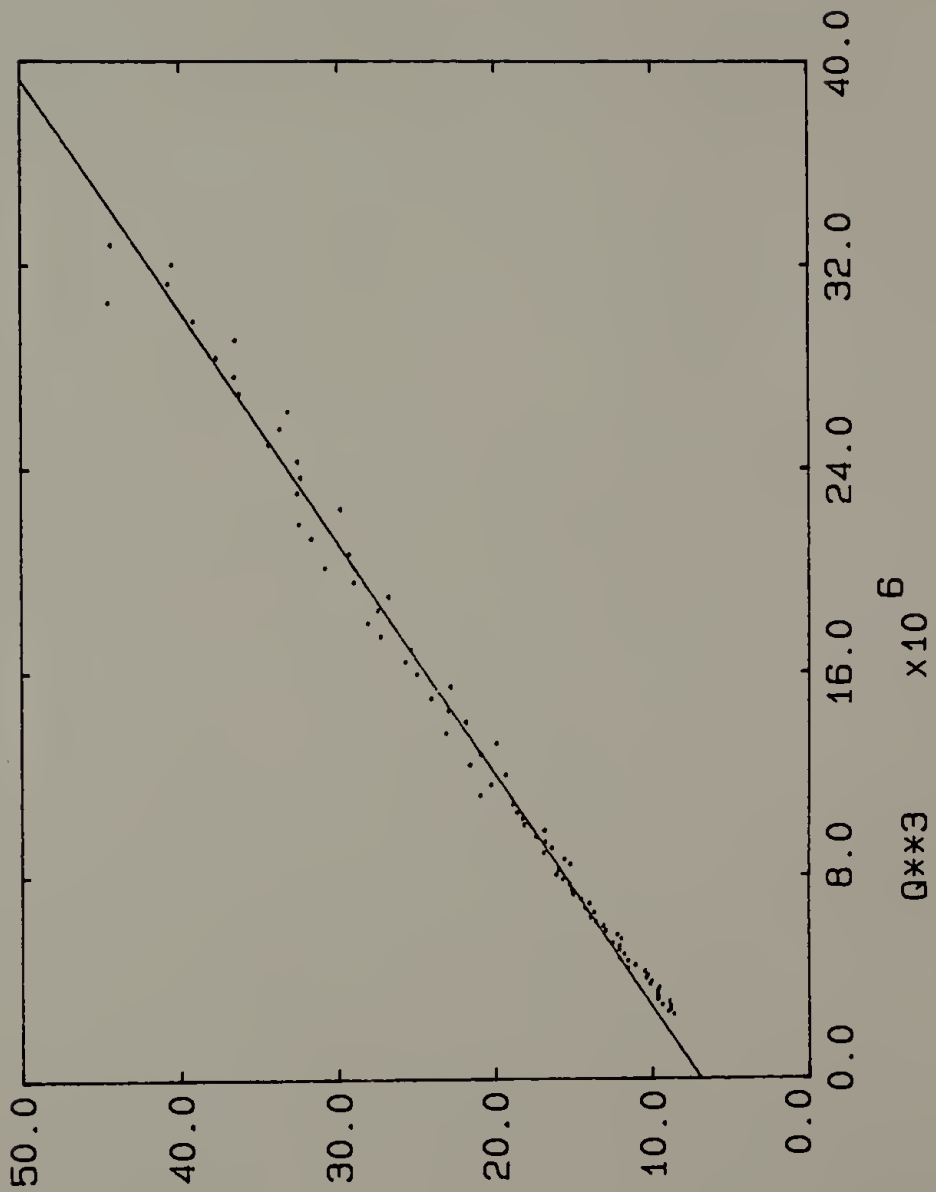
Figure 6. Iq^4 vs. q^4 SANS intensities for 70 PVF$_2$/30 PMMA blend (melt cryst.).
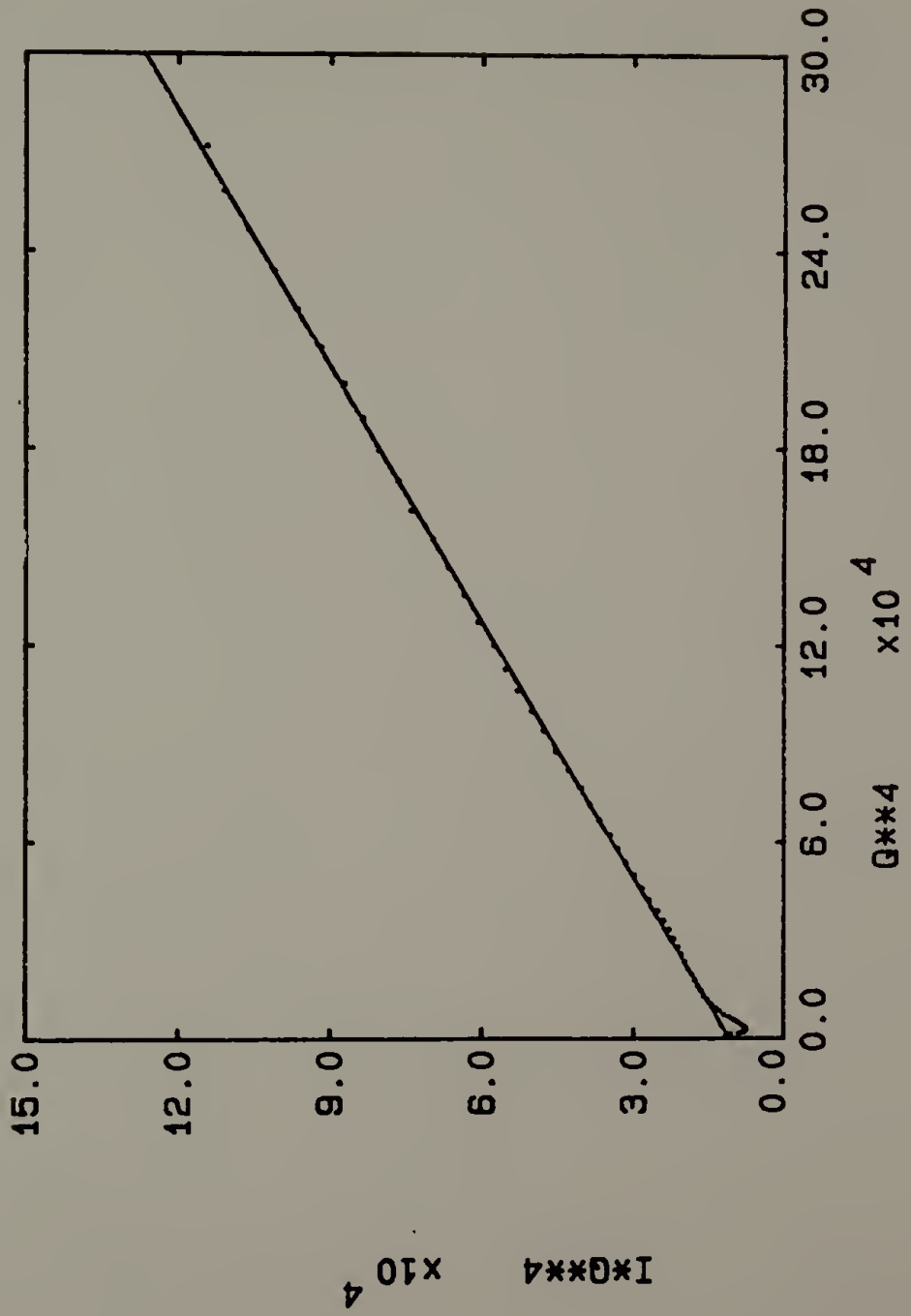
Figure 7. Iq^4 vs. q^4 SANS intensities for 90 PVF$_2$/10 PMMA blend (quenched).
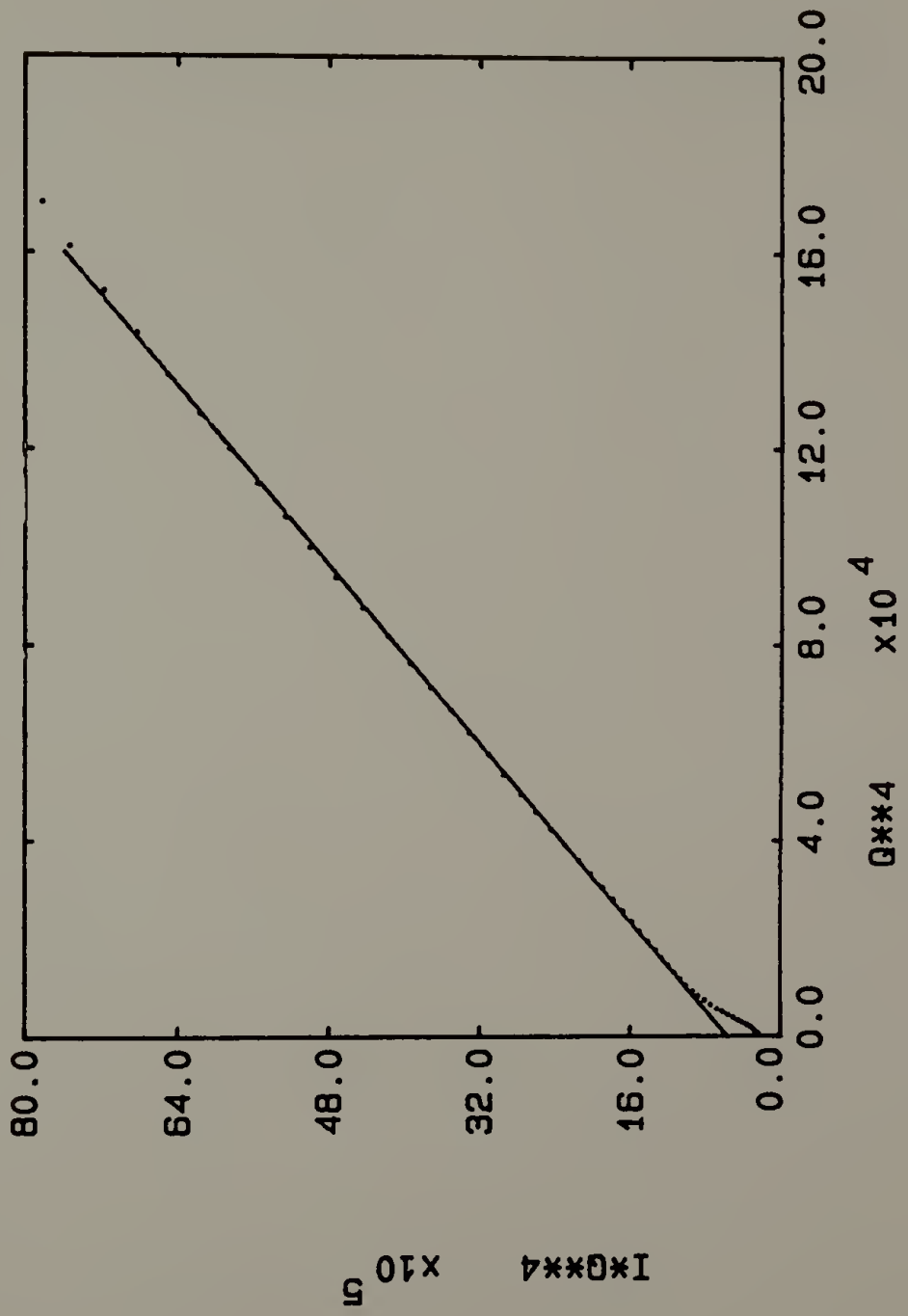
Figure 8. Iq^4 vs. q^4 SANS intensities for 80 PVF_2/20 PMMA
blend   (quenched).
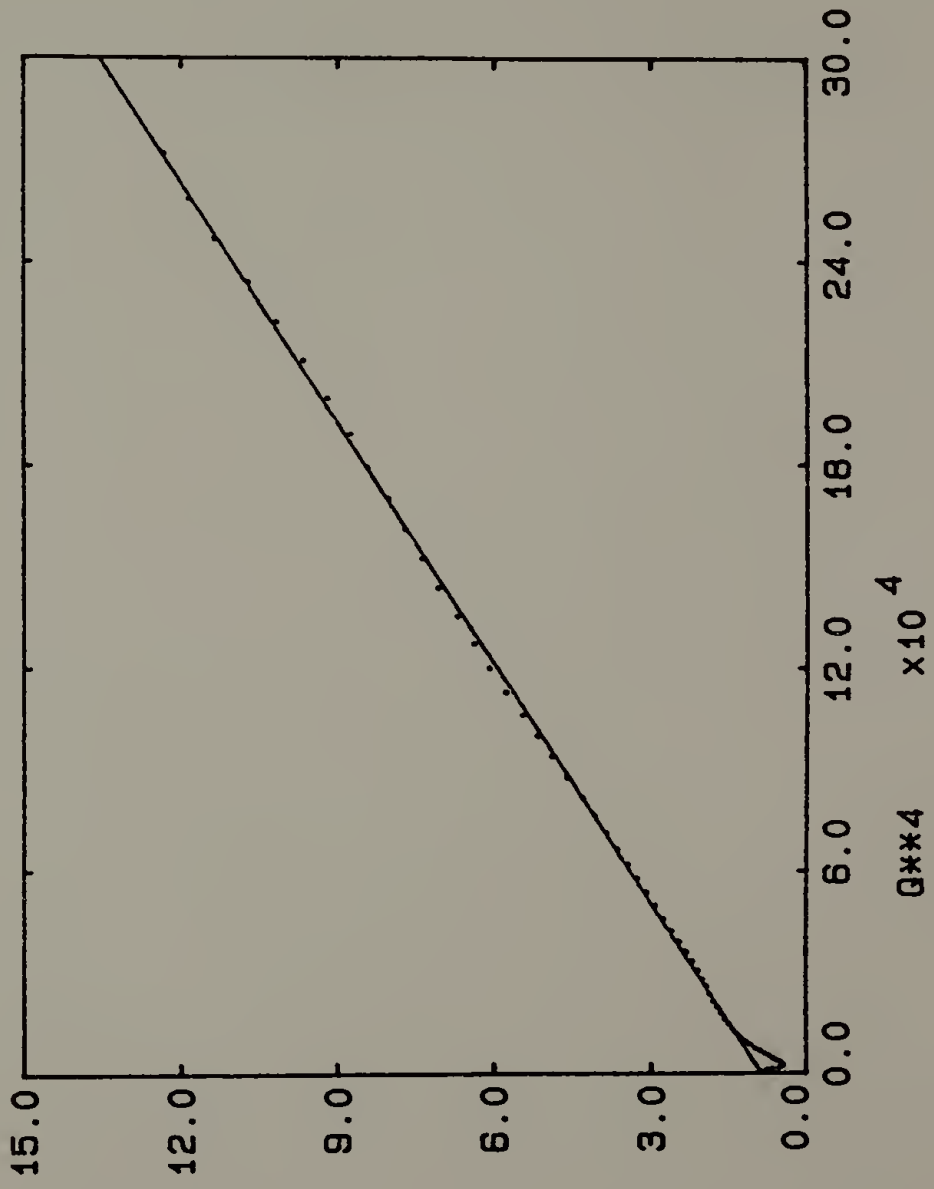
Figure 9.   Electron density profile and concentration profile for PVF$_2$/PMMA blend.

$\rho(X)$

$C_{PMMA}(X)$

X
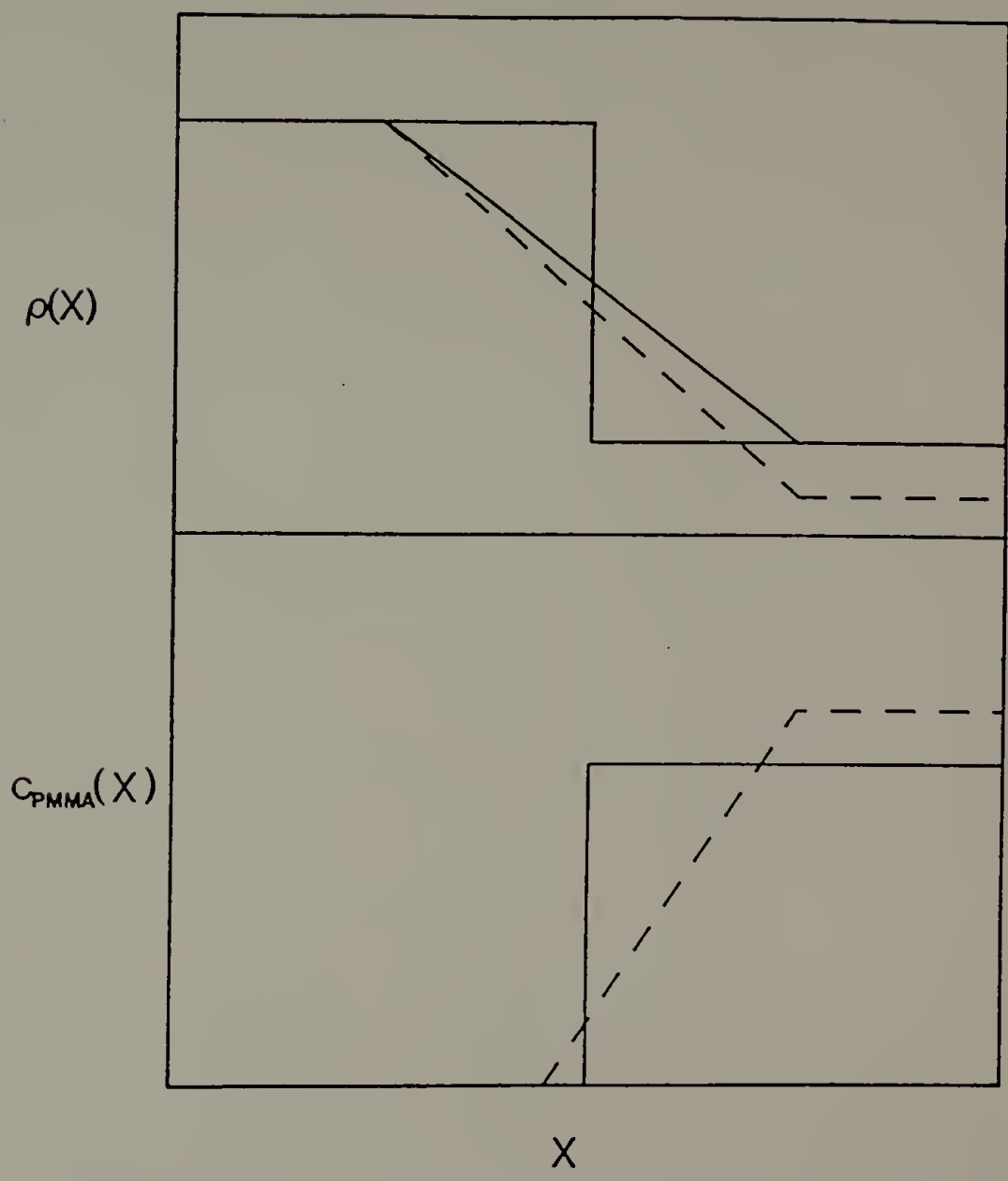
Figure 10. I vs. q SANS for pure PVF$_2$.
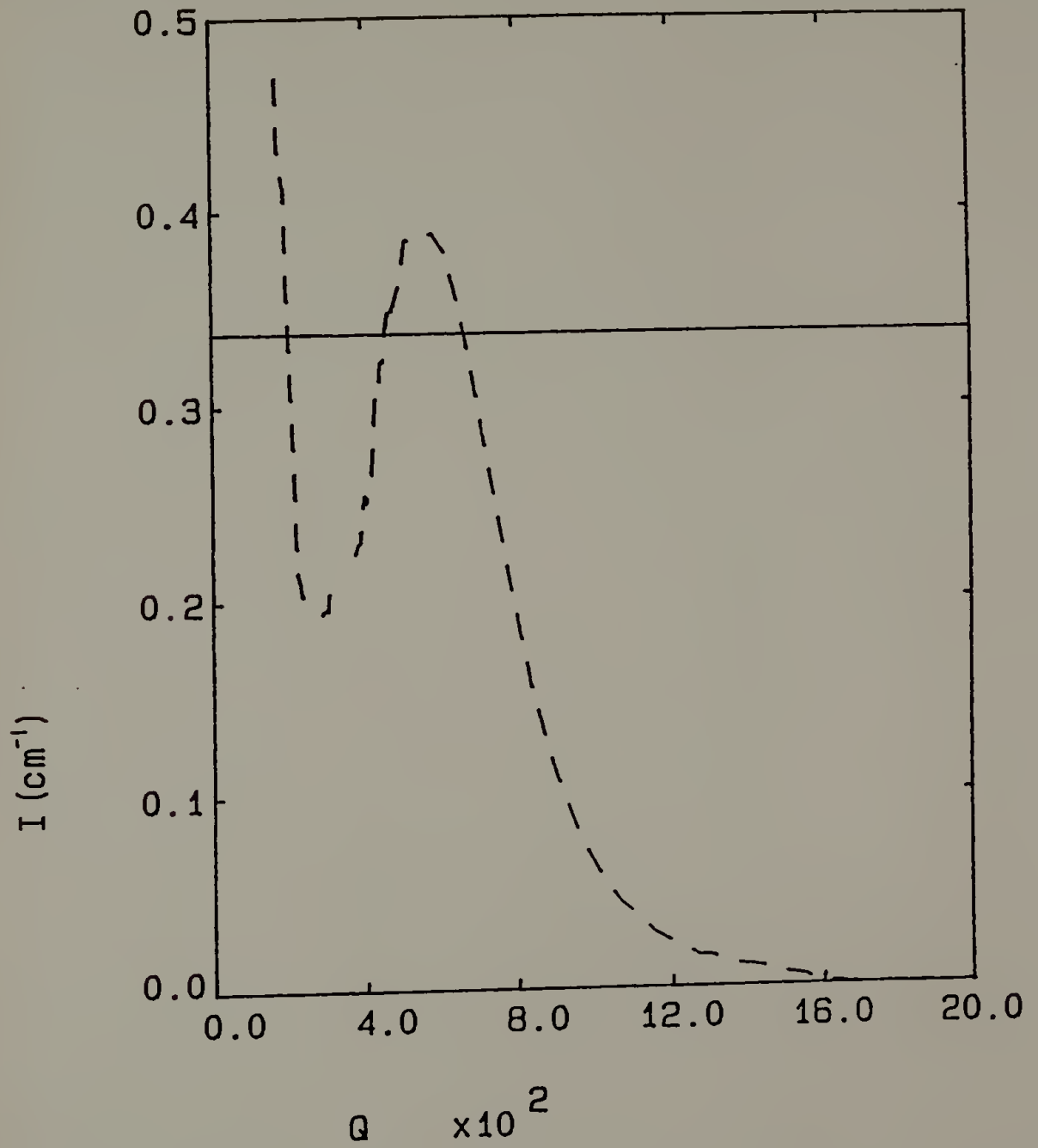
Figure 11. Calculated SANS intensities for pure iPS from SAXS results.
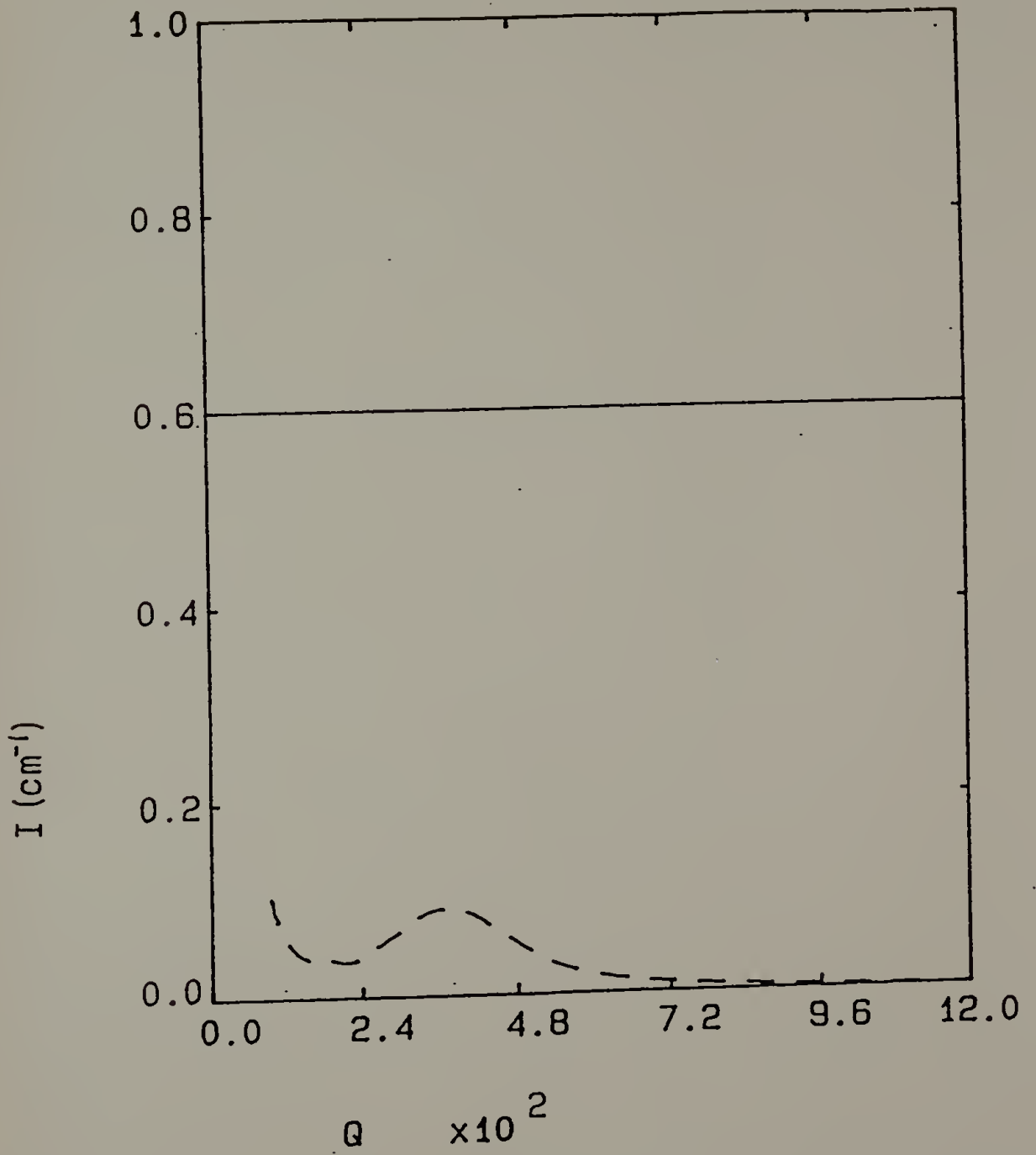
Figure 12. I vs. q SANS and desmeared SAXS intensities for 70 PVF$_2$/30 PMMA (melt cryst.) blend.
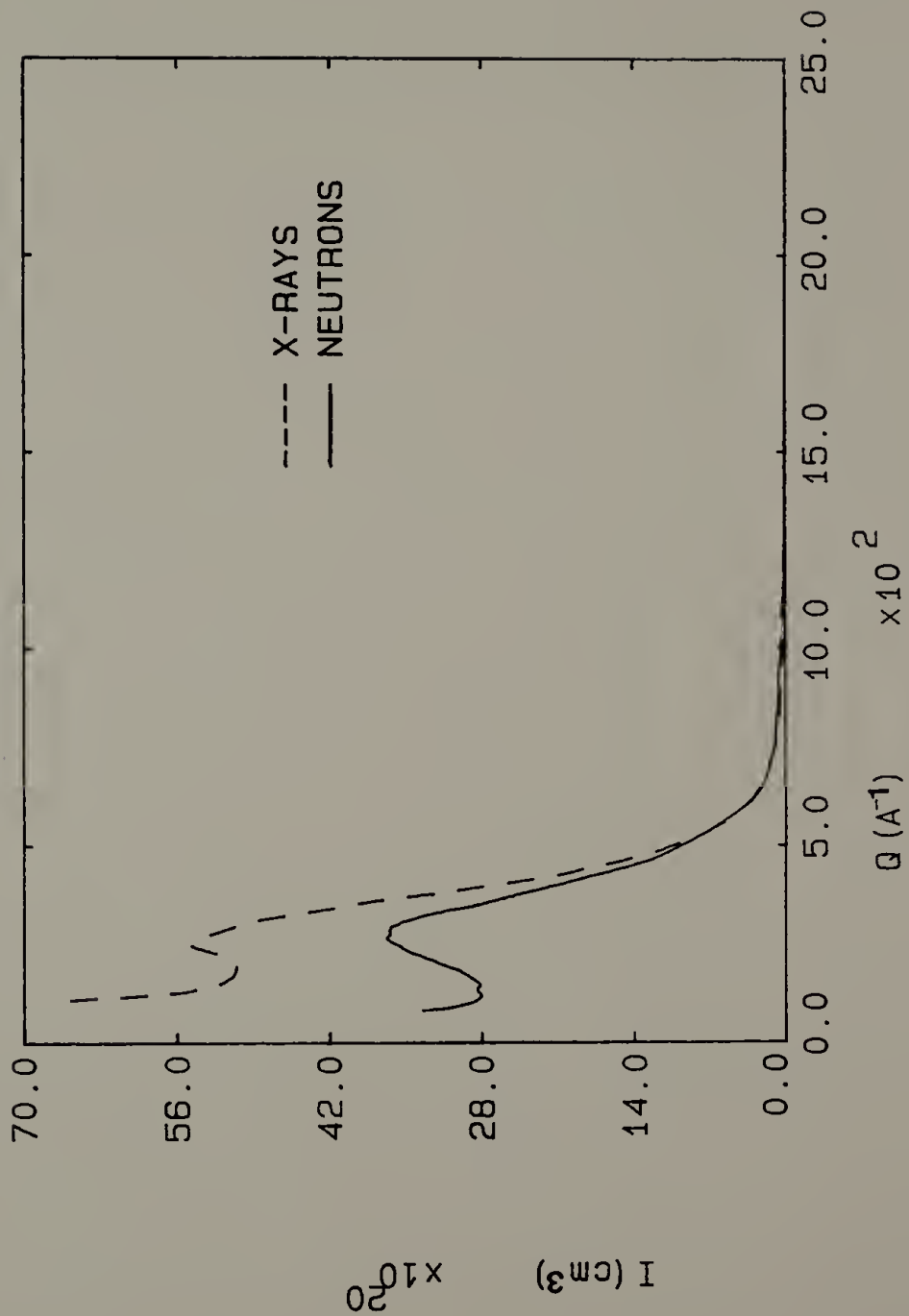
Figure 13. I vs. q SANS and desmeared SAXS intensities for 80 PVF$_2$/20 PMMA (melt cryst.) blend.
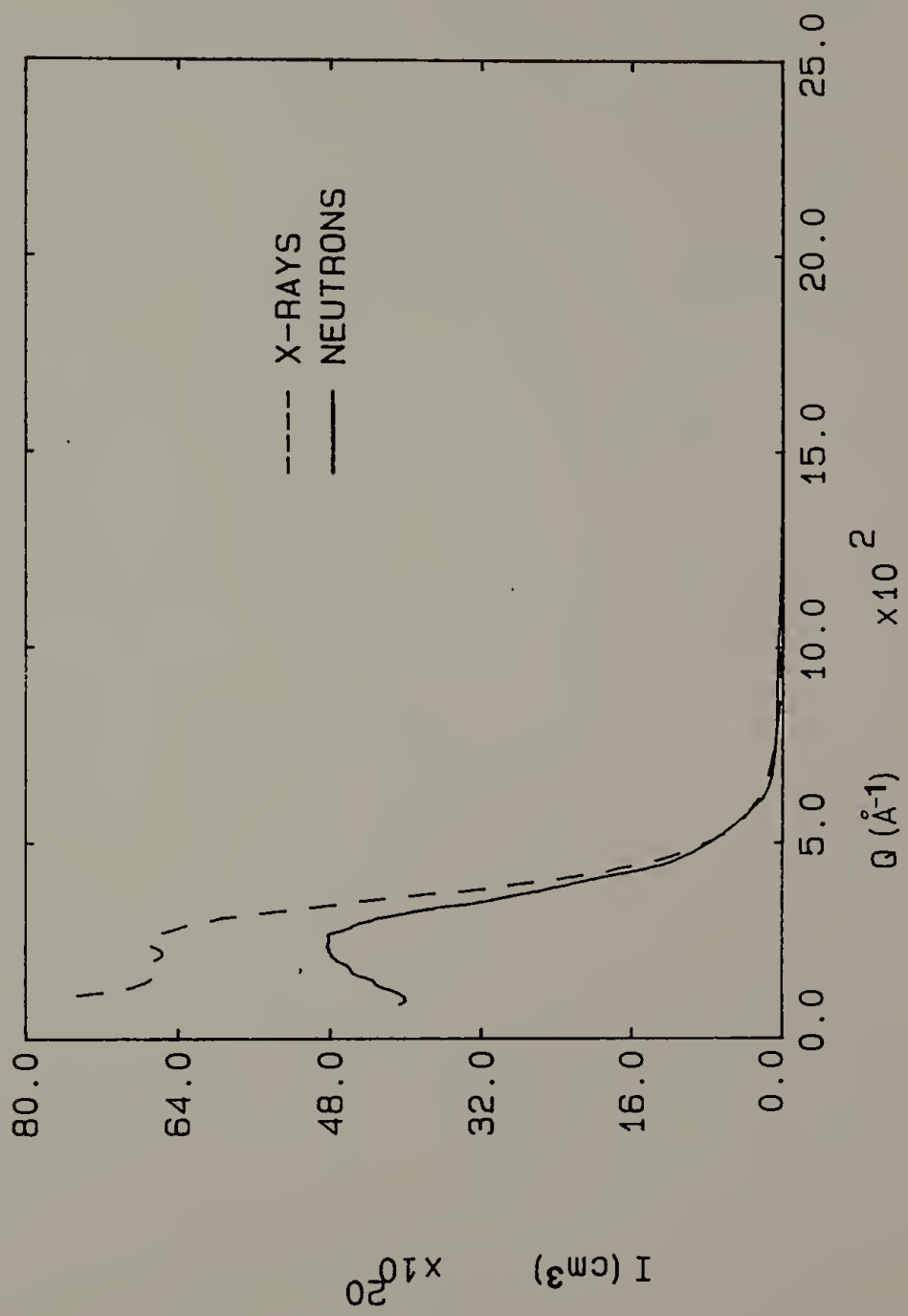
Figure 14. I vs. q SANS and desmeared SAXS intensities for 90 PVF$_2$/10 PMMA (melt cryst.) blend.
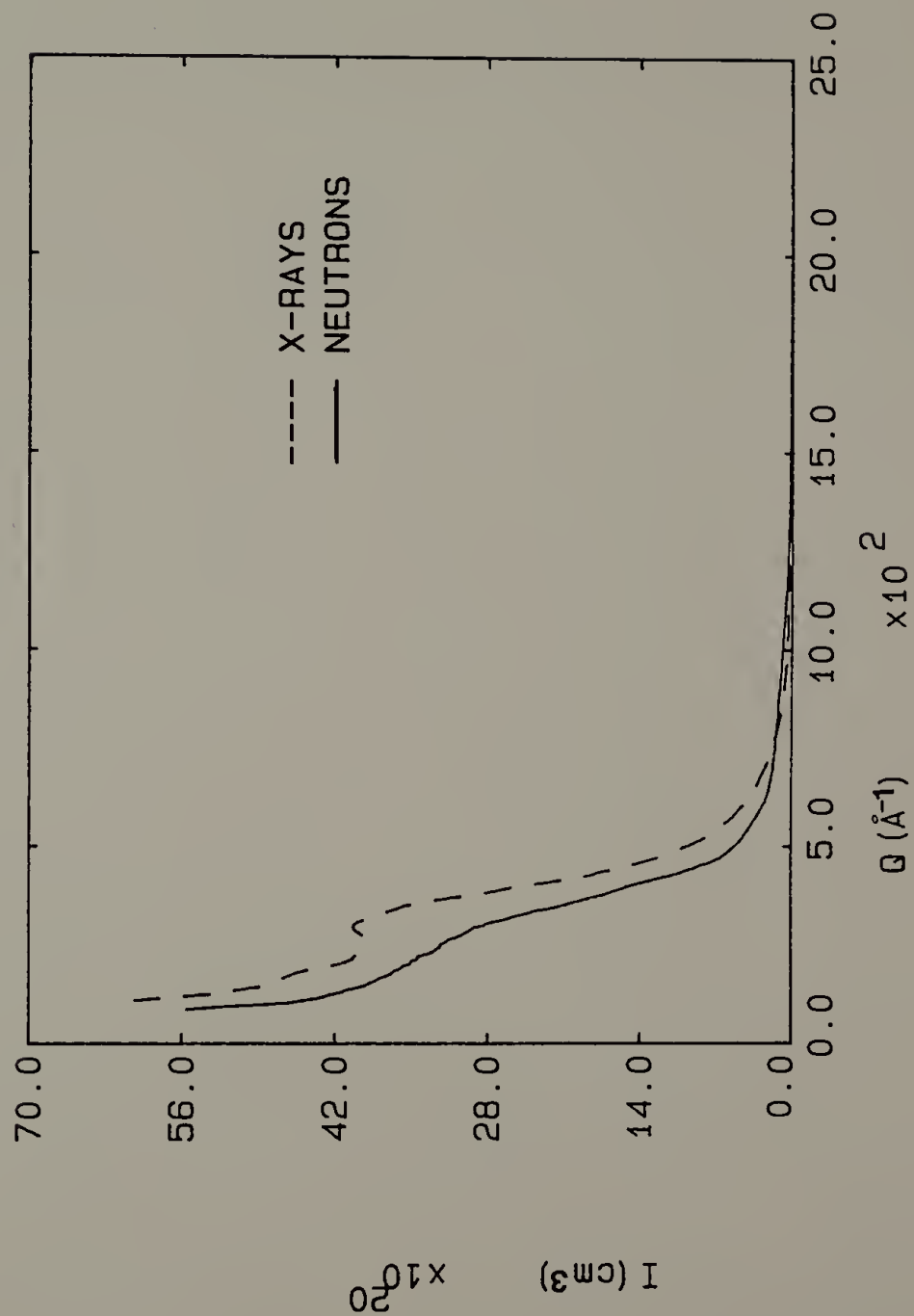
Figure 15. I vs. q SANS and desmeared SAXS intensities for 70 PVF_2/30 PMMA (melt cryst.) blend.
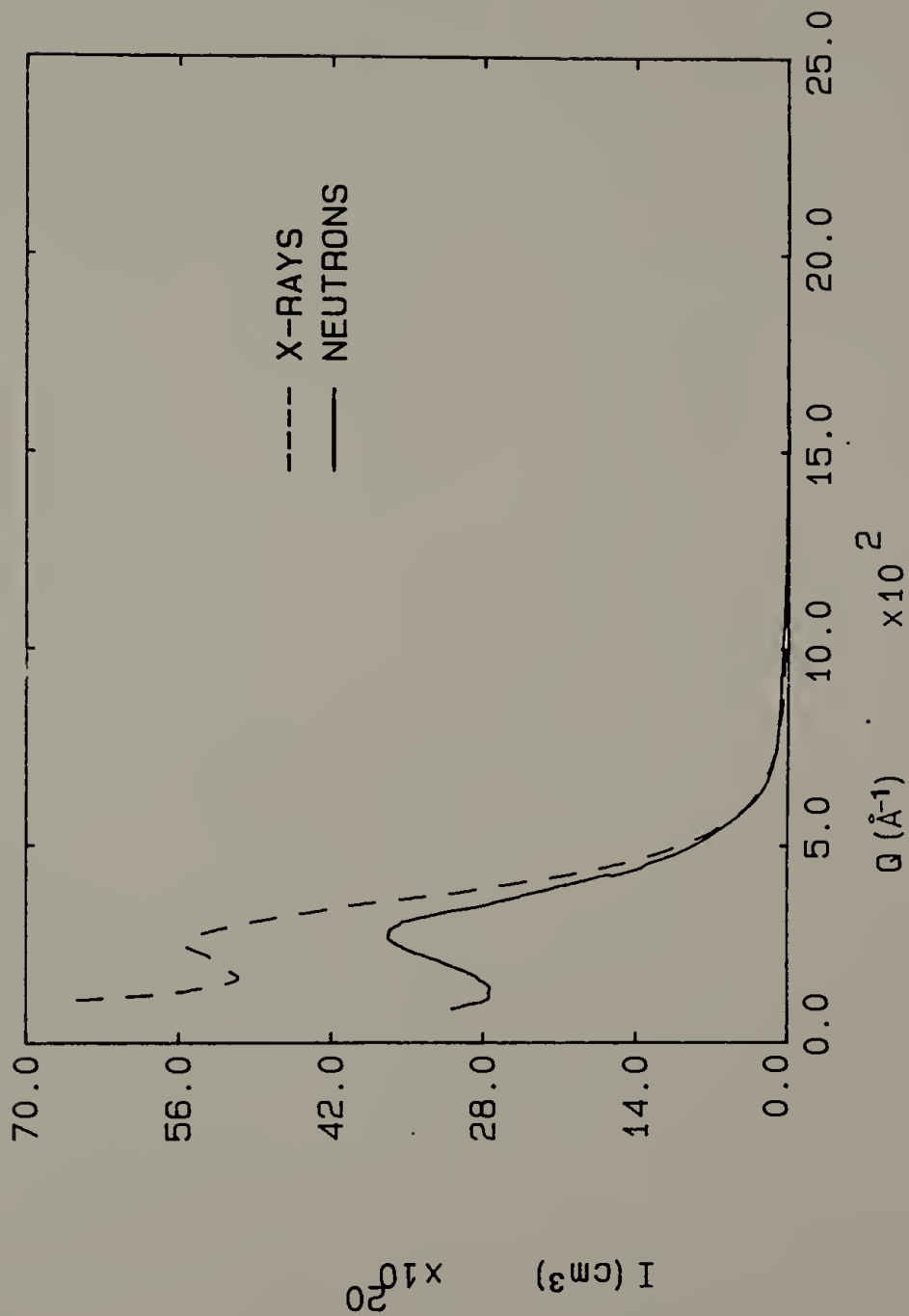
Figure 16. I vs. q SANS and desmeared SAXS intensities for 80 PVF_2/20 PMMA (melt cryst.) blend.
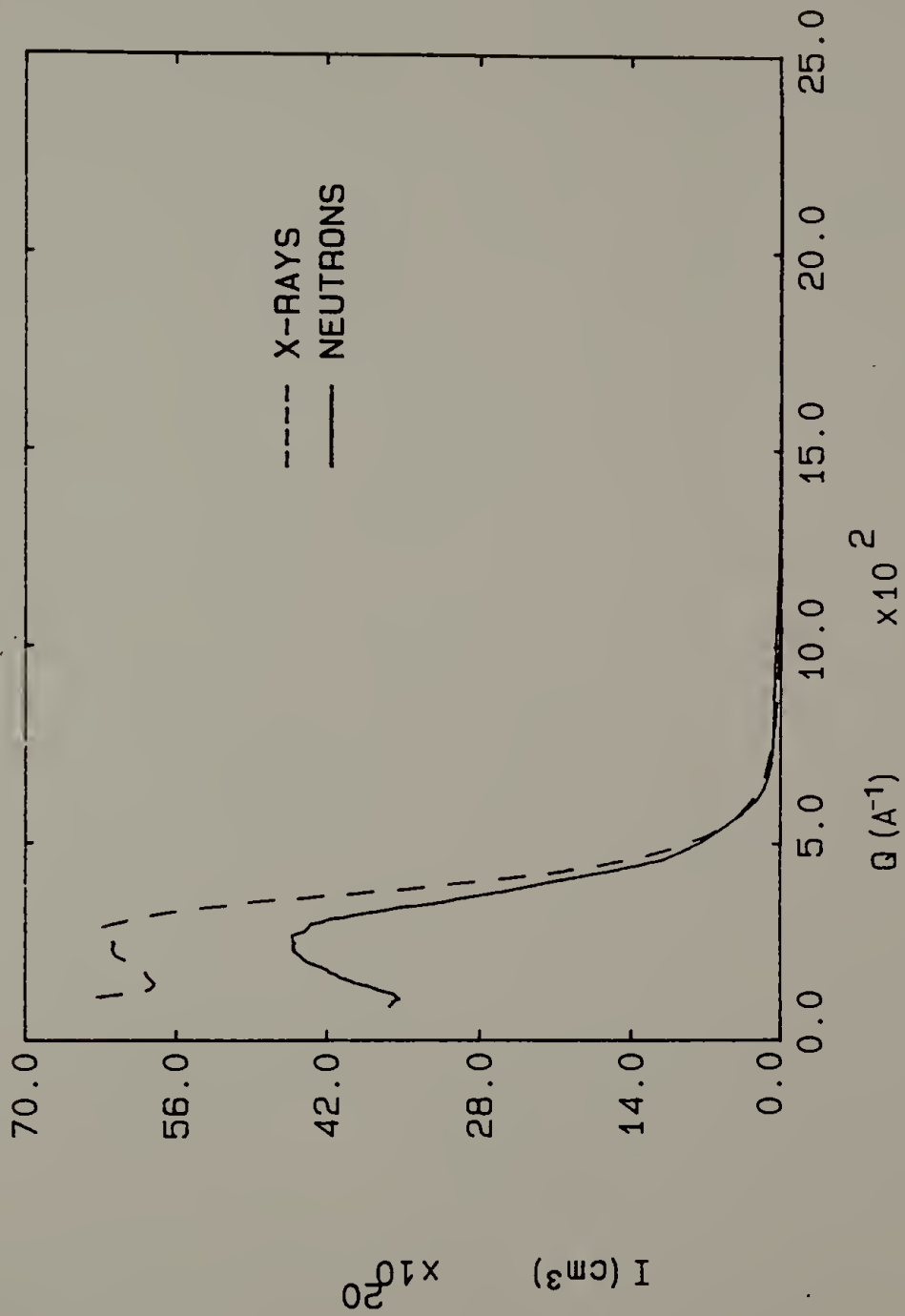
Figure 17. I vs. q SANS and desmeared SAXS intensities for 90 PVF$_2$/10 PMMA (melt cryst.) blend.
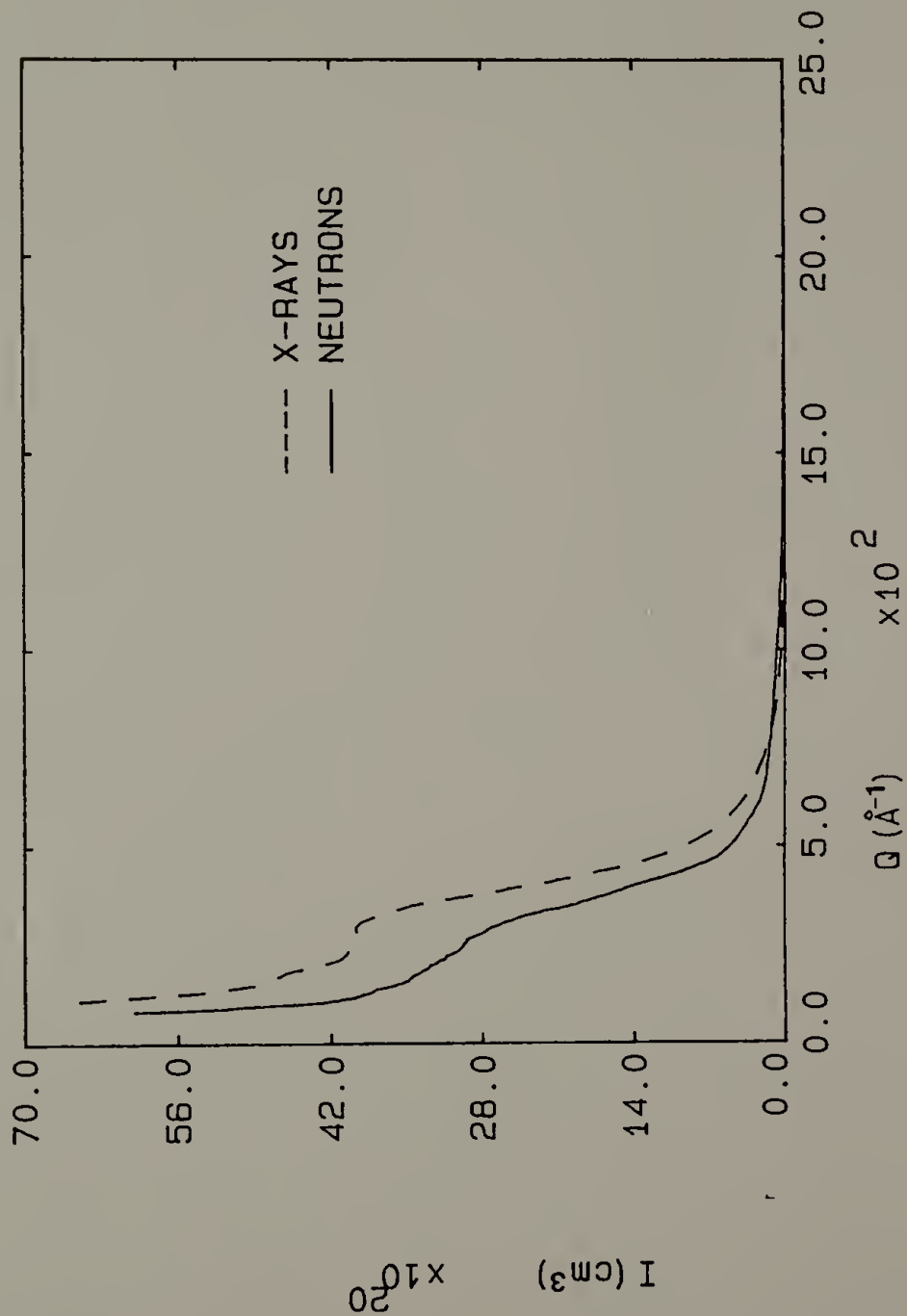
Figure 18. Iq^2 vs. q SANS and desmeared SAXS intensities for 70 PVF_2/30 PMMA (melt cryst.) blend.
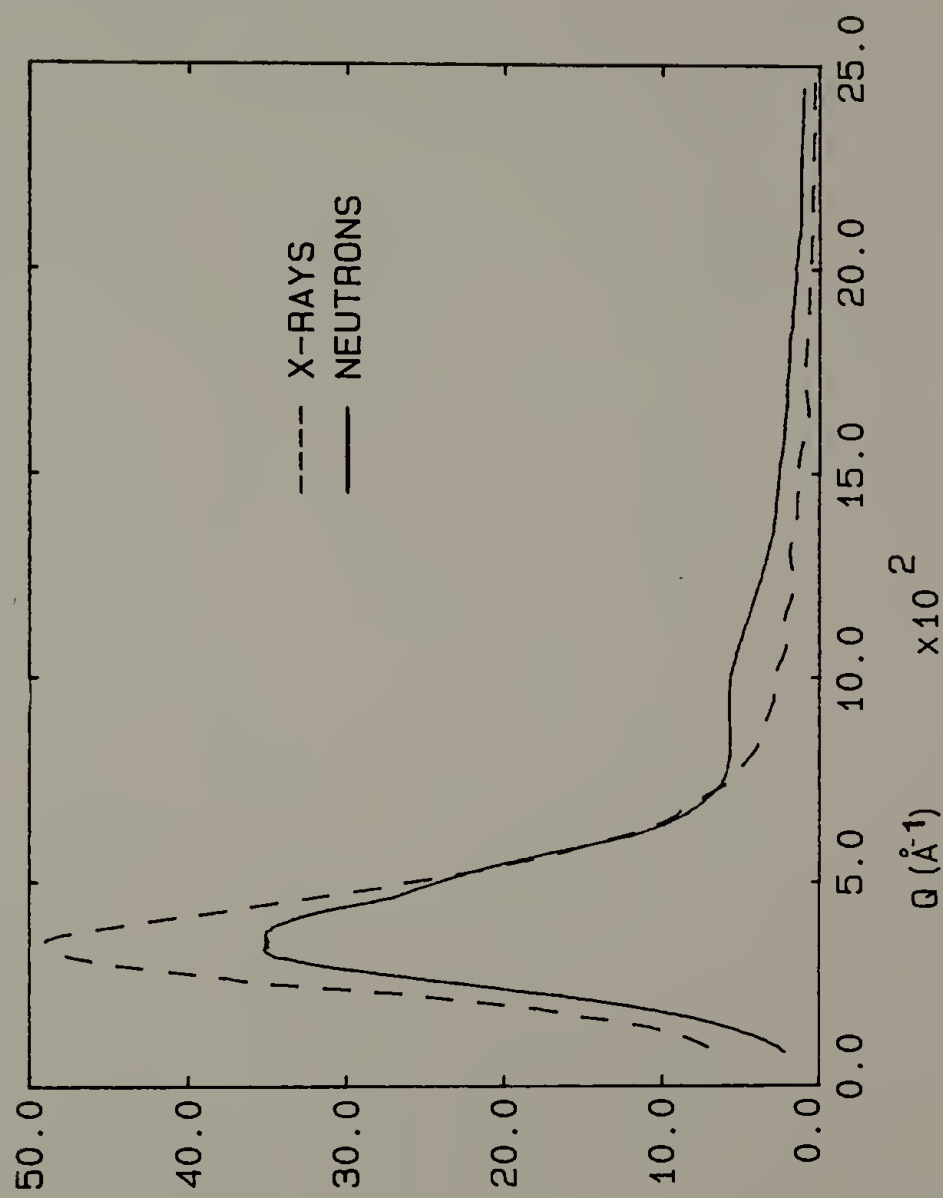
Figure 19. Iq^2 vs. q SANS and desmeared SAXS intensities for 80 PVF_2/20 PMMA (melt cryst.) blend.
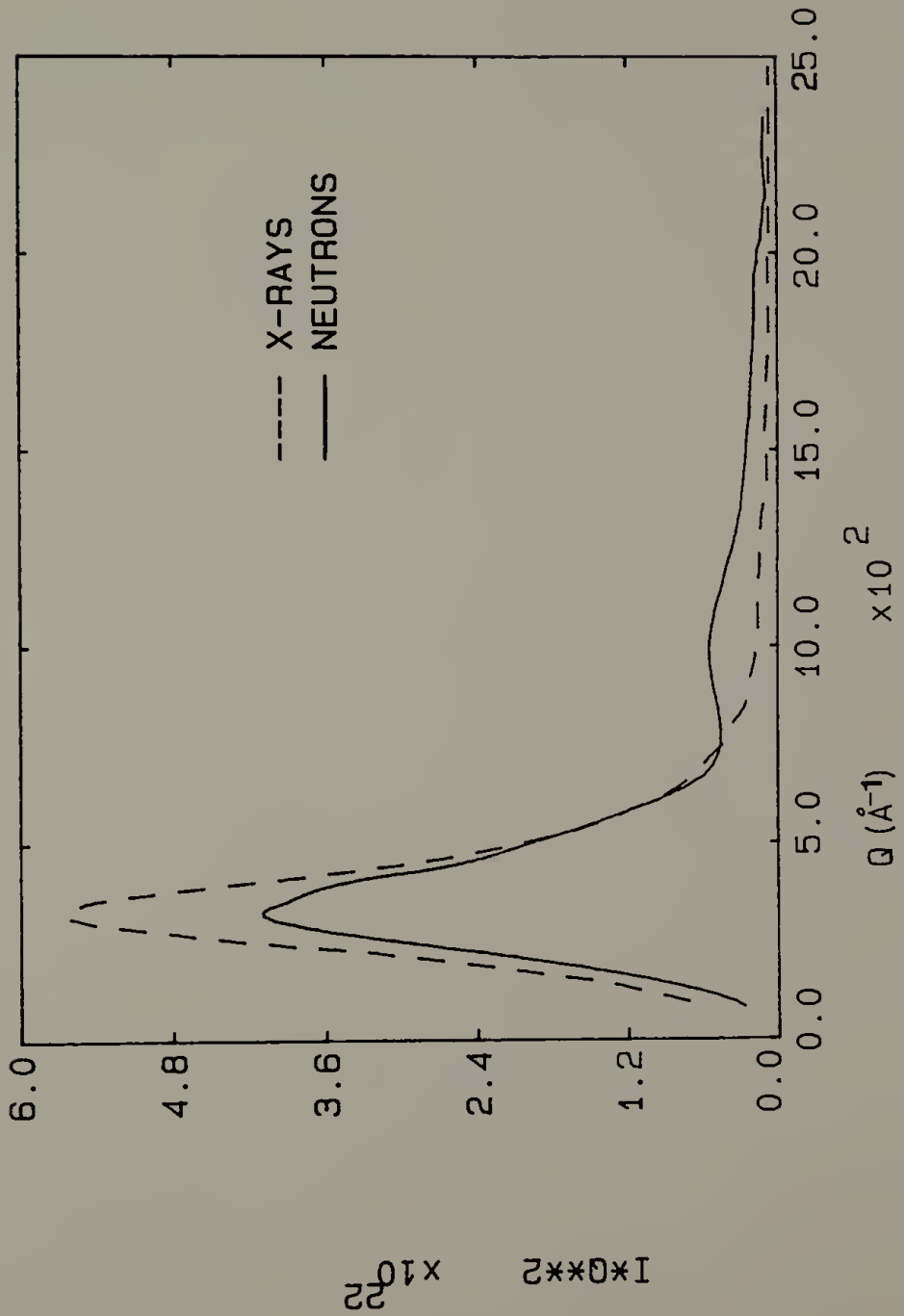
Figure 20. Iq^2 vs. q SANS and desmeared SAXS intensities for 90 PVF_2/10 PMMA (melt cryst.) blend.
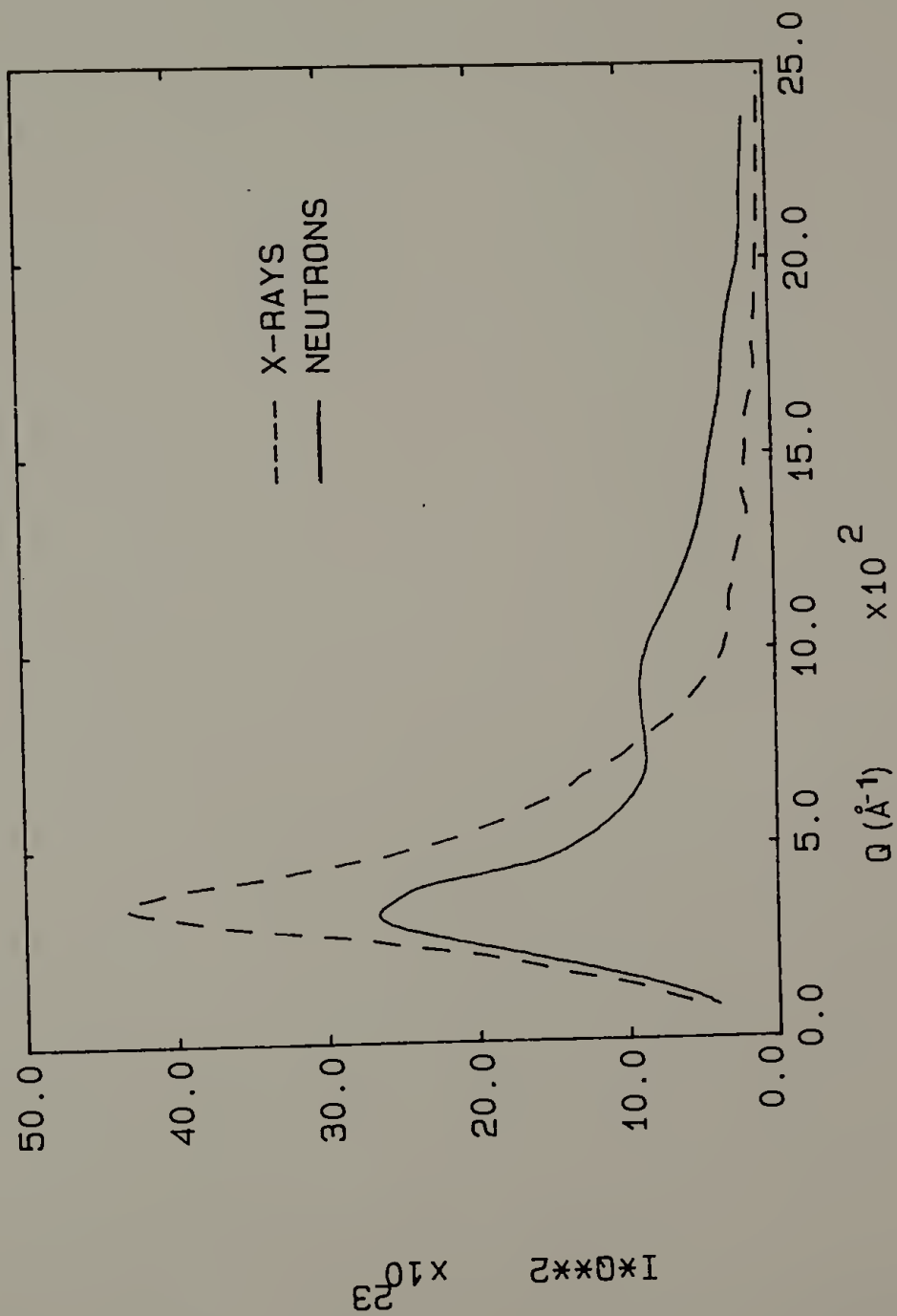
Figure 21. Iq^2 vs. q SANS and desmeared SAXS intensities for 70 PVF$_2$/30 PMMA (melt cryst.) blend.
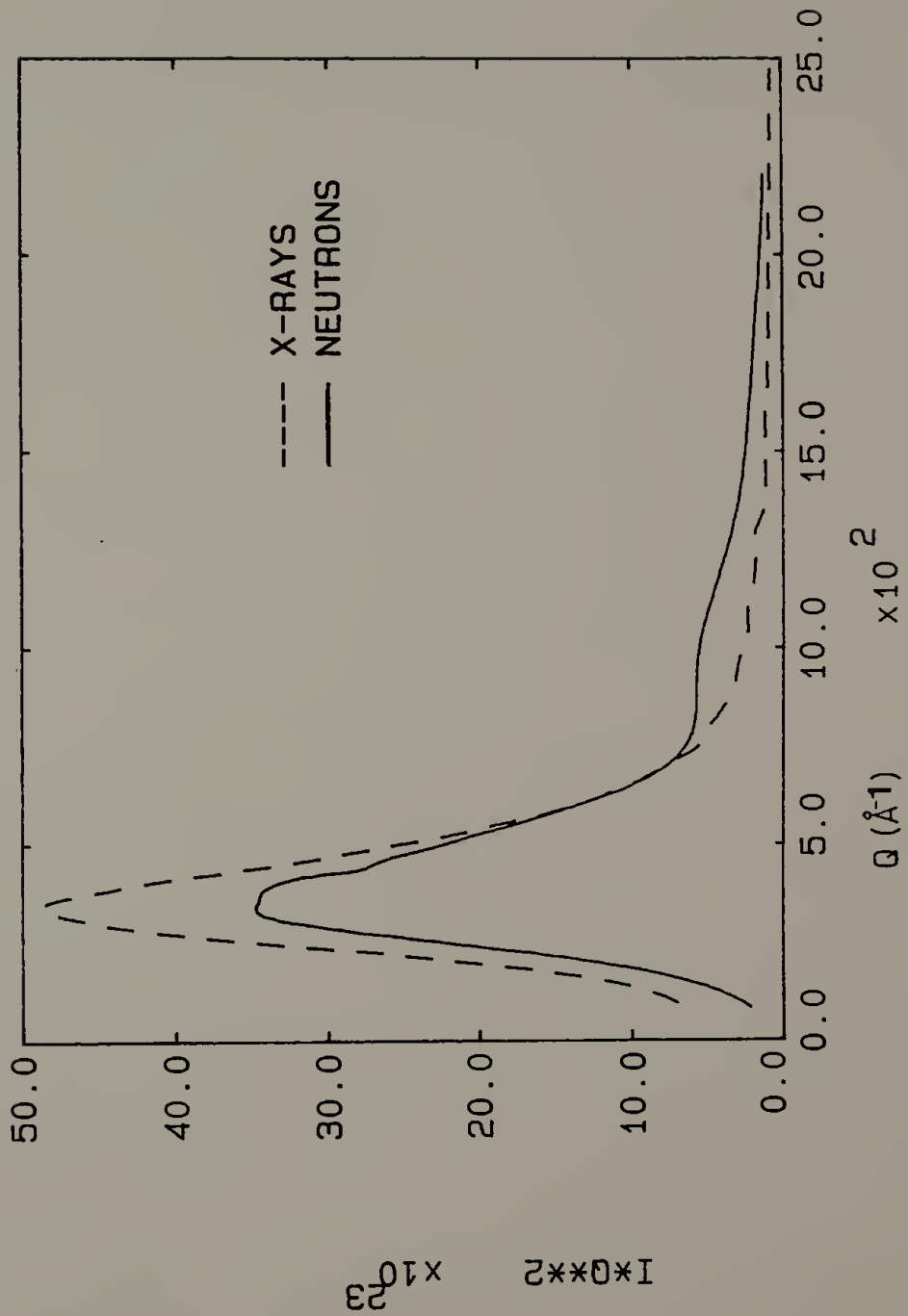
Figure 22. Iq^2 vs. q SANS and desmeared SAXS intensities for 80 PVF$_2$/20 PMMA quenched blend.
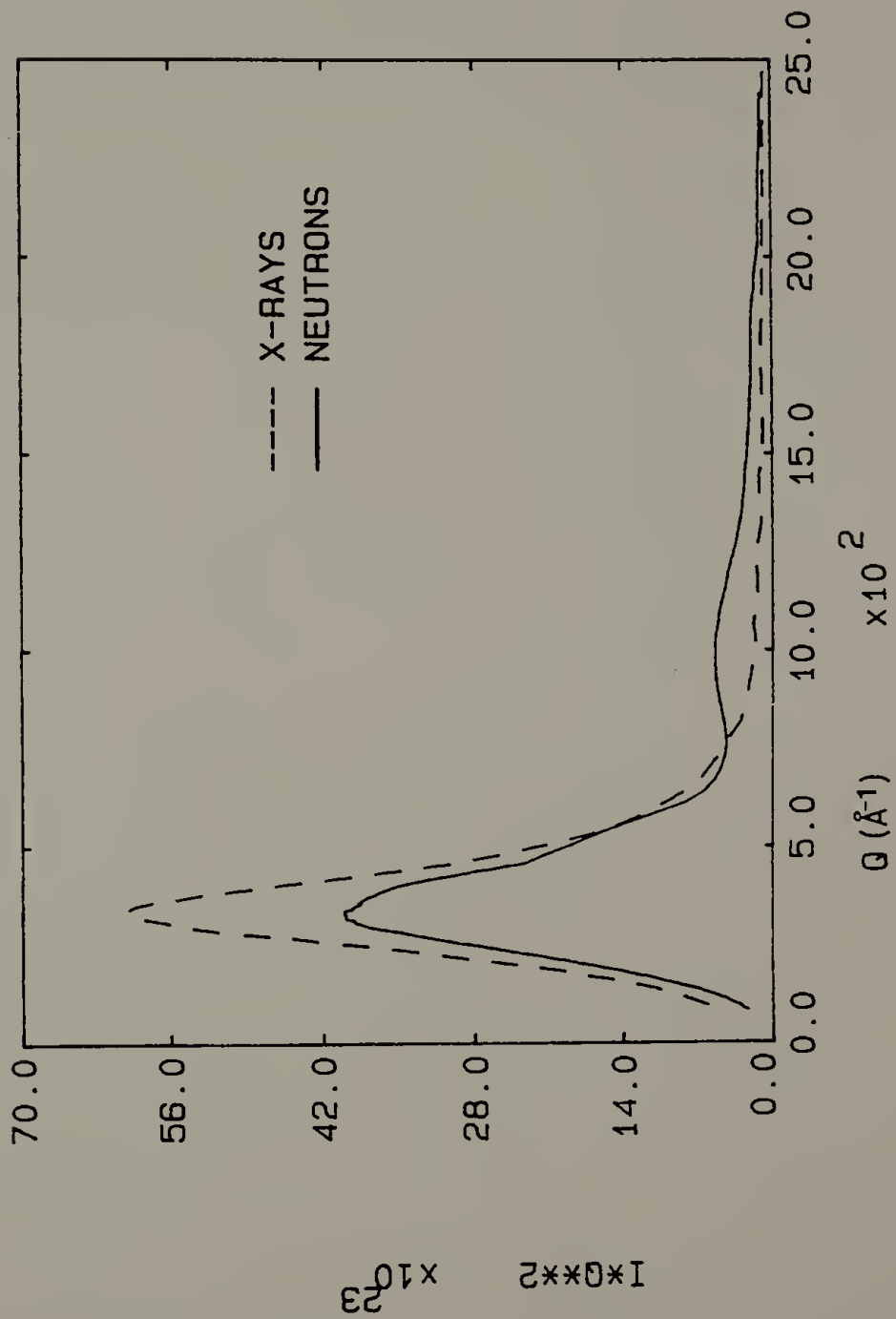
Figure 23. Iq^2 vs. q SANS and desmeared SAXS intensities for 90 PVF_2/10 PMMA quenched blend.
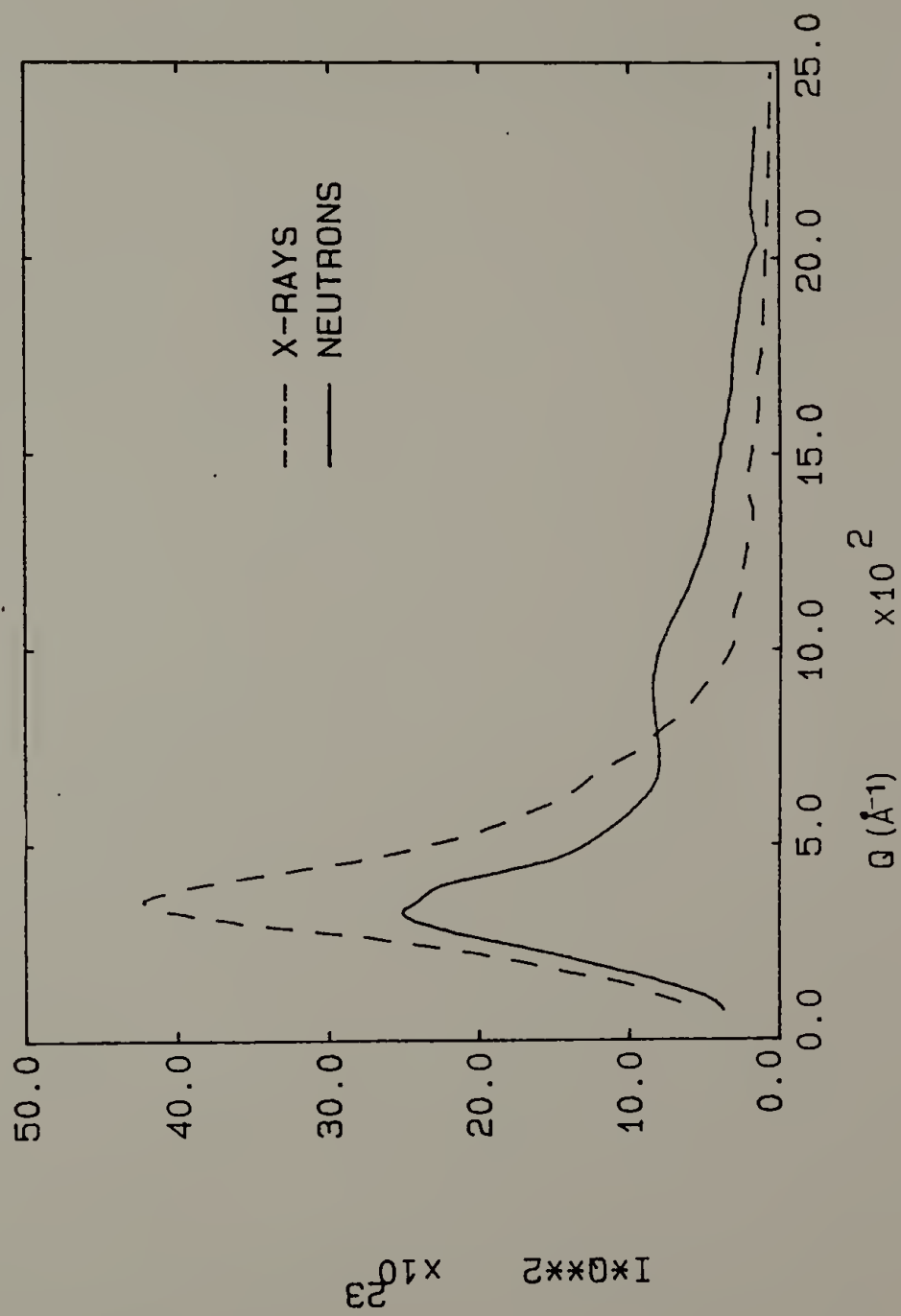
Figure 24. One-dimensional correlation function from SANS and SAXS intensities for 70 PVF$_2$/30 PMMA (melt cryst.) blend.
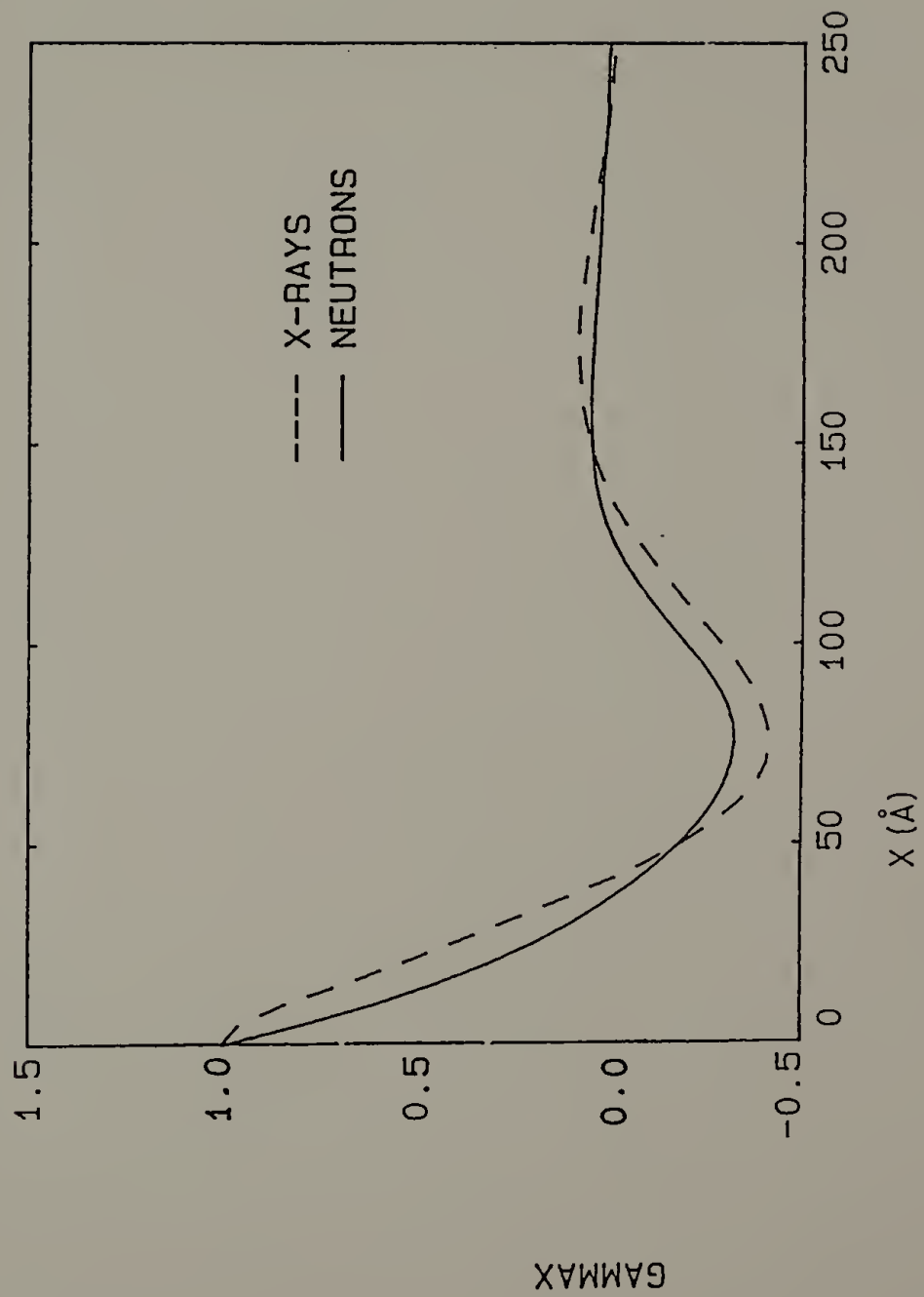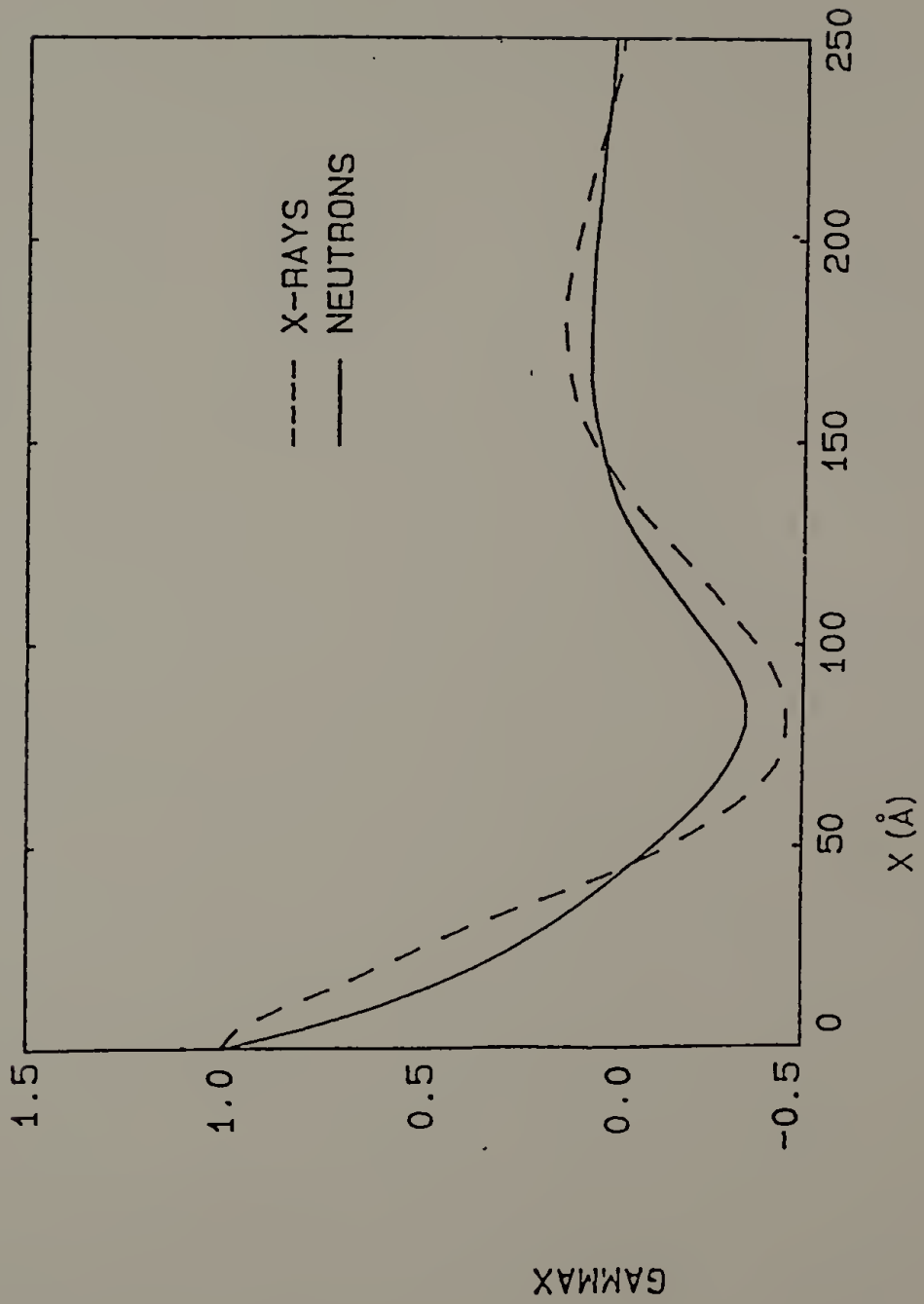
Figure 25. One-dimensional correlation function from SANS and SAXS intensities for 80 PVF_2/20 PMMA (melt cryst.) blend.
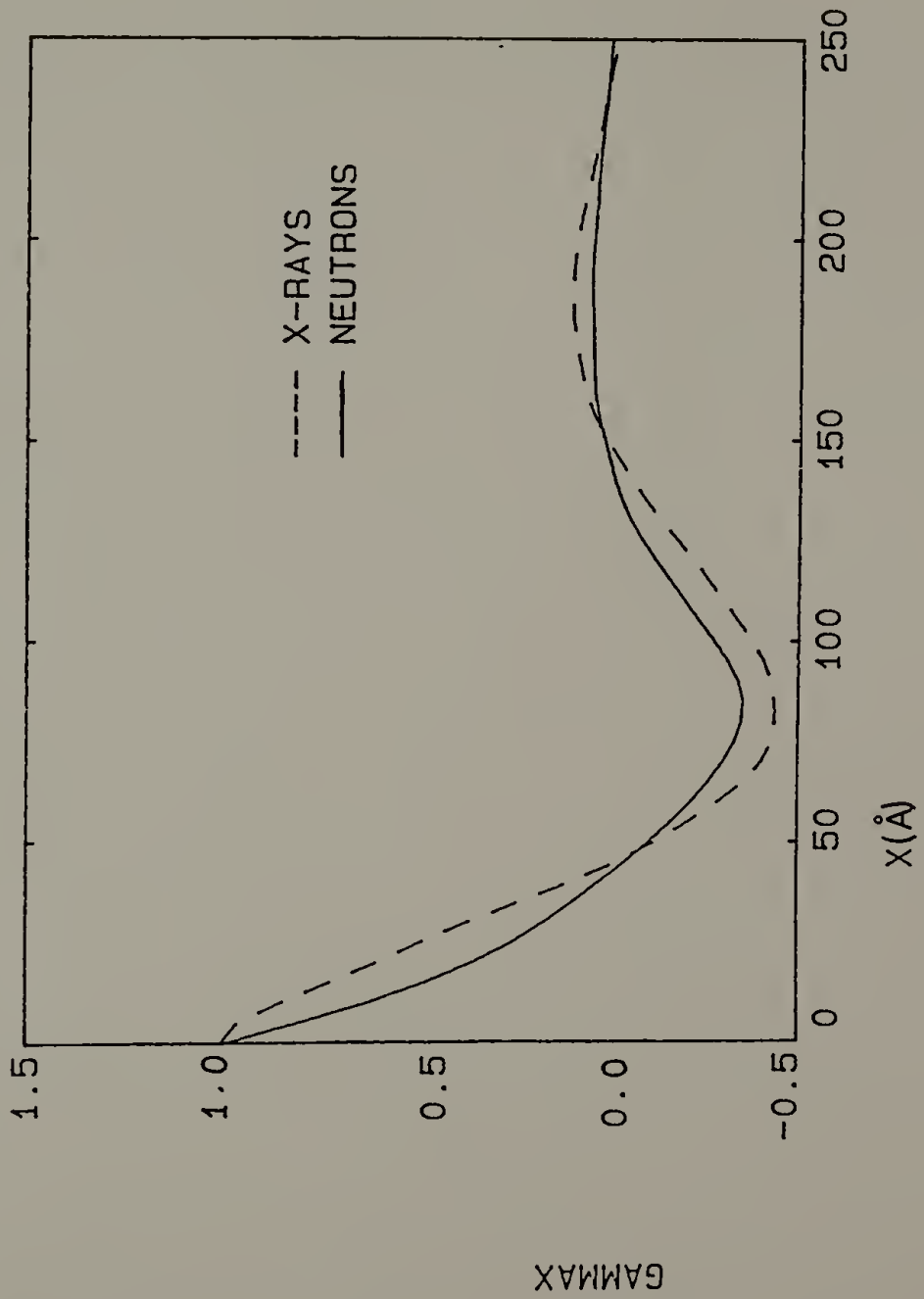
Figure 26. One-dimensional correlation function from SANS and SAXS intensities for 90 PVF$_2$/10 PMMA (melt cryst.) blend.
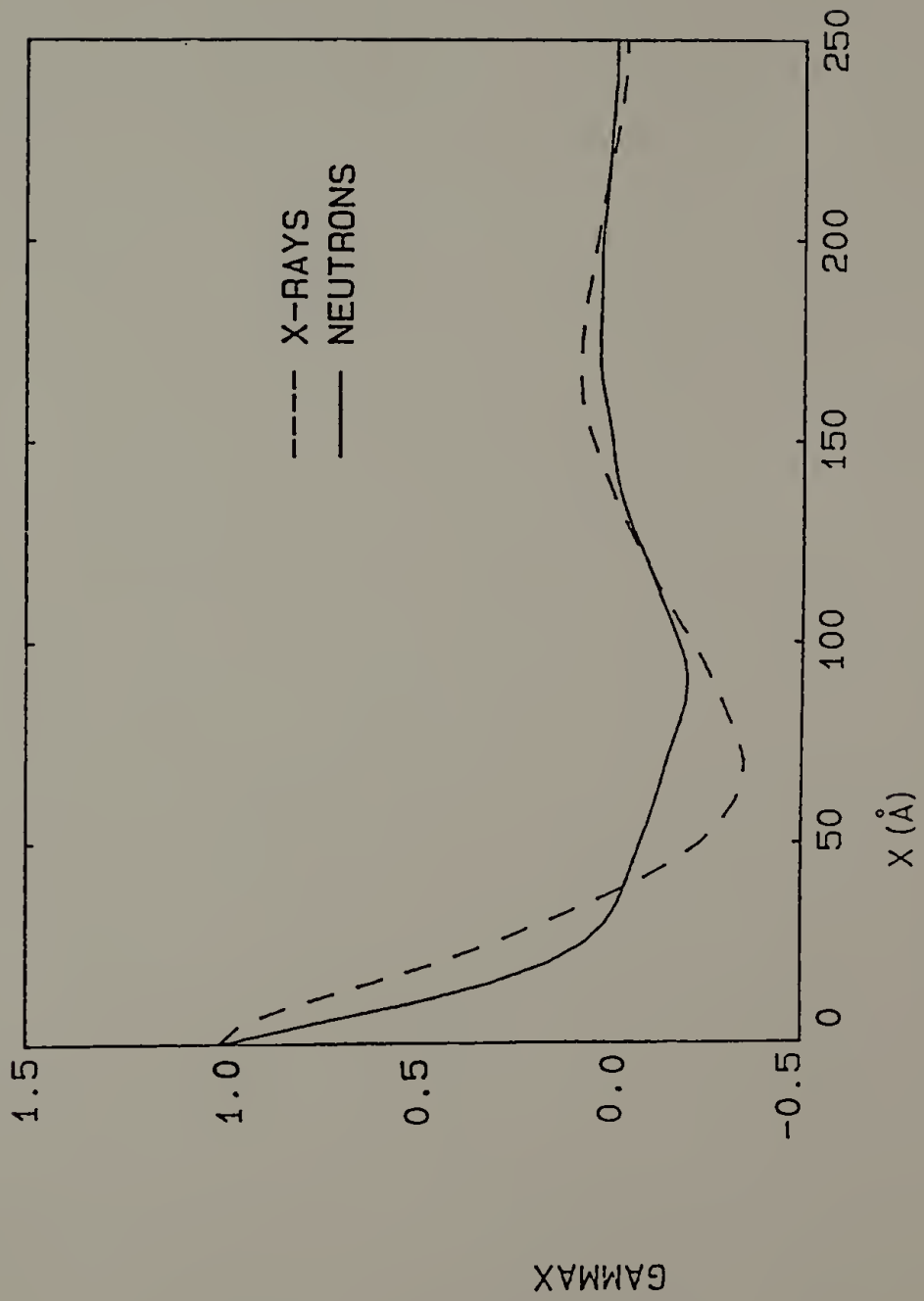
Figure 27. One-dimensional correlation function from SANS and SAXS intensities for 70 PVF_2/30 PMMA (quenched) blend.
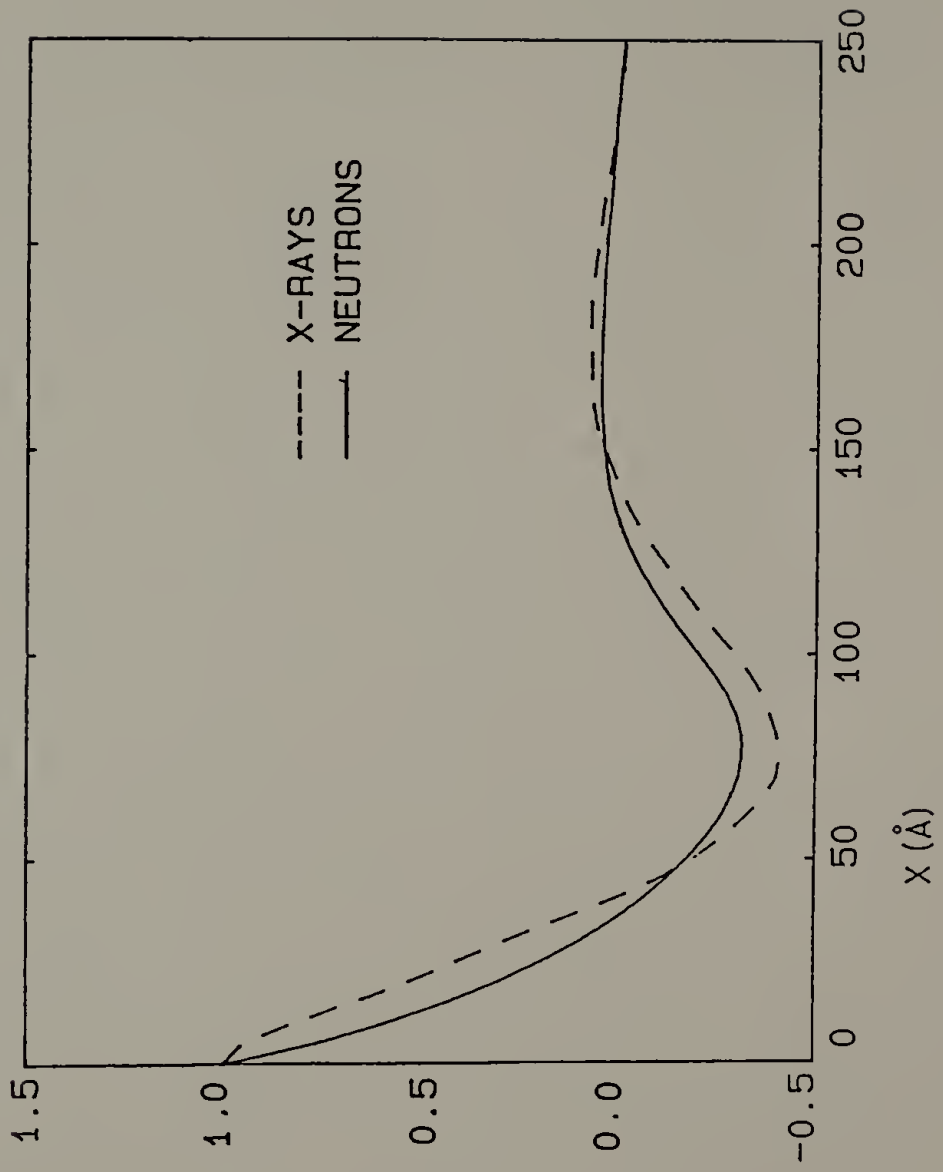
Figure 28. One-dimensional correlation function from SANS and SAXS intensities for 80 PVF$_2$/20 PMMA (quenched) blend.
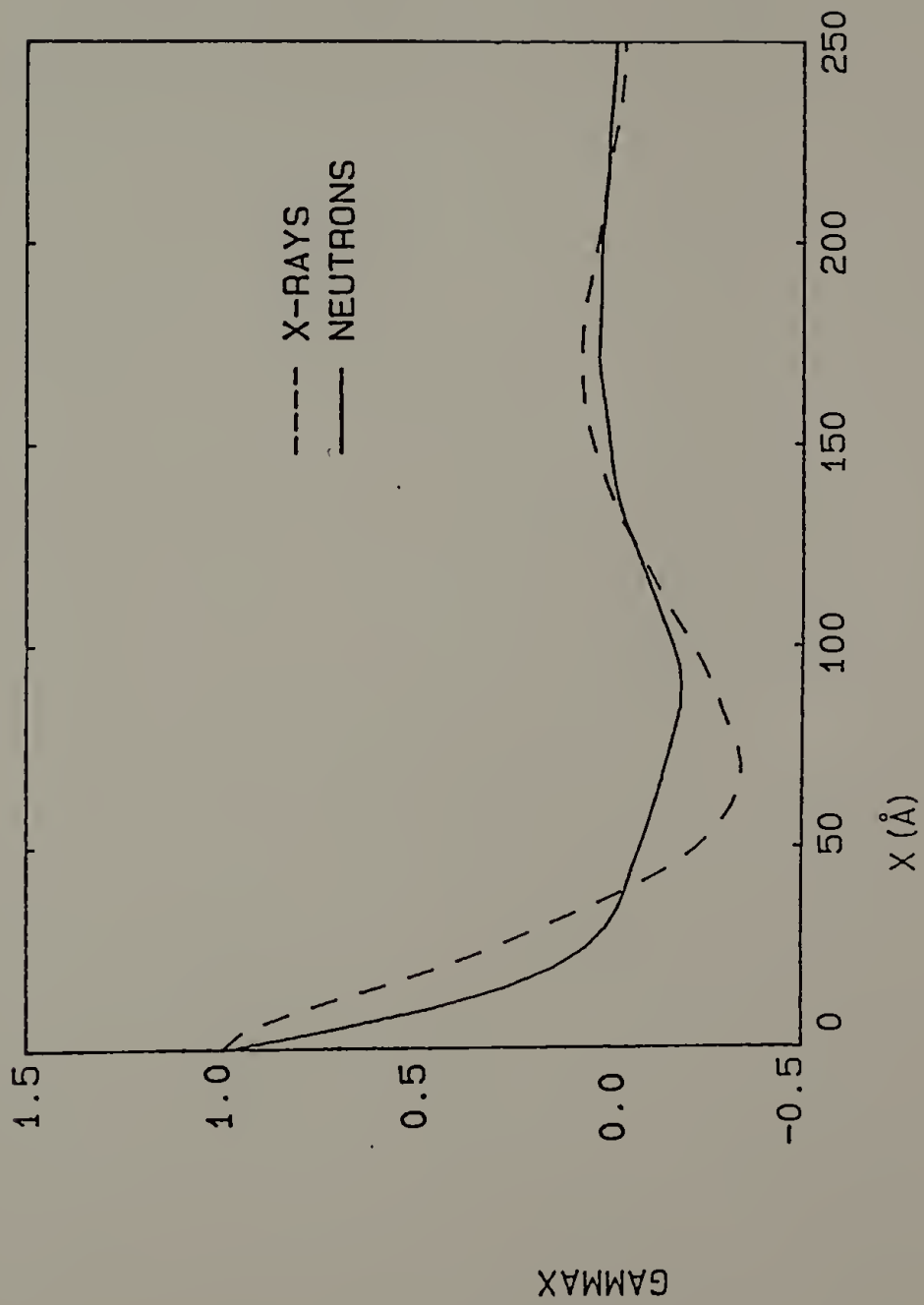
Figure 29. One-dimensional correlation function from SANS and SAXS intensities for 90 PVF_2/70 PMMA (quenched) blend.

GAMMAX

X (Å)

X-RAYS

NEUTRONS

119

Figure 30. Iq vs. q-2 SAXS intensities in the Porod region
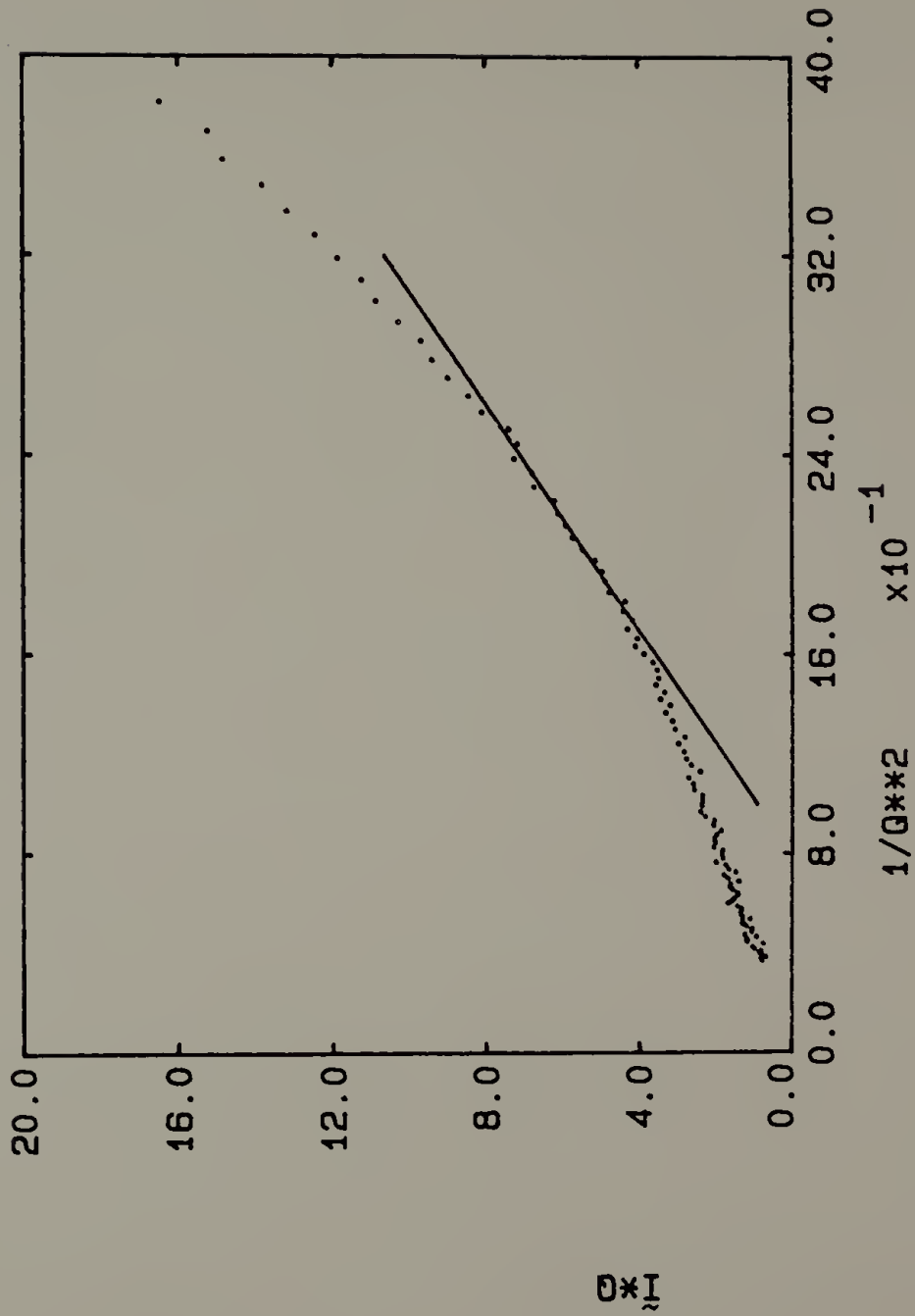
Figure 31. Iq vs. q^{-2} SAXS intensities in the Porod region for 80 PVF$_2$/20 PMMA (melt cryst.) blend.
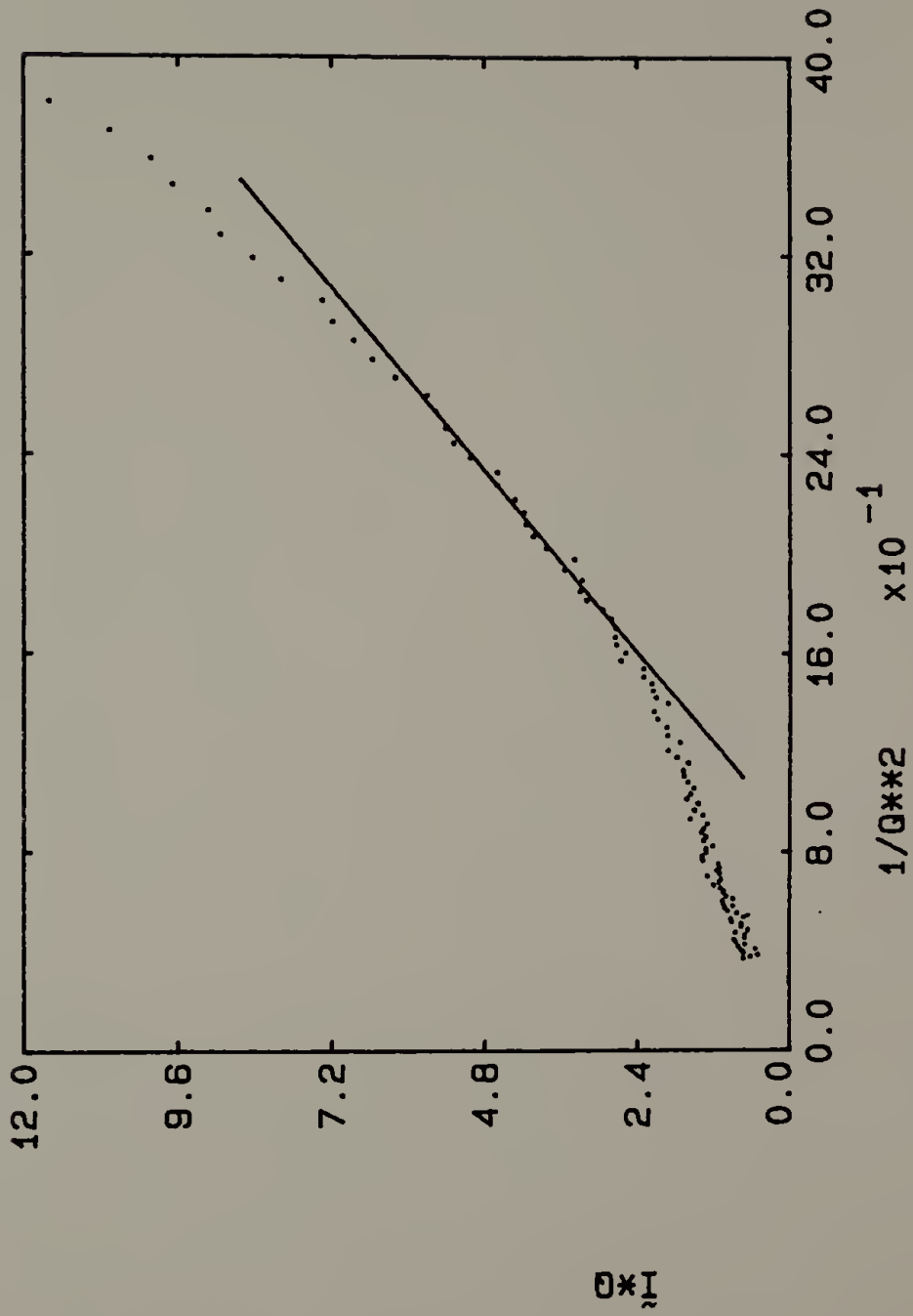
Figure 32. Iq vs. q^{-2} SAXS intensities in the Porod region for 90 PVF_2/10 PMMA (melt cryst.) blend.
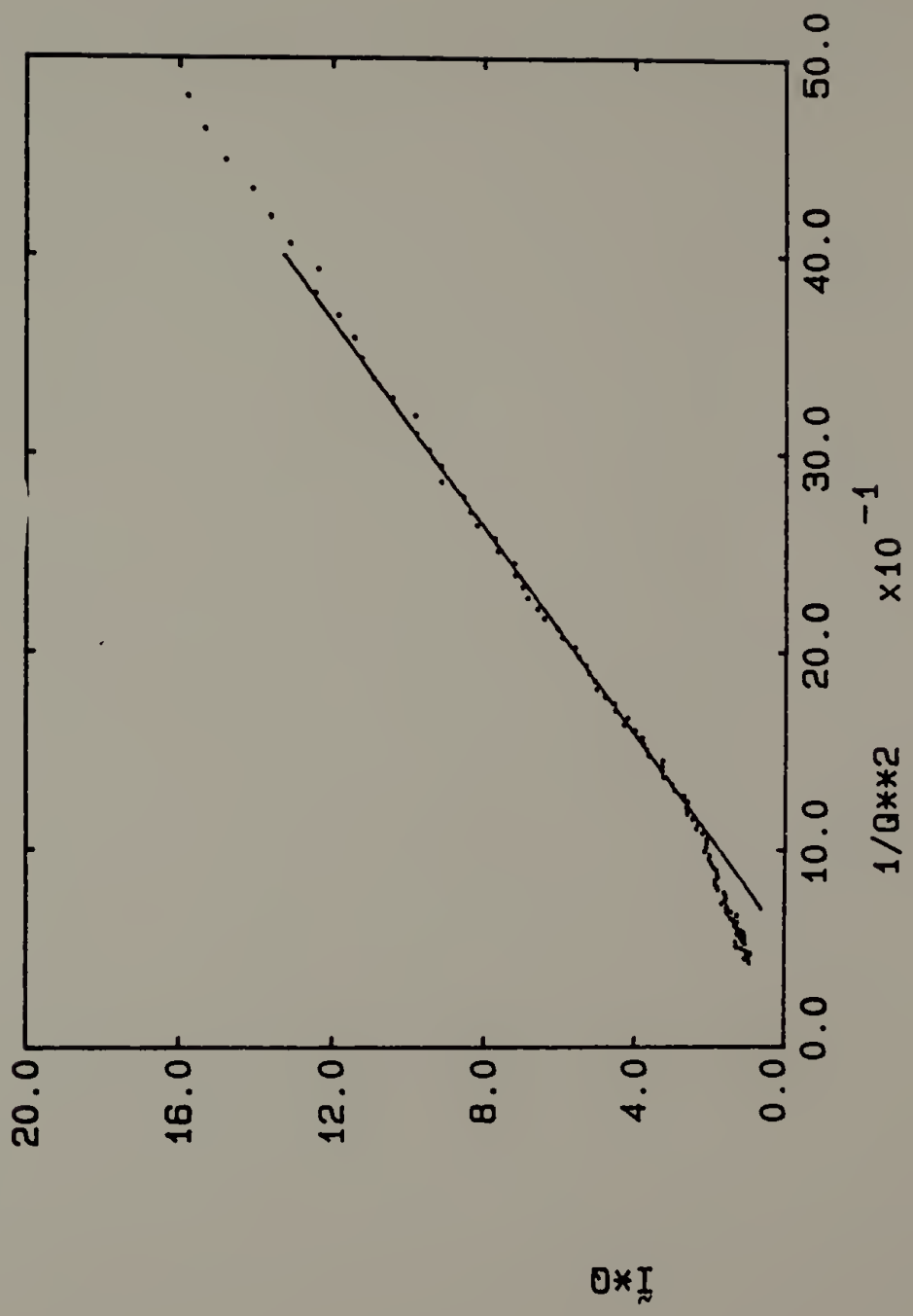
Figure 33. Iq vs. q^{-2} SAXS intensities in the Porod region for 70 PVF_2/30 PMMA quenched blend.
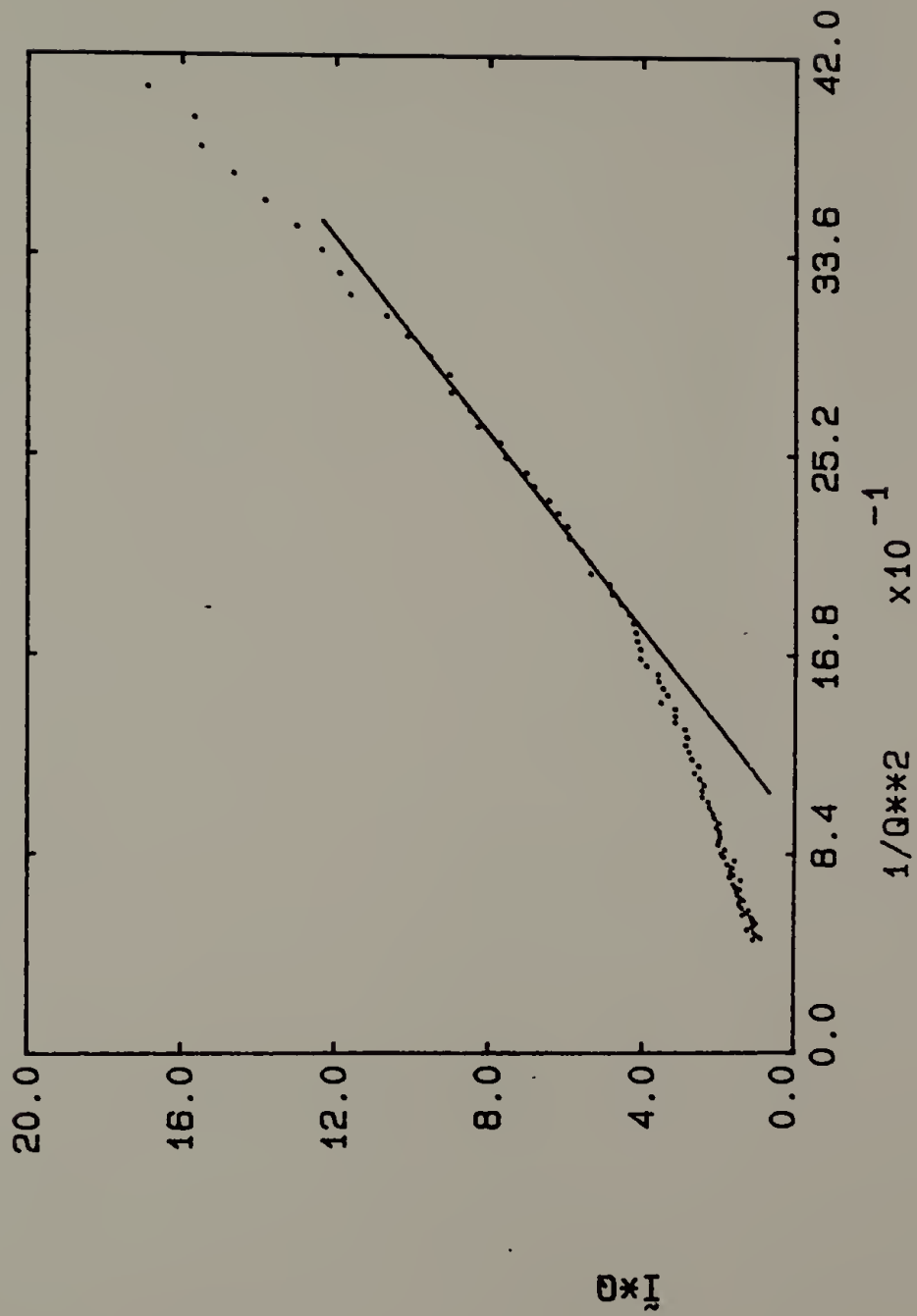
Figure 34. Iq vs. q^{-2} SAXS intensities in the Porod region for 80 PVF_2/20 PMMA quenched blend.
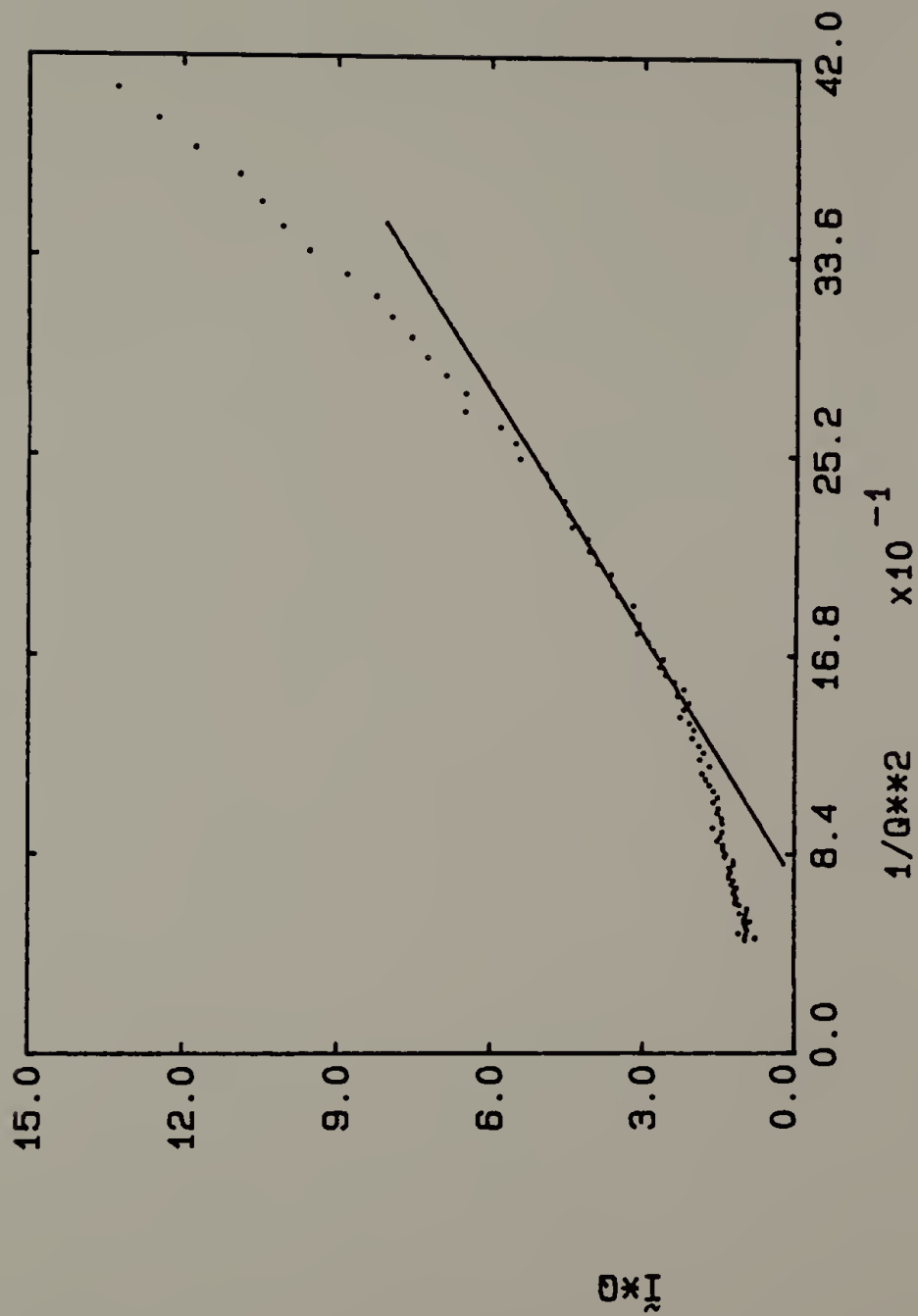
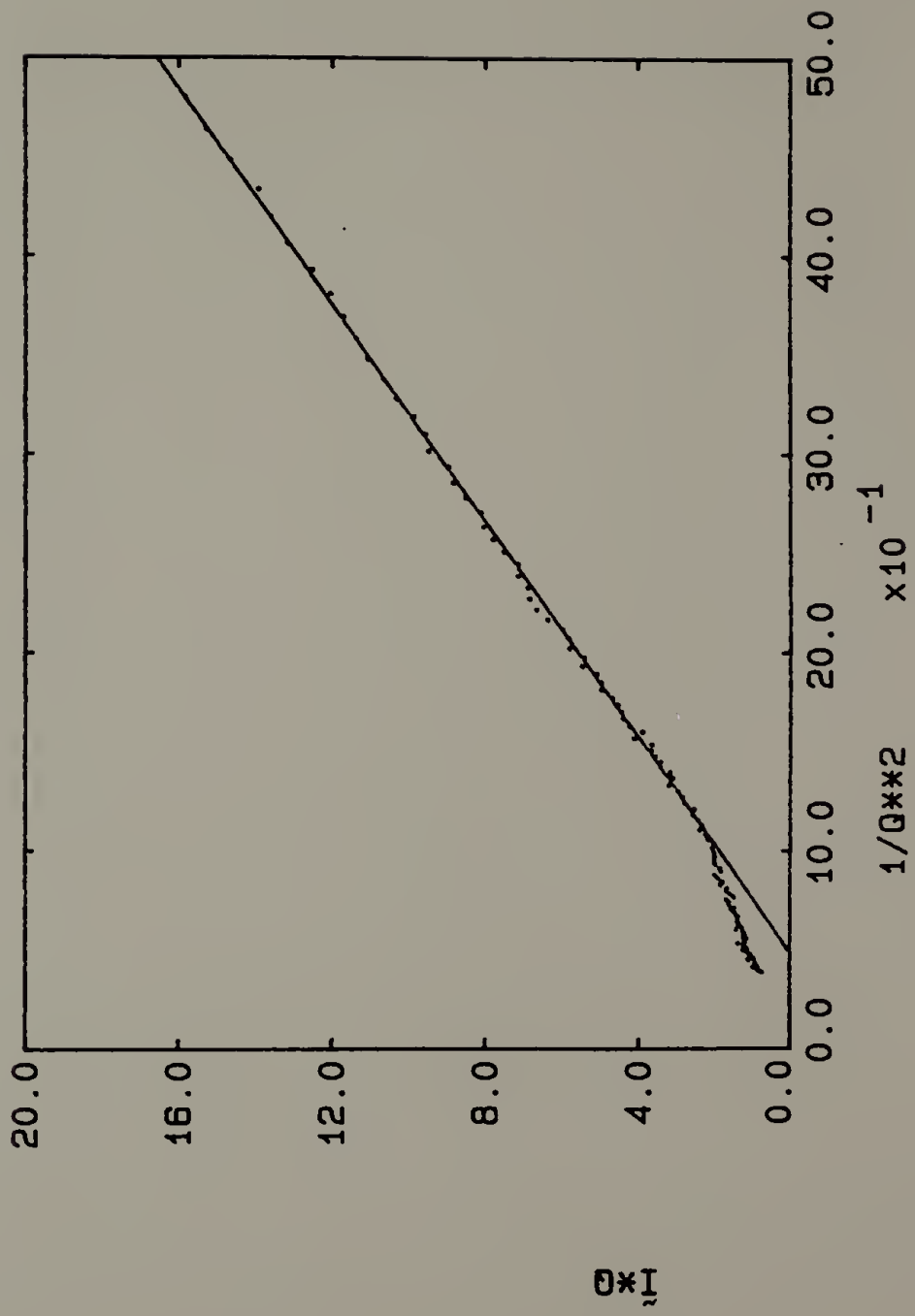Figure 35. Iq vs. q^{-2} SAXS intensities in the Porod region for 90 PVF$_2$/10 PMMA quenched blend.

Figure 36. Development of the equations and structure of the three-phase tiered model in real space.
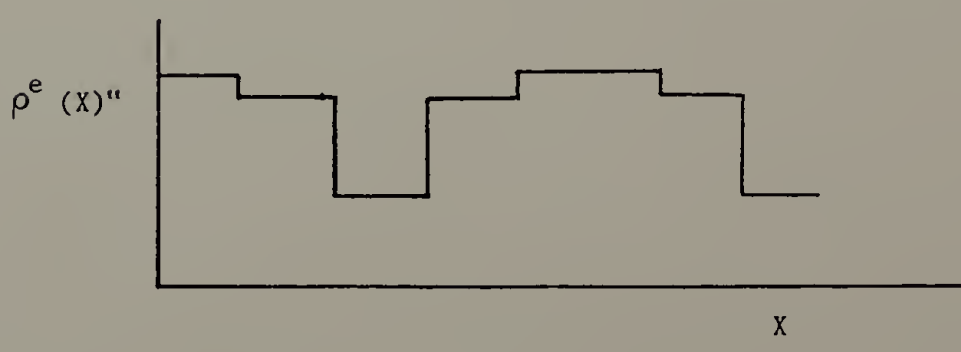
$$\rho^e(X) = \widehat{\rho_1(X)\ h(X)}$$
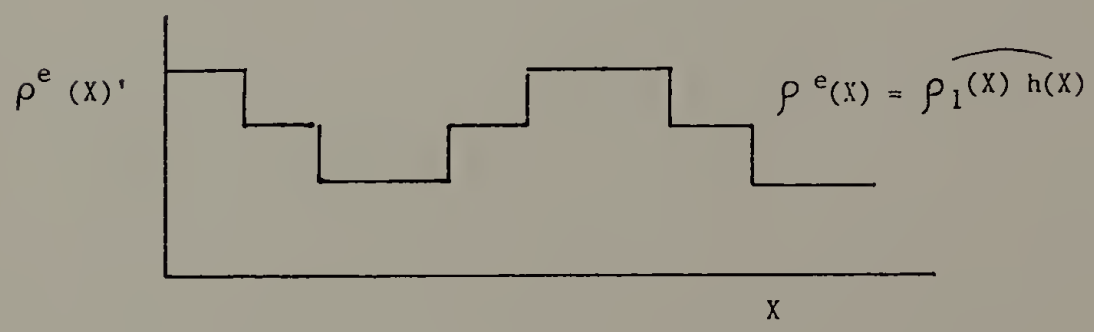
133

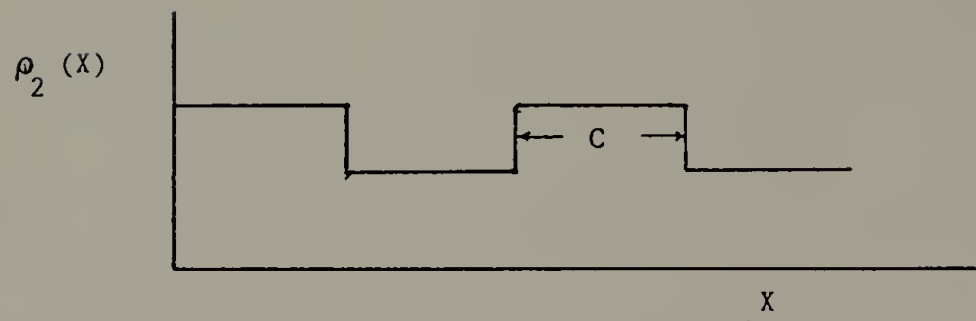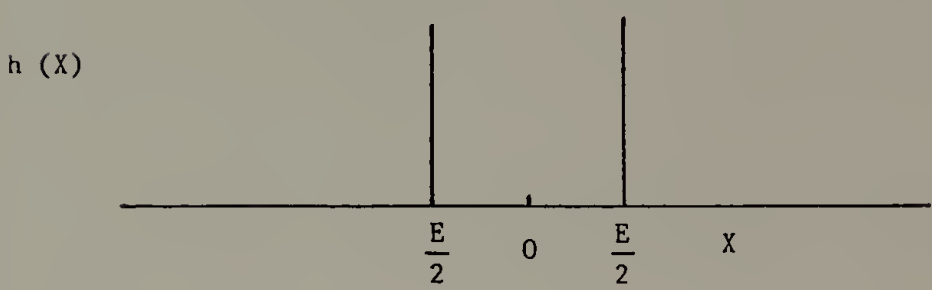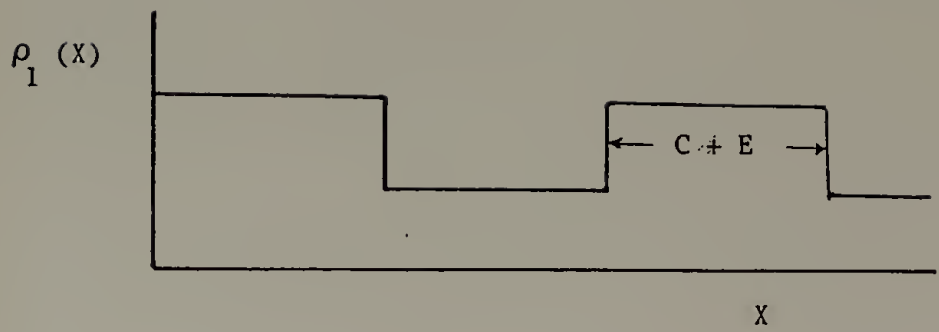Figure 37. Comparison of experimental and two calculated values for mean square electron density fluctuation (Morra's Analysis).
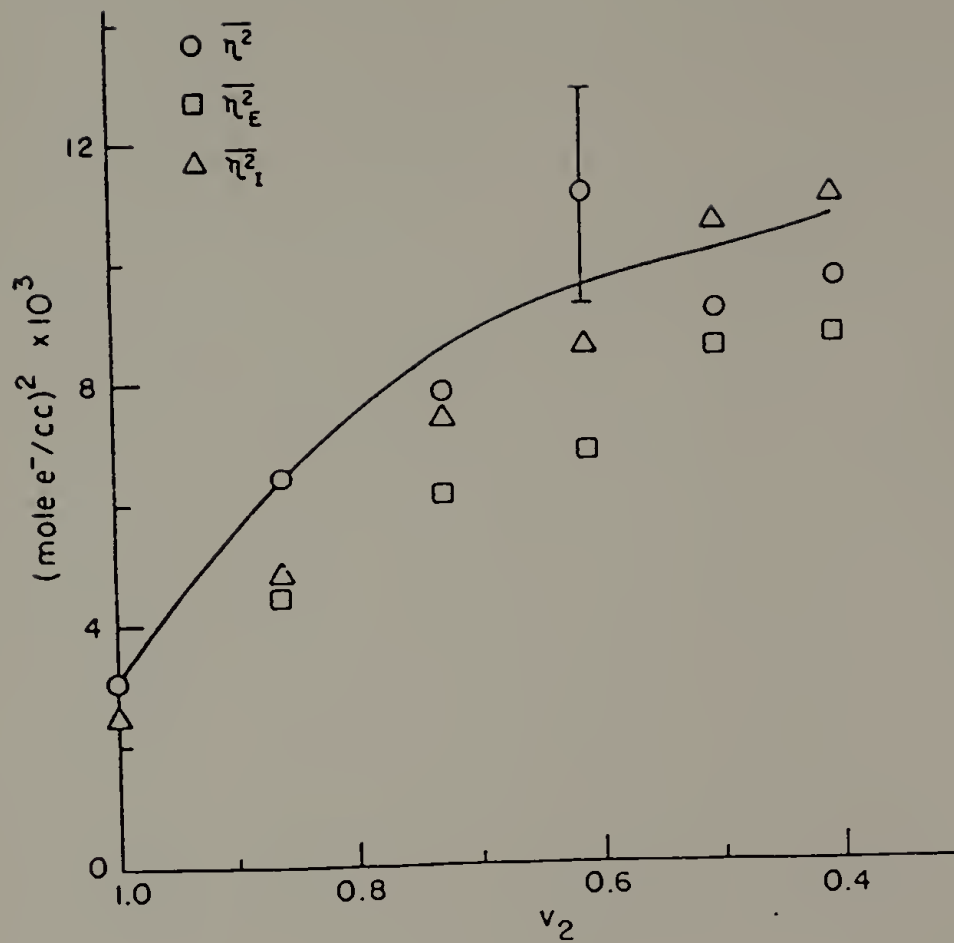
Figure 38. Electron density and correlation function representation for the ideal two-phase model compared with a real correlation function.
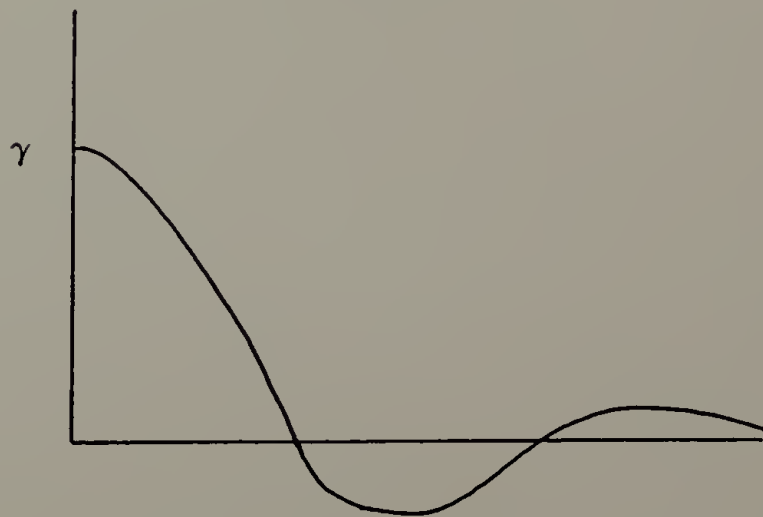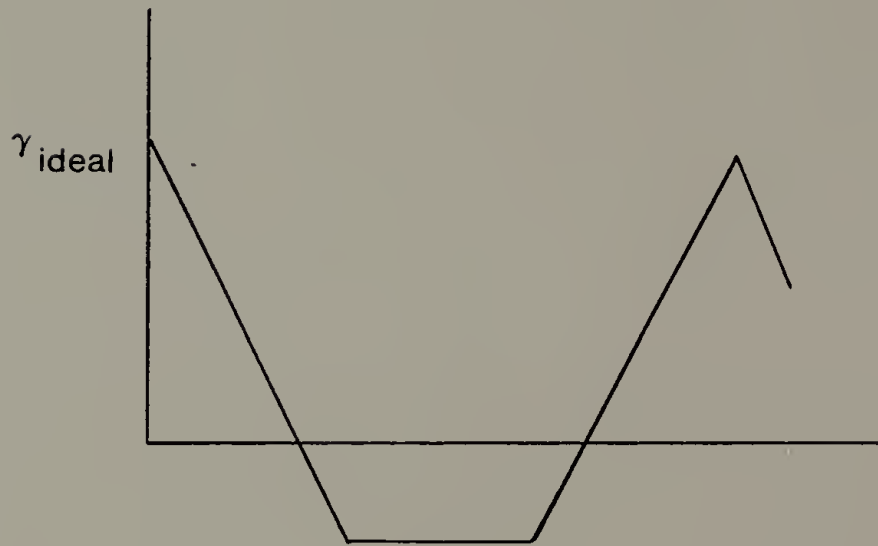
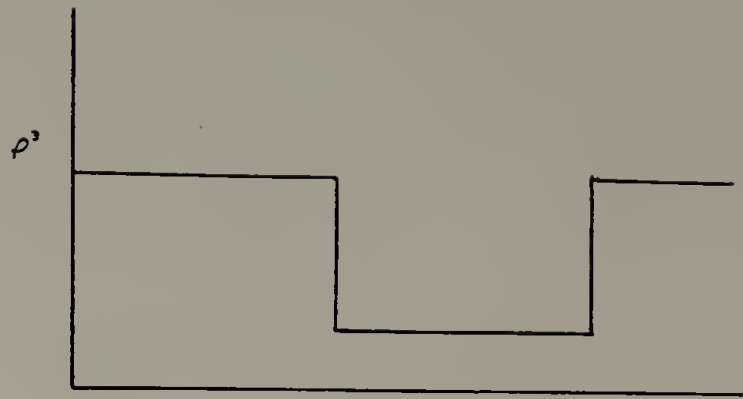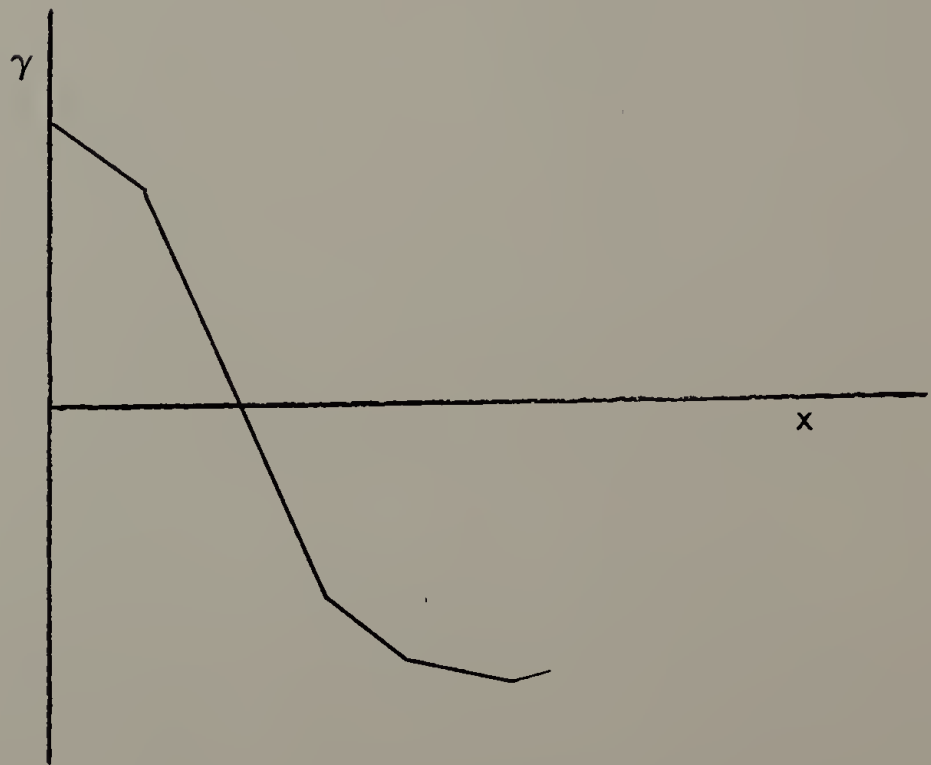Figure 39. Electron density profile and one-dimensional correlation function for the three-phase model.

IDEAL   THREE   PHASE   MODEL
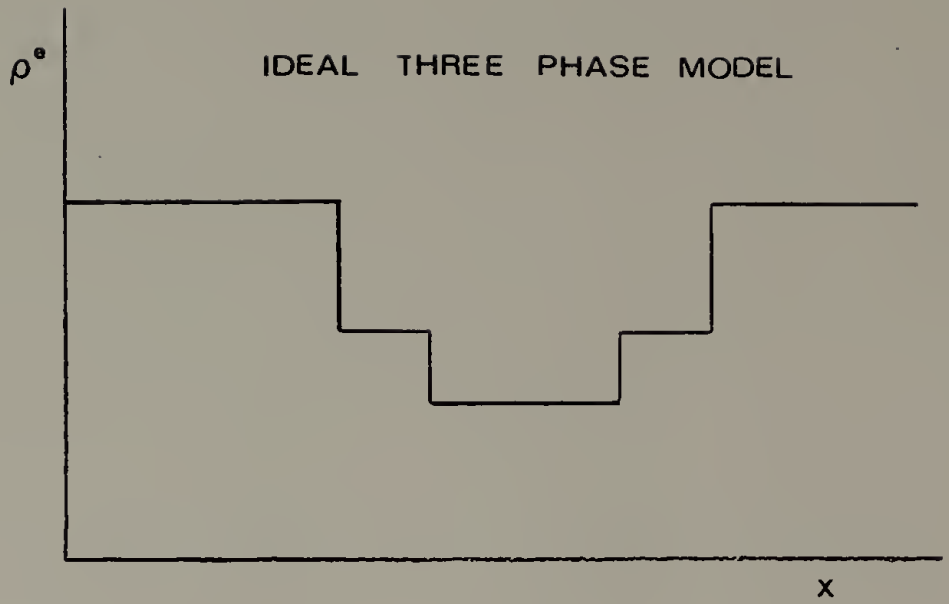
REFERENCES

1. Olabisi, O., Robeson, L.M., Shaw, M.T., <u>Polymer-Polymer Miscibility</u> Academic Press, 1979.

2. Paul, D.R., Newman, S., <u>Polymer Blends</u> Academic Press, 1978.

3. Hong, S.C., Shen, M., Russell, T. and Stein, R.S. in <u>Polymer Alloys</u> D. Klempner and K.C. Frisch, Eds., Plenum Press, N.Y. (1978).

4. Wunderlich, B. <u>Macromolecular Physics</u>, Volumes I, II, and III, Academic Press, N.Y. (1973).

5. Mansen, J.A. and Sperling, <u>Polymer Blends and Composites</u>, Plenum Press, N.Y. (1976).

6. Bommi, G., LeBlanc, Mod. Plast. Encycl. 53, 10A, 42 (1976).

7. Eickert, J.S., Mod. Plast. Encycl. 50, 10A, 56 (1973).

8. Emmett, R.A., Ind. Eng. Chem. 36, 730 (1944).

9. Reed, M.C., Mod. Plast. 27, 117 (1949).

10. Flory, P.J. J. Am. Chem. Soc. 87, 1833 (1965).

11. McMaster, L.P. Macromolecules 6, 760 (1973).

12. Patterson, D., Robard, A. Macromolecules 11, 690 (1978).

13. Murray, C.T., Gilmer, J.W., Stein, R.S. Macromolecules 18, 996 (1985).

14. Shibayama, M., Yang, H., Stein, R.S., Han, C.C. Macromolecules 18, 2179 (1985).

15. Cruz, C.A. Paul, D.R. and Barlow J.W. J. Appl. Polym. Sci. 23, 589 (1979).

16. Robeson, L.M. J. Appl. Polym. Sci. 17, 3607.

17. Berghmans, H. and Overbergh, N.J. Polym. Sci.-Polym. Phys. Ed. 15, 1757 (1977).

18. Martuscelli, E., Demma, G., Drioli, E., Nicolais, L., Spina, S., Hopfenberg, H.B. and Stannett, V.T. Polymer 20, 571 (1979).

19. Yeh, G.S.Y. and Lambert, S.L. J. Polym. Sci. Pt. A-2, 10 1183 (1972).

20. Calvert, P.D. and Ryan, T.G. Polymer 19, 611 (1978).

21. Warner, F.P. MacKnight, W.J. and Stein, R.S. J. Polym. Sci.-Polym. Phys. Ed., 15, 2113 (1977).

22. Wai, M.P., Ph.D. Thesis, University of Massachusetts, Amherst, MA (1982).

23. Carter, A.J., Davies, C.K.L., and Thomas, A.G., Joint Polish-Italian Symposium on Polymer Blends, Plenum Press, N.Y. (1981).

24. Wenig, W., Karasz, F.E. and MacKnight, W.J. J. Appl. Phys. 46, 4194 (1975).

25. Russell, T.P., Ph.D. Thesis, University of Massachusetts, Amherst, MA (1979).

26. Hermann, O., Master's Thesis, Deutsches Kuntstoff Institut, Darmstadt, FRG (1983).

27. Morra, B., Ph.D. Thesis, University of Massachusetts, Amherst, MA (1980).

28. Cross, W. Phil. Soc. Wash. 11, 411 (1981).

29. Bernauer, F. Gedrille Kristalle (1929).

30. Keith, H.D. and Padden, F.J., Jr. J. Appl. Phys. 34, 2409 (1963).

31. Chalmers, B.J. Principles of Solidification, Wiley, N.Y. (1964).

32. Delves, R.T. in Crystal Growth, Pergamon Press, Chapter 3 (1975).

33. Keith, H.D. and Padden, F.J., Jr. J. Appl. Phys. 35, 1270 (1964).

34. Keith, H.D. and Padden, F.J., Jr. J. Appl. Phys. 35, 1286 (1964).

35. Keith, H.D. J. Polym. Sci., Part A 2, 4339 (1964).

36. Keith, H.D. J. Appl. Phys. 35, 3115 (1964).

37. Beevers, R.B. and White, E.F.T. Trans. Farad. Soc. 56, 744 (1960).

38. deGennes, P.G. Scaling Concepts in Polymer Physics, Cornell Univ. Press, Ithaca, NY, page 239 (1979).

39. Nakagawa, K. and Ishida, Y.J. Polym. Sci., Polym. Phys. Ed. 11, 2153 (1973).

40. Osaki, S. and Ishida, Y.J. Polym. Sci., Polym. Phys. Ed. 13, 1071 (1975).

41. Lovinger, A.J. J. Polym. Sci., Polym. Phys. Ed. 18, 793 (1980).

42. Wahrmund, D.C., Bernstein, R.E., Barlow, J.W. and Paul, D.R. Polym. Eng. Sci. 18, 677 (1978).

43. Bernstein, R.E., Barlow, J.W. and Paul, D.R. Polym. Eng. Sci. 18, 683 (1978).

44. Bernstein, R.E., Wahrmund, D.C., Barlow, J.W. and Paul, D.R. Polym. Eng. Sci. 18, 1220 (1978).

45. Paul, D.R., Barlow, J.W., Bernstein, R.E. and Wahrmund, D.C. Polym. Eng. Sci. 18, 1225 (1978).

46. Roerdink, E. and Challa, G. Polymer 21, 509 (1980).

47. Leonard, C., Halary, J.L. and Monnerie, L. Polymer 26, 1507 (1985).

48. Saito, H., Fujita, Y. and Inoue, T. (submitted to Polymer Journal).

49. Flory, P.J. Principles of Polymer Chemistry Cornell Univ. Press, Ithaca, NY (1953).

50. Wendorff, J.H. J. Polym. Sci., Polym. Lett. Ed. 18, 445 (1980).

51. Hadziouanou, G. and Stein, R.S. Macromolecules 17, 567 (1984).

52. Nishi, T. and Wang, T.T. Macromolecules 8, 909 (1975).

53. Roerdink, E. and Challa, G. Polymer 19, 173 (1978).

54. Noland, J.S., Hsu, N.N., Saxon, R. and Schmitt, J.M. Adv. Chem. Ser. 99, 15 (1971).

55. Paul, D.R. and Altamirano, J.O. Polym. Preprints, Am. Chem. Soc. Div. Polym. Chem. 15, 409 (1974).

56. Hourston, D.J. and Challa, G. Polymer 18, 1175 (1977).

57. Paul, D.R. and Altamirano, J.O. Adv. Chem. Ser. 142, 371 (1975).

58. Hirata, Y. and Kotaka, T. Polymer J. 13, 273 (1981).

59. Sasabe, H., Saito, S., Asahina, M. and Kakutani, H. J. Polym. Sci., Part A-2 7, 1405 (1969).

60. Hahn, B., Wendorff, J. and Yoon, D.Y. Macromolecules 18, 718 (1985).

61. Hahn, B.R., Herrmann-Schonherr, O. and Wendorff, J.H. Polymer 28, 201 (1987).

62. Flory, P.J., Yoon, D.Y. and Dill, K.A. Macromolecules 17, 868 (1984).

63. Yoon, D.Y. and Flory, P.J. Macromolecules 17, 868 (1984).

64. Marqusee, J.A. and Dill, K.A. Macromolecules 19, 2420 (1986).

65. Vonk, C.G. J. Appl. Cryst. 6, 81 (1973).

66. Guinier, A. and Fournet, Small Angle Scattering of X-rays, Wiley, N.Y. (1955).

67. Hoseman, R. and Bagchi, S.N., Direct Analysis of Diffraction by Matter, Interscience Publishers, Inc., N.Y. (1962).

68. Alexander, L.E. X-ray Diffraction Methods in Polymer Science, Krieger Publishing Co., N.Y. (1979).

69. Glatter, O. and Kratky, O. Small Angle X-ray Scattering, Academic Press, N.Y. (1982).

70. Stein, R.S. and Higgins, J.S. J. Appl. Cryst. 11, 346 (1978).

71. Stein, R.S., Murray, C.T., Yang, H., Soni, V. and Lo, R. Physica 137B, 194 (1986).

72. Debye, P. and Bueche, A.M.J. Appl. Phys. 20, 518 (1949).

73. Debye, P., Anderson, H.R. and Brumberger, H. J. Appl. Phys. 28, 679 (1957).

74. Stein, R.S., Wilson, P.R. and Stidham, S.N. J. Appl. Phys. 34, 46 (1963).

75. Porod, G. Kolloid-Z. Z. Pol. 124, 83 (1951).

76. Porod, G. Small Angle X-ray Scattering (ed. by Brumberger) (1965).

77. Kratky, O. Pure and Appl. Chem. 12, 483 (1966).

78. Russell, T., Private communications.

79. Vonk, C.G. J. Appl. Cryst. 8, 340 (1975).

80. Ruland, W. J. Appl. Cryst. 4, 70 (1971).

81. Ruland, W. J. Appl. Cryst. 11, 535 (1978).

82. Ruland, W. Colloid Polym. Sci. 255, 417 (1977).

83. Rathje, J. and Ruland, W. Colloid Polym. Sci. 254, 358 (1976).

84. Todo, A., Hashimoto, T. and Kawai, H. Polym. Eng. Sci. 17, 587 (1977).

85. Vonk, C.G. and Pijpers, A.P. J. Polym. Sci. Polym. Phys. Ed. 23, 2517 (1985).

86. Vonk, C.G. J. Polym. Sci. Polym. Phys. Ed. 23, 2539 (1985).

87. Kinning, D.J., Ph.D. Thesis, University of Massachusetts, Amherst, MA (1986).

88. Koberstein, J.T. J. Polym. Sci., Polym. Phys. Ed. 20, 593 (1982).

89. Roe, R.J., Fishkis, M. and Chang, J.C. Macromolecules 14, 1091 (1981).

90. Shibayama, M. and Hashimoto, T. Macromolecules 19, 740 (1986).

91. Strobl, G.R. and Schneider, M. J. Polym. Sci. Polym. Phys. Ed. 18, 1343 (1980).

BIBLIOGRAPHY

- Alexander, L.E. <u>X-ray Diffraction Methods in Polymer Science</u>, Krieger Publishing Co., N.Y. (1979).

- Beevers, R.B. and White, E.F.T. Trans. Farad. Soc. 56, 744 (1960).

- Berghmans, H. and Overbergh, N.J. Polym. Sci.-Polym. Phys. Ed. 15, 1757 (1977).

- Bernauer, F. Gedrille Kristalle (1929).

- Bernstein, R.E., Barlow, J.W. and Paul, D.R. Polym. Eng. Sci. 18, 683 (1978).

- Bernstein, R.E., Wahrmund, D.C., Barlow, J.W. and Paul, D.R. Polym. Eng. Sci. 18, 1220 (1978).

- Bommi, G., LeBlanc, Mod. Plast. Encycl. 53, 10A, 42 (1976).

- Calvert, P.D. and Ryan, T.G. Polymer 19, 611 (1978).

- Carter, A.J., Davies, C.K.L., and Thomas, A.G., Joint Polish-Italian Symposium on Polymer Blends, Plenum Press, N.Y. (1981).

- Chalmers, B.J. <u>Principles of Solidification</u>, Wiley, N.Y. (1964).

- Cross, W. Phil. Soc. Wash. 11, 411 (1981).

- Cruz, C.A. Paul, D.R. and Barlow J.W. J. Appl. Polym. Sci. 23, 589 (1979).

- Debye, P. and Bueche, A.M.J. Appl. Phys. 20, 518 (1949).

- Debye, P., Anderson, H.R. and Brumberger, H. J. Appl. Phys. 28, 679 (1957).

- deGennes, P.G. <u>Scaling Concepts in Polymer Physics</u>, Cornell Univ. Press, Ithaca, NY, page 239 (1979).

- Delves, R.T. in <u>Crystal Growth</u>, Pergamon Press, Chapter 3 (1975).

- Eickert, J.S., Mod. Plast. Encycl. 50, 10A, 56 (1973).

- Emmett, R.A., Ind. Eng. Chem. 36, 730 (1944).

- Flory, P.J. J. Am. Chem. Soc. 87, 1833 (1965).

- Flory, P.J. Principles of Polymer Chemistry Cornell Univ. Press, Ithaca, NY (1953).

- Flory, P.J., Yoon, D.Y. and Dill, K.A. Macromolecules 17, 868 (1984).

- Glatter, O. and Kratky, O. <u>Small Angle X-ray Scattering</u>, Academic Press, N.Y. (1982).

- Guinier, A. and Fournet, <u>Small Angle Scattering of X-rays</u>, Wiley, N.Y. (1955).

- Hadziouanou, G. and Stein, R.S. Macromolecules 17, 567 (1984).

- Hahn, B., Wendorff, J. and Yoon, D.Y. Macromolecules 18, 718 (1985).

- Hahn, B.R., Herrmann-Schonherr, O. and Wendorff, J.H. Polymer 28, 201 (1987).

- Hermann, O., Master's Thesis, Deutsches Kuntstoff Institut, Darmstadt, FRG (1983).

- Hirata, Y. and Kotaka, T. Polymer J. 13, 273 (1981).

- Hong, S.C., Shen, M., Russell, T. and Stein, R.S. in <u>Polymer Alloys</u> D. Klempner and K.C. Frisch, Eds., Plenum Press, N.Y. (1978).

- Hoseman, R. and Bagchi, S.N., <u>Direct Analysis of Diffraction by Matter</u>, Interscience Publishers, Inc., N.Y. (1962).

- Hourston, D.J. and Challa, G. Polymer 18, 1175 (1977).

- Keith, H.D. and Padden, F.J., Jr. J. Appl. Phys. 34, 2409 (1963).

- Keith, H.D. and Padden, F.J., Jr. J. Appl. Phys. 35, 1270 (1964).

- Keith, H.D. and Padden, F.J., Jr. J. Appl. Phys. 35, 1286 (1964).

- Keith, H.D. J. Polym. Sci., Part A 2, 4339 (1964).

- Keith, H.D. J. Appl. Phys. 35, 3115 (1964).

- Kinning, D.J., Ph.D. Thesis, University of Massachusetts, Amherst, MA (1986).

- Koberstein, J.T. J. Polym. Sci., Polym. Phys. Ed. 20, 593 (1982).

- Kratky, O. Pure and Appl. Chem. 12, 483 (1966).

- Leonard, C., Halary, J.L. and Monnerie, L. Polymer 26, 1507 (1985).

- Lovinger, A.J. J. Polym. Sci., Polym. Phys. Ed. 18, 793 (1980).

- Mansen, J.A. and Sperling, <u>Polymer Blends and Composites</u>, Plenum Press, N.Y. (1976).

- McMaster, L.P. Macromolecules 6, 760 (1973).

- Marqusee, J.A. and Dill, K.A. Macromolecules 19, 2420 (1986).

- Martuscelli, E., Demma, G., Drioli, E., Nicolais, L., Spina, S., Hopfenberg, H.B. and Stannett, V.T. Polymer 20, 571 (1979).

- Morra, B., Ph.D. Thesis, University of Massachusetts, Amherst, MA (1980).

- Murray, C.T., Gilmer, J.W., Stein, R.S. Macromolecules 18, 996 (1985).

- Nakagawa, K. and Ishida, Y.J. Polym. Sci., Polym. Phys. Ed. 11, 2153 (1973).

- Nishi, T. and Wang, T.T. Macromolecules 8, 909 (1975).

- Noland, J.S., Hsu, N.N., Saxon, R. and Schmitt, J.M. Adv. Chem. Ser. 99, 15 (1971).

- Olabisi, O., Robeson, L.M., Shaw, M.T., Polymer-Polymer Miscibility Academic Press, 1979.

- Osaki, S. and Ishida, Y.J. Polym. Sci., Polym. Phys. Ed. 13, 1071 (1975).

- Patterson, D., Robard, A. Macromolecules 11, 690 (1978).

- Paul, D.R., Newman, S., Polymer Blends Academic Press, 1978.

- Paul, D.R., Barlow, J.W., Bernstein, R.E. and Wahrmund, D.C. Polym. Eng. Sci. 18, 1225 (1978).

- Paul, D.R. and Altamirano, J.O. Polym. Preprints, Am. Chem. Soc. Div. Polym. Chem. 15, 409 (1974).

- Paul, D.R. and Altamirano, J.O. Adv. Chem. Ser. 142, 371 (1975).

- Porod, G. Kolloid-Z. Z. Pol. 124, 83 (1951).

- Porod, G. Small Angle X-ray Scattering (ed. by Brumberger) (1965).

- Rathje, J. and Ruland, W. Colloid Polym. Sci. 254, 358 (1976).

- Reed, M.C., Mod. Plast. 27, 117 (1949).

- Robeson, L.M. J. Appl. Polym. Sci. 17, 3607.

- Roe, R.J., Fishkis, M. and Chang, J.C. Macromolecules 14, 1091 (1981).

- Roerdink, E. and Challa, G. Polymer 21, 509 (1980).

- Roerdink, E. and Challa, G. Polymer 19, 173 (1978).

- Ruland, W. J. Appl. Cryst. 4, 70 (1971).

- Ruland, W. J. Appl. Cryst. 11, 535 (1978).

- Ruland, W. Colloid Polym. Sci. 255, 417 (1977).

- Russell, T.P., Ph.D. Thesis, University of Massachusetts, Amherst, MA (1979).

- Russell, T., Private communications.

- Saito, H., Fujita, Y. and Inoue, T. (submitted to Polymer Journal).

- Sasabe, H., Saito, S., Asahina, M. and Kakutani, H. J. Polym. Sci., Part A-2 7, 1405 (1969).

- Shibayama, M., Yang, H., Stein, R.S., Han, C.C. Macromolecules 18, 2179 (1985).

- Shibayama, M. and Hashimoto, T. Macromolecules 19, 740 (1986).

- Stein, R.S. and Higgins, J.S. J. Appl. Cryst. 11,346 (1978).

- Stein, R.S., Murray, C.T., Yang, H., Soni, V. and Lo, R. Physica 137B, 194 (1986).

- Stein, R.S., Wilson, P.R. and Stidham, S.N. J. Appl. Phys. 34, 46 (1963).

- Strobl, G.R. and Schneider, M. J. Polym. Sci. Polym. Phys. Ed. 18, 1343 (1980).

- Todo, A., Hashimoto, T. and Kawai, H. Polym. Eng. Sci. 17, 587 (1977).

- Vonk, C.G. J. Appl. Cryst. 6, 81 (1973).

- Vonk, C.G. J. Appl. Cryst. 8, 340 (1975).

- Vonk, C.G. and Pijpers, A.P. J. Polym. Sci. Polym. Phys. Ed. 23, 2517 (1985).

- Vonk, C.G. J. Polym. Sci. Polym. Phys. Ed. 23, 2539 (1985).

- Wahrmund, D.C., Bernstein, R.E., Barlow, J.W. and Paul, D.R. Polym. Eng. Sci. 18, 677 (1978).

- Wai, M.P., Ph.D. Thesis, University of Massachusetts, Amherst, MA (1982).

- Warner, F.P. MacKnight, W.J. and Stein, R.S. J. Polym. Sci.-Polym. Phys. Ed., 15, 2113 (1977).

- Wendorff, J.H. J. Polym. Sci., Polym. Lett. Ed. 18, 445 (1980).

- Wenig, W., Karasz, F.E. and MacKnight, W.J. J. Appl. Phys. 46, 4194 (1975).

- Wunderlich, B. Macromolecular Physics, Volumes I, II, and III, Academic Press, N.Y. (1973).

- Yeh, G.S.Y. and Lambert, S.L. J. Polym. Sci. Pt. A-2, 10 1183 (1972).

- Yoon, D.Y. and Flory, P.J. Macromolecules 17, 868 (1984).